REPORT DOCUMENTATION PAGE

Form Approved
OMB No. 0704-0188

AFRL-SR-BL-TR-98-
0411

1. AGENCY USE ONLY (Leave Blank)	2. REPORT DATE	3. REPORT TYPE
	February 1993	Final

4. TITLE AND SUBTITLE
Molecular Beam Epitaxial Growth and Characterization of Mismatched InGaAs and InAlAs Layers on InP

5. FUNDING NUMBERS

6. AUTHORS
Brian R. Bennett

7. PERFORMING ORGANIZATION NAME(S) AND ADDRESS(ES)
Massachusetts Institute of Technology

8. PERFORMING ORGANIZATION REPORT NUMBER

9. SPONSORING/MONITORING AGENCY NAME(S) AND ADDRESS(ES)
AFOSR/NI
110 Duncan Avenue, Room B-115
Bolling Air Force Base, DC 20332-8080

10. SPONSORING/MONITORING AGENCY REPORT NUMBER

11. SUPPLEMENTARY NOTES

12a. DISTRIBUTION AVAILABILITY STATEMENT
Approved for Public Release

12b. DISTRIBUTION CODE

13. ABSTRACT *(Maximum 200 words)*
See attachment

14. SUBJECT TERMS	15. NUMBER OF PAGES
	16. PRICE CODE

17. SECURITY CLASSIFICATION OF REPORT	18. SECURITY CLASSIFICATION OF THIS PAGE	19. SECURITY CLASSIFICATION OF ABSTRACT	20. LIMITATION OF ABSTRACT
Unclassified	Unclassified	Unclassified	UL

Molecular Beam Epitaxial Growth and Characterization of Mismatched InGaAs and InAlAs Layers on InP

by

Brian R. Bennett

Submitted to the Department of Materials Science and Engineering
in partial fulfillment of the requirements for the degree of

Doctor of Philosophy in Electronic Materials

at the

MASSACHUSETTS INSTITUTE OF TECHNOLOGY

February 1993

Author .....Brian R. Bennett.....
Department of Materials Science and Engineering
October 16, 1992

Certified by .....Jesús A. del Alamo.....
Jesús A. del Alamo
Associate Professor of Electrical Engineering
Thesis Supervisor

Accepted by .....
Linn W. Hobbs
Professor of Materials Science
Chairman, Departmental Committee on Graduate Students

Molecular Beam Epitaxial Growth and Characterization of Mismatched InGaAs and InAlAs Layers on InP

by

Brian R. Bennett

Submitted to the Department of Materials Science and Engineering
on October 16, 1992, in partial fulfillment of the
requirements for the degree of
Doctor of Philosophy in Electronic Materials

Abstract

Mismatched epitaxial layers of $In_xGa_{1-x}As$ and $In_yAl_{1-y}As$ were grown on (001) InP by molecular beam epitaxy. The layers were characterized by a technique we developed known as variable azimuthal-angle ellipsometry. It reveals large optical anisotropy for many strained layers. We attribute the anisotropy to strain-induced surface roughening during growth. Samples were also characterized by high-resolution x-ray diffraction (HRXRD) to assess layer quality as well as composition and strain. HRXRD measurements reveal orthorhombic distortion of partially relaxed layers of InGaAs and InAlAs in tension or compression, with preferential strain relief in the [110] direction. We show that HRXRD epilayer peak width and interference fringes are sensitive, non-destructive criteria to judge the structural quality of strained heterostructures. For layers ranging from 300 to 10,000 Å, with lattice mismatch of $\pm$ 1% or less, the crystalline quality consistently remains high to thicknesses up to 3-9 times the Matthews-Blakeslee critical layer thickness. We investigated the thermal stability of these layers, using HRXRD to measure structural changes caused by high-temperature anneals. We also compared the electron mobility of modulation-doped heterostructures before and after annealing. Both techniques demonstrate that our high-quality strained layers are stable to temperatures of at least 800-850°C. We explain this result by the limited sources available for the nucleation of misfit dislocations. The findings are applied to the design and growth of high-performance pseudomorphic InAlAs/InGaAs/InP heterostructure field-effect transistors with layers exceeding the Matthews-Blakeslee limit.

Thesis Supervisor: Jesús A. del Alamo
Title: Associate Professor of Electrical Engineering

Acknowledgements

My graduate studies at MIT were supported by a fellowship from the Air Force Office of Scientific Research, a research grant from Nippon Telegraph and Telephone Corporation, NSF-PYI #9157305-ECS and AASERT #DAAL03-92-G-0046. I gratefully acknowledge this support.

The work described here would not have been possible without the use of an MBE. I thank Prof. Clif Fonstad for allowing me to be a grower on his system. I also thank Sandeep Bahl for teaching me to use the MBE and performing the HFET processing and testing, among many other things. Maintaining an MBE system is a group effort; it was fortunate that the mechanical abilities of other group members were greater than mine. I thank all my fellow growers, past and present: Elias Towe, Jim Vlcek, Geoff Burns, Tom Broekaert, Richard Singer, Woo-Young Choi, Paul Martin, Jurgen Smet, Krishna Shenoy, and Raj Aggarwal.

My HRXRD measurements were performed in the X-Ray Diffraction Central Facilities at MIT. I thank Joe Adario and Peter Kloumann for helping me keep the system working. I thank David Greenberg, Chock Gan, and Lung-Han Peng for assistance on topics ranging from calculating Fermi levels to including postscript figures in LaTeX. I also appreciate the help of Angela Odoardi and Kelley Donovan.

This work benefited greatly from collaborations with groups outside of MIT. Francisca Peiro and Prof. Albert Cornet of the University of Barcelona performed the TEM measurements. I thank them for the excellent and timely results. The RDS measurements were performed at Bellcore, in collaboration with David Aspnes and Kurt Hingerl. I am grateful for their help. I also thank Noren Pan of Raytheon for supplying MOCVD-grown layers of InAlAs (and many good tennis matches over the last year).

My former employers, Rome Laboratory at Hanscom Air Force Base, allowed me access to their facilities during my time at MIT. I thank Joe Lorenzo for making this possible. I also appreciate Richard Soref's time and encouragement while serving as my mentor in the AFOSR fellowship program. Finally, thanks to Ken Vaccaro for a great deal of help over the past several years.

I carried out this work as a materials science student working in an electrical engineering group. In this situation, my thesis committee became much more than a formality. My committee members, Profs. Carl Thompson and Kim Kimerling, made important contributions to this work. I thank them for their time and interest.

For the past four years, I have had the pleasure of working with Prof. Jesús del Alamo. He gave me the independence to pursue topics of interest to me. At the same time, he was an enthusiastic partner in my research. One could not ask for more from an advisor.

Contents

1 Introduction **13**

1.1 Why $In_xGa_{1-x}As/InP$ and $In_yAl_{1-y}As/InP$? 13

1.2 Critical Layer Thickness: Theory 15

1.3 Critical Layer Thickness: Experiments 18

1.4 Metastability 20

1.5 Growth Modes 21

1.6 Summary 24

1.7 Outline of Thesis 25

2 Characterization by High-Resolution X-Ray Diffraction **27**

2.1 Background 28

2.2 Crystalline Quality 34

2.3 Lattice Relaxation and Orthorhombic Distortion 48

2.4 Optimal Thickness for Composition Measurements 59

2.5 Summary 66

3 Optical Anisotropy **67**

3.1 Background 68

3.2 Variable Azimuthal-Angle Ellipsometry 69

3.3 Reflectance Difference Spectroscopy 76

3.4 Physical Origin of Optical Anisotropy 79

3.5 Summary 87

4 Relaxation Kinetics and Thermal Stability **88**

4.1 Annealing: Structural Stability 89

4.2 Annealing: Electronic Stability 92

4.3 Relaxation Kinetics 100

4.4 Summary 107

5 Device Application: Heterostructure Field-Effect Transistors **111**

5.1 HFET Characterization by HRXRD 112

5.2 Device Characteristics 114

5.3 Heterostructure Evaluation 115

5.4 Survey of Pseudomorphic $In_xGa_{1-x}As/In_yAl_{1-y}As/InP$ HFETs 118

5.5 Summary 120

6 Discussion **121**

6.1 Composition Modulation 121

6.2 Heterogeneous Nucleation of Dislocations 123

6.3 Asymmetries in Misfit Dislocation Density 125

6.4 Surface Roughness and Relaxation 127

6.5 Summary 132

7 Summary **133**

7.1 Conclusions 133

7.2 Suggestions for Future Work 136

A Molecular Beam Epitaxy of InGaAs and InAlAs **138**

B Material Parameters of InP, GaAs, InAs, and AlAs **143**

C Matthews-Blakeslee Critical Layer Thickness **144**

Bibliography **147**

List of Figures

1-1 Energy gap versus lattice constant at 300K for selected III-V compound semiconductors. 14

1-2 Proposed growth modes for stained epitaxial layers. 16

1-3 Critical layer thickness, as determined by Hall mobility, versus InAs mole-fraction in $In_{0.52}Al_{0.48}As/In_xGa_{1-x}As/InP$ modulation-doped structures. 19

1-4 Strained-layer thickness versus InAs mole fraction for $In_xGa_{1-x}As/InP$ p-i-n photodiodes. 20

2-1 Schematic of double-crystal x-ray diffraction system. 29

2-2 HRXRD (004) rocking curve for sample 1683, 1760 Å of $In_{0.530}Al_{0.470}As$ on InP. 32

2-3 HRXRD (004) experimental and simulated rocking curves for sample 1876; heterostructure cross-section is shown. 34

2-4 HRXRD (004) rocking curves for four $In_{0.42}Al_{0.58}As$ heterostructures with varying epilayer thickness. 36

2-5 HRXRD (004) rocking curves for five heterostructures shown in inset. 38

2-6 HRXRD (004) rocking curves for four 1000 Å layers of $In_xGa_{1-x}As$ in compression. 38

2-7 HRXRD (004) rocking curves for five 1000 $\AA$ layers of $In_yAl_{1-y}As$ in tension. 39

2-8 HRXRD (004) rocking curves for five 1000 $\AA$ layers of $In_yAl_{1-y}As$ in compression. 40

2-9 HRXRD (004) rocking curves for samples 2006 and 2010. 41
2-10 HRXRD (004) rocking curves for two MODFETs with nominally identical structures, including 500 Å channels of $In_{0.68}Ga_{0.32}As$. 42
2-11 HRXRD (004) peak width versus InGaAs or InAlAs thickness for layers in compression and tension. 43
2-12 Ratio of experimental to theoretical HRXRD (004) peak width versus ratio of thickness to anisotropic Matthews-Blakeslee critical thickness for (a) InGaAs and (b) InAlAs layers. 45
2-13 Thickness versus relaxed lattice mismatch for a) InGaAs and b) InAlAs in both compression and tension on InP. 46
2-14 Geometry of x-ray measurements. 49
2-15 HRXRD (004) rocking curves for sample 1503, showing different epilayer peak widths at $\alpha = 0$ and 90^o. 50
2-16 HRXRD (004) epilayer peak width as a function of azimuthal angle for sample 1503. Solid line is a least-squares fit to a cosine function. . . . 50
2-17 Geometry of glancing-exit and glancing-incidence asymmetric HRXRD measurements. 51
2-18 HRXRD rocking curves for (224) glancing-exit reflections of sample 1245 at azimuthal angles of 0^o and 90^o. The difference in peak separation for the two curves indicates asymmetric strain in the epilayer. . . 54
2-19 Thickness versus lattice mismatch for a) InGaAs and b) InAlAs. . . . 56
2-20 Difference in relaxation in the [110] and $[1\bar{1}0]$ directions as a function of the ratio of thickness to Matthews-Blakeslee critical layer thickness. Most of the samples exhibit substantial orthorhombic distortion. . . . 58
2-21 Schematic view of lattice distortion as a function of degree of relaxation for an epilayer with a larger lattice constant than the substrate: a) t $< t_c$, b) and c) t $> t_c$, d) t $>> t_c$. 59
2-22 Thickness versus lattice mismatch for 150 samples of InGaAs and InAlAs on InP. 60

2-23 Simulated HRXRD rocking curves for $In_{0.60}Ga_{0.40}As$/InP heterostructures with different epilayer thicknesses.[63] 61
2-24 Epilayer thickness versus mismatch showing the minimum resolvable peak (MRP) criteria, the thickness at which the error in composition due to layer peak shift is 0.005, and the 10% relaxation threshold of $5t_{c,MB}$. 62

3-1 Geometry of ellipsometry measurements. 70
3-2 Ellipsometric parameter Δ as a function of azimuthal angle for sample 1530, mismatched InGaAs in tension. 71
3-3 Ellipsometric parameter Δ as a function of azimuthal angle for sample 1877, nearly lattice-matched InGaAs. 71
3-4 Amplitude of the cosine function fits for the ellipsometric parameter Δ as a function of lattice mismatch for a set of InGaAs layers in tension. 72
3-5 Amplitude of the cosine function fits for the ellipsometric parameter Δ as a function of lattice mismatch for a set of InGaAs layers in compression. 73
3-6 Ellipsometric parameter Δ as a function of azimuthal angle for sample 1843, InAlAs in compression. Solid line is a least-squares fit to eq. (3.5). 74
3-7 Amplitude of the cosine function fit for the ellipsometric parameter Δ as a function of lattice mismatch for a set of InAlAs layers in compression. 74
3-8 Amplitude of the cosine function fit for the ellipsometric parameter Δ as a function of thickness for a set of InAlAs layers in compression. . 75
3-9 Amplitude of the cosine function fit for the ellipsometric parameter Δ as a function of the ratio of the HRXRD experimental and theoretical (004) peak widths for (a) InGaAs and (b) InAlAs layers. 77
3-10 Polarization of incident light with respect to the crystallographic directions of the sample for reflectance difference spectroscopy on an (001) substrate. 78
3-11 Magnitude and phase of RDS signal as a function of photon energy for 1879, a sample with good crystalline quality. 79

3-12 Magnitude and phase of RDS signal as a function of photon energy for 1880, a sample with degraded crystalline quality. 80
3-13 Comparison of a) magnitude, and b) phase, from reflectance difference spectroscopy with anisotropy parameter from variable azimuthal angle ellipsometry. The photon energy is 1.96 eV for both techniques. . . . 81
3-14 Optical anisotropy as a function of the difference in strain in the [110] and [1$\bar{1}$0] directions for partially relaxed InGaAs layers. 82
3-15 Plan-view transmission electron micrograph for sample 3099, 1000 Å of $In_{0.579}Al_{0.421}As$. 83
3-16 Plan-view transmission electron micrograph for sample 1530. 84
3-17 Cross-section transmission electron micrograph for sample 1530. . . . 85
3-18 Plan-view transmission electron micrograph for sample 1879 with g = [220]. 86
3-19 Plan-view transmission electron micrograph for sample 1880 with g = [220]. 86

4-1 HRXRD scans of sample 1441, a partially relaxed layer of InGaAs with $t/t_{c,MB} = 33$, before and after annealing. The shift in the layer peak indicates lattice relaxation during the anneal. 90
4-2 HRXRD scans of sample 1331, a coherent layer of InGaAs with $t/t_{c,MB} =$ 0.5, before and after annealing. 91
4-3 HRXRD scans of a 1700 Å layer of $Si_{0.82}Ge_{0.18}$ on Si with $t/t_{c,MB} = 8$. The layer was grown at 500°C and annealed for 60 seconds at 550-850°C. 92
4-4 HRXRD scans of sample 1879 before and after annealing. The sample includes an InGaAs layer with $t/t_{c,MB} = 7.3$. 93
4-5 HRXRD scans of sample 1682, a single layer of InAlAs with $t/t_{c,MB} =$ 8.6, before and after annealing. 93
4-6 Cross-section of modulation-doped structures used in this study. . . . 94
4-7 HRXRD scans of sample 4089, a MODFET heterostructure, before and after annealing. The InGaAs channel is a factor of 2.6 thicker than $t_{c,MB}$. 95

4-8 Electron mobility (a) and sheet carrier concentration (b) at 300 K as a function of annealing for MODFET heterostructures. 97
4-9 Electron mobility (a) and sheet carrier concentration (b) at 77 K as a function of annealing for MODFET heterostructures. 98
4-10 Parallel lattice mismatch as a function of layer thickness for two sets of InGaAs layers in compression. 102
4-11 Parallel lattice mismatch as a function of layer thickness for InGaAs layers in tension. 103
4-12 Parallel lattice mismatch as a function of layer thickness for InAlAs layers in compression. 103
4-13 Parallel lattice mismatch as a function of layer thickness for InAlAs layers in tension. 104
4-14 Behavior of substrate threading dislocations in strained-layer epitaxy. 105
4-15 Formation of a misfit dislocation from a dislocation half-loop. The critical radius of the half-loop is r^*. 106
4-16 Critical radius (a) and energy (b) for homogeneous nucleation of dislocation half-loops in InGaAs. 108
4-17 Critical radius (a) and energy (b) for homogeneous nucleation of dislocation half-loops in InAlAs. 109

5-1 Cross-section of doped-channel InAlAs/InGaAs heterostructure field-effect transistor. 112
5-2 Experimental and simulated HRXRD rocking curves for HFET 1870. 114
5-3 Output I-V characteristics for HFET 1870. The gate length was 1.9 μm and the gate width was 200 μm. 115
5-4 Unity current and power gain cut-off frequencies for HFET 1870. The drain-source voltage is fixed at 4.5 V. 116
5-5 HRXRD rocking curves for HFETs with structures similar to fig. 5.1. 117
5-6 Layer thickness versus mismatch for InGaAs (a) and InAlAs (b) including device results. 119

6-1 Atom positions in the zinc-blende structure. 126
6-2 Proposed regions based upon material quality and thermal stability of our InGaAs layers on InP. 129

A-1 Schematic of Riber 2300 Molecular Beam Epitaxy system used in this study. 139
A-2 Calibration of the composition of $In_xGa_{1-x}As$. 141

C-1 Matthews-Blakeslee critical layer thickness for InGaAs layers on InP. 146
C-2 Matthews-Blakeslee critical layer thickness for InAlAs layers on InP. . 146

List of Tables

1.1 Lattice mismatch, energy gap, and anisotropic Matthews-Blakelsee critical layer thickness for $In_xGa_{1-x}As/InP$ at 300K. 18

B Material Parameters of InP, GaAs, InAs, and AlAs. 143

Chapter 1

Introduction

1.1 Why $In_xGa_{1-x}As/InP$ and $In_yAl_{1-y}As/InP$?

Compound semiconductors are of interest for both optical and electronic devices. Solid-state lasers can be fabricated from III-V semiconductors such as gallium arsenide (GaAs) and indium phosphide (InP) because these materials, unlike silicon, have fundamental energy gaps which are direct. These materials also offer the possibility of very high-speed electronic devices. If only binary semiconductors are considered, however, the device possibilities are somewhat limited. The use of ternary alloys such as $Al_xGa_{1-x}As$ and $In_xGa_{1-x}As$ allows much greater freedom to choose materials with the desired characteristics such as energy gap and electron mobility.

In fig. 1.1, we plot the energy gap as a function of lattice constant for selected III-V compound semiconductors. GaAs and AlAs have almost identical lattice constants. Hence, any composition of $Al_xGa_{1-x}As$ will be nearly lattice matched to GaAs. For this reason, much research has focussed on the $Al_xGa_{1-x}As/GaAs$ materials system.

In contrast to GaAs, nature does not provide a ternary alloy system which is always lattice matched to InP. As shown in fig. 1.1, $In_yAl_{1-y}As$ is only lattice matched to InP when y=0.52. Similarly, $In_xGa_{1-x}As$ is lattice matched if and only if x=0.53. If the quaternary $In_{1-x-y}Ga_xAl_yAs$ (with $x + y \approx 0.47$) is used, alloys with energy gaps covering the range of 0.74 to 1.44 eV can be lattice matched to InP. This range includes both the minimum dispersion wavelength (1.3 μm) and the minimum at-

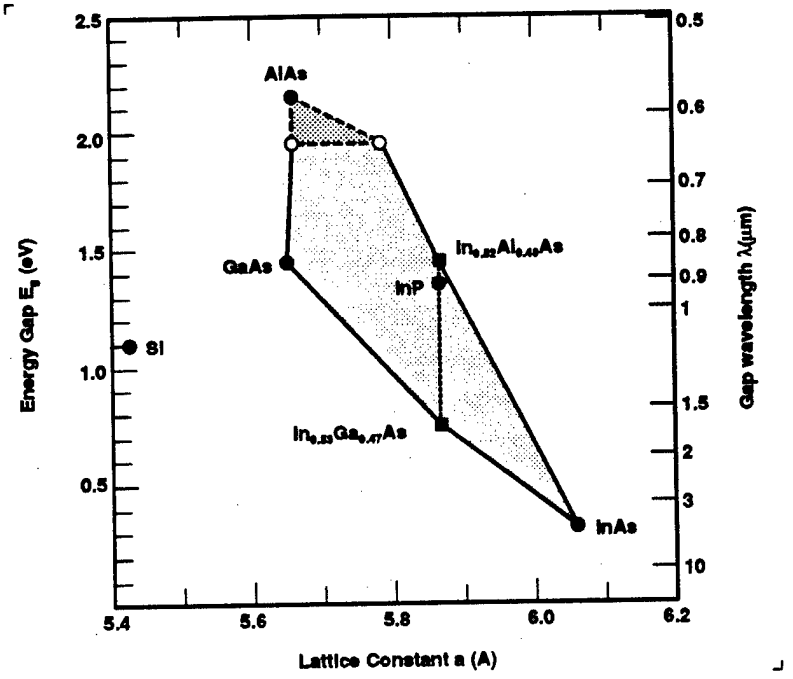

Figure 1-1: Energy gap versus lattice constant at 300K for selected III-V compound semiconductors (courtesy of J.C. Vlcek).

tenuation wavelength (1.55 μm) of silica optical fibers. Primarily for this reason, InP-based compounds are the materials of choice for lasers and detectors in optical telecommunications.

Electronic devices based upon InP are also of interest because of the potential for integration with optical components to build optoelectronic integrated circuits. In addition, the InP materials system has several intrinsic advantages for electronic devices. For example, $In_{0.53}Ga_{0.47}As$ has a room-temperature mobility of 11,000 cm^2/V-sec and a peak electron velocity of 3.0×10^7 cm/sec.[1] These values are considerably higher than those for GaAs or Si, and make $In_{0.53}Ga_{0.47}As$ a promising material for high-frequency microwave transistors and high-speed digital circuits. The conduction band offset between $In_{0.52}Al_{0.48}As$ and $In_{0.53}Ga_{0.47}As$ is 0.5 eV, compared to about 0.3 eV for the AlGaAs/GaAs system.[1] Hence, $In_{0.52}Al_{0.48}As$ can be used as a pseudo-insulator to confine electrons in the $In_{0.53}Ga_{0.47}As$ channel of heterostructure field-effect transistors (HFETs) lattice-matched to InP.

If we eliminate the requirement of lattice matching, the range of available material

properties is expanded. For example, $In_xGa_{1-x}As$ with $x > 0.53$ has an even higher mobility and peak velocity than $In_{0.53}Ga_{0.47}As$, and can be used as the channel in HFETs. The lattice mismatch will result in strained epitaxial layers. In the case of certain optical devices, the strain itself is beneficial. Strain splits the light- and heavy-hole valence band degeneracy, resulting in lower threshold current for solid-state lasers. Clearly, the use of mismatched layers in the InGaAs/InAlAs/InP materials system is desirable for many device applications.

1.2 Critical Layer Thickness: Theory

There is a limit to the amount of strain which can be accomodated by epitaxial layers. If a layer is sufficiently thick and mismatched, the formation of misfit dislocations at the substrate/epilayer interface becomes energetically favorable. These dislocations relieve strain, but also degrade the structural, electrical, and optical quality of epitaxial layers, often making them unsuitable for device applications.

In fig. 1.2, we show schematics of epitaxial growth of strained layers. We assume the epitaxial layer has a larger lattice constant than the substrate. If the lattice mismatch between the epilayer and substrate is small and the layer is thin, the mismatch will be accomodated entirely by strain in the layer and atomic bonds will be continuous across the interface (A). In this case, the symmetry of the epilayer lattice distorts from cubic to tetragonal, and the layer is said to be coherent or pseudomorphic. As the layer thickness is increased, misfit dislocations will form, relieving a portion of the strain and resulting in a partially-relaxed layer (B). Lattice constants perpendicular to the plane of growth, $a_\perp$, and parallel to the plane of growth, $a_{||}$, are shown. In case A, $a_{||}$ is equal in the substrate and epilayer; in case B, the values are different. In both A and B, $a_\perp$ is not equal in the substrate and epilayer. Growth modes C and D will be discussed later in this chapter.

For a fixed lattice mismatch, the thickness at which misfit dislocations begin to form is known as the *critical layer thickness.* Several theories have been proposed to predict the critical layer thickness. The most widely accepted theory was published

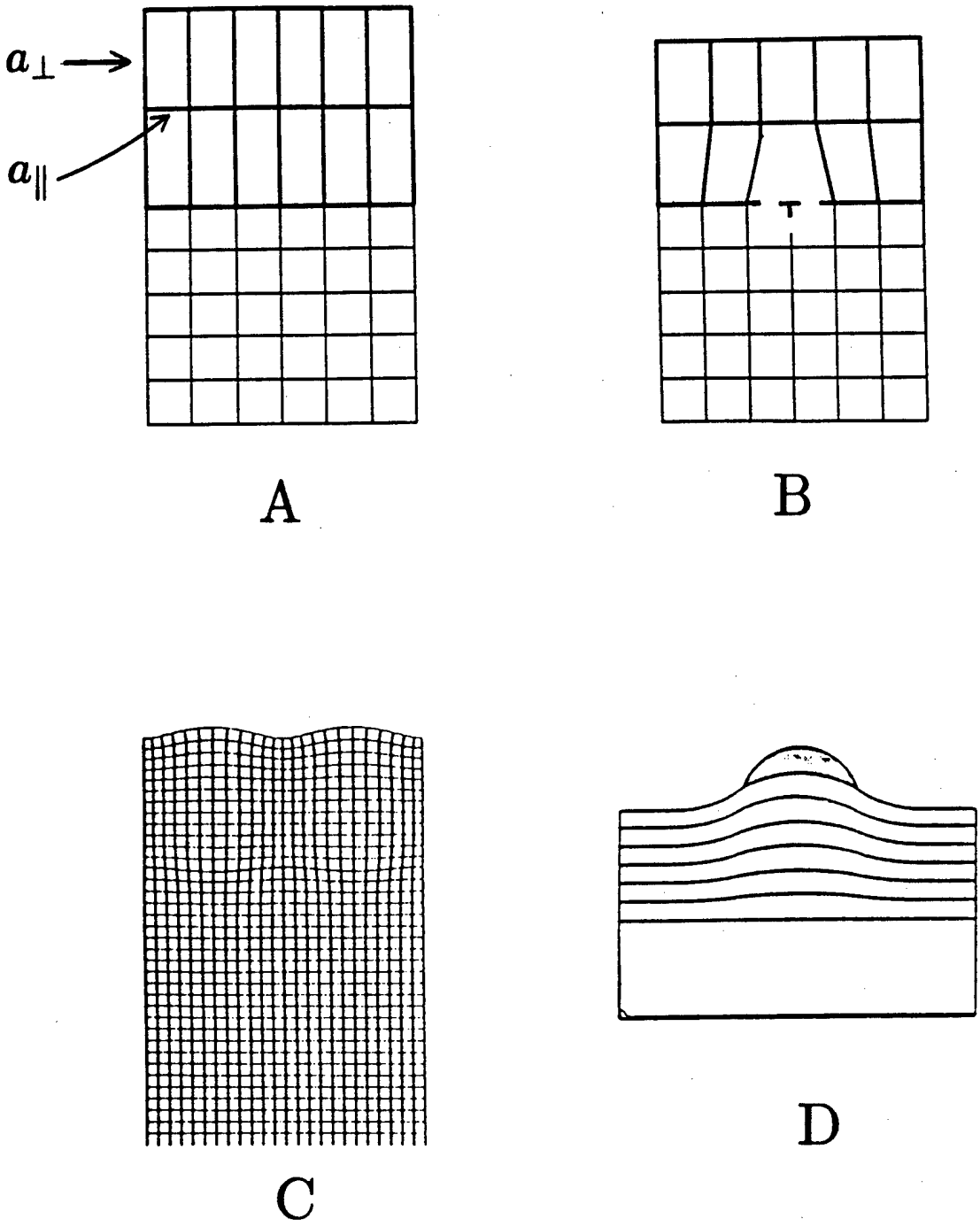

Figure 1-2: Proposed growth modes for stained epitaxial layers. A) 2-D growth of a coherent (dislocation-free), tetragonally distorted layer. B) 2-D growth of a partially relaxed layer in which misfit dislocations at the layer/substrate interface have relieved strain. C) 2-D growth with composition modulation.[48] D) 3-D growth of a coherent island; strain is relieved by the deformation of the substrate.[33]

by Matthews and Blakeslee (M-B) in 1974.[2] M-B considered the formation of misfit dislocations at the layer/substrate interface by the elongation of threading dislocations from the substrate. They equated the force exerted on the dislocation line by misfit stress with the tension in the dislocation line. The result was a transcendental equation relating the critical layer thickness to the mismatch and elastic constants. In appendix C, we give the equation and an extension of the theory to account for anisotropic elastic properties. To first order, $t_{c,MB}$, the M-B critical layer thickness, is inversely proportional to the lattice mismatch, f, which is given by:

$$f = \frac{a_e - a_S}{a_S} \tag{1.1}$$

where a_S and a_e are the lattice constants of the substrate and epilayer, respectively.

To get some idea of the limitations that the M-B theory imposes on strained-layer design and band-gap engineering, we give the values of both the energy gap[3] and $t_{c,MB}$ for InAs-rich $In_xGa_{1-x}As$ on InP in table 1.1. Complete plots of $t_{c,MB}$ for both $In_xGa_{1-x}As$ and $In_yAl_{1-y}As$ are given in appendix C. From the table, we see that if a band-gap of 0.07 eV less than the lattice matched value is required, the layer thickness is limited to 300 Å. For a lattice mismatch of 1%, the critical thickness is only about 130 Å. We also consider a layer of $In_{0.540}Ga_{0.460}As$ which is about as close to lattice matching as can be routinely achieved in epitaxial growth. For this layer, $t_{c,MB}$ is only 4400 Å; thicker layers are often required in optical devices. It is clear that the M-B limit places severe constraints on the design of strained-layer and even nominally lattice-matched heterostructures.

An epilayer with a small number of misfit dislocations may still be suitable for certain device applications. In fact, InP substrates always contain threading dislocations so a truly defect-free heterostructure is not possible. Elman suggested a more practical approach, proposing an "effective critical layer thickness, defined as the thickest layer still useful for high quality optical devices."[4] This effective thickness will depend upon the specific optical (or electronic) device in question.

Table 1.1: Lattice mismatch, energy gap, and anisotropic Matthews-Blakelsee critical layer thickness for $In_xGa_{1-x}As/InP$ at 300K.

x	f	E_g (eV)	$t_{c,MB}$ (Å)
0.532	0.00000	0.736	∞
0.54	0.00054	0.728	4400
0.56	0.00192	0.707	960
0.60	0.00469	0.668	300
0.65	0.00814	0.620	170
0.70	0.0116	0.574	110
0.80	0.0185	0.490	60
1.00	0.0323	0.350	30

1.3 Critical Layer Thickness: Experiments

Over the past decade, a large number of experimental investigations of critical layer thickness have been reported.[5,6] Experimental techniques have ranged from imaging dislocations with electron microscopy to fabricating heterostructure devices and inferring the presence of dislocations from device characteristics. The results have often been contradictory, with critical layer thicknesses ranging from about $t_{c,MB}$ to more than an order of magnitude greater than $t_{c,MB}$. We will review experimental results in this and the following sections.*

Orders and Ushers[7] used high-resolution x-ray diffraction to measure the strain relief in InGaAs layers on (001) GaAs substrates. They found that layers remained coherent to thicknesses about an order of magnitude larger than $t_{c,MB}$. Gal *et al.*[8] examined the photoluminescence (PL) peak position and width in the InGaAs/GaAs system, and obtained results similar to those of Orders and Usher. In the same materials system, however, Fritz *et al.*[9] applied both PL and low-temperature Hall measurements and obtained t_c's approximately equal to $t_{c,MB}$. Wang[10] fabricated AlGaAs/InGaAs/GaAs HFET's with the InGaAs channels a factor of two and four

*Most of the experimental investigations of critical layer thickness have been in the SiGe/Si and InGaAs/GaAs systems, with only a few reports for InGaAs/InP and InAlAs/InP heterostructures. We expect that InGaAs/InP and InAlAs/InP may behave similarly to InGaAs/GaAs, and hence include the latter in our literature review.

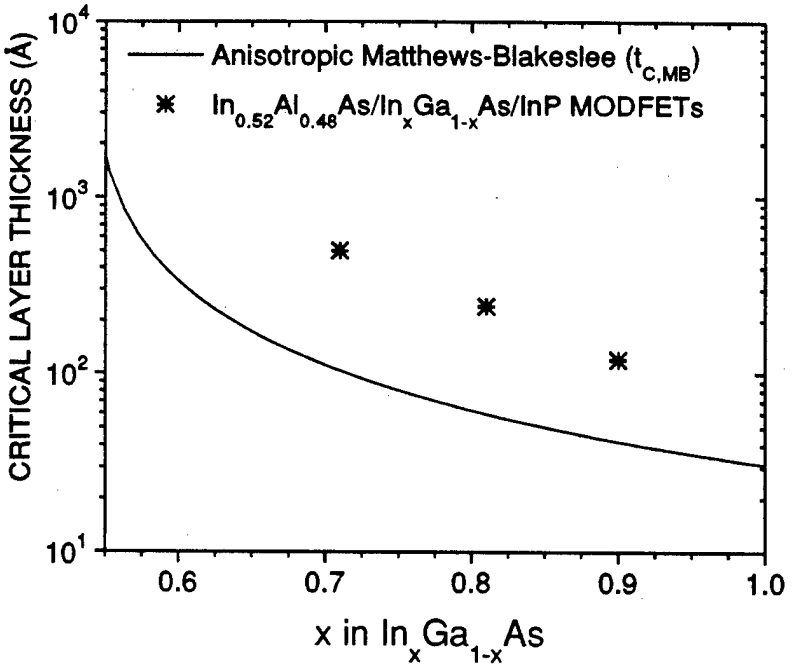

Figure 1-3: Critical layer thickness, as determined by Hall mobility, versus InAs mole-fraction in $In_{0.52}Al_{0.48}As/In_xGa_{1-x}As/InP$ modulation-doped structures (from Tacano *et al.*[11]).

thicker than $t_{c,MB}$, and observed no signs of degradation in the device characteristics.

In the InGaAs/InP system, conflicting results have also been reported. Tacano *et al.*[11] measured the 10K, 77K, and 300K Hall mobility of modulation-doped $In_{0.52}Al_{0.48}As/In_xGa_{1-x}As/InP$ heterostructures. As shown in fig. 1.3, they obtained critical thicknesses which exceeded $t_{c,MB}$ by a factor of three to five. Temkin[12] also studied the $In_xGa_{1-x}As/InP$ system, but looked for signs of misfit dislocations by monitoring the reverse-bias leakage current in photodiodes. His results were approximately in agreement with the Matthews-Blakeslee theory, as shown in fig. 1.4.

It is now clear that one reason for the apparent discrepancies in the literature is the different experimental resolutions of the various techniques.[13,14] In the InGaAs/InP examples listed above, it seems reasonable that a significant number of misfit dislocations are required before electron mobility is affected, but each dislocation could make a substantial contribution to the leakage current. It is apparent that any serious study of critical layer thickness requires a thorough analysis of the characterication techniques.

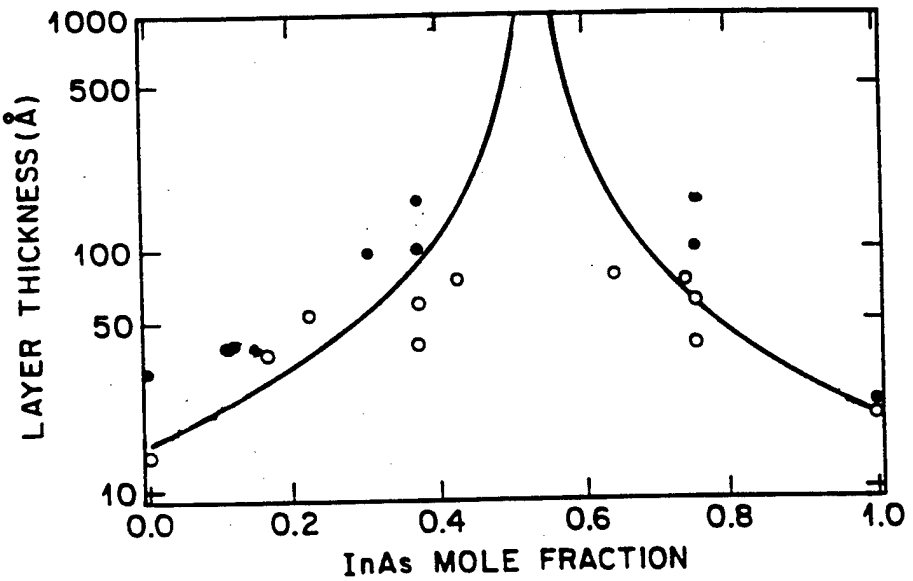

Figure 1-4: Strained-layer thickness versus InAs mole fraction for $In_xGa_{1-x}As/InP$ p-i-n photodiodes. Solid symbols indicate samples which contain misfit dislocations, based upon the reverse-leakage current. Samples which exhibit no signs of dislocations are plotted as open symbols. The line is the Matthews-Blakeslee critical layer thickness (from Temkin *et al.*[12]).

1.4 Metastability

The Matthews-Blakeslee theory of the critical layer thickness is based upon equilibrium considerations. A strained layer exceeds $t_{c,MB}$ if the lowest energy configuration includes misfit dislocations. In techniques such as molecular beam epitaxy (MBE) and metal-organic chemical vapor deposition (MOCVD), growth occurs under conditions which are far from equilibrium.[15] Hence, it is possible that kinetic barriers to the nucleation and growth of misfit dislocations could result in *metastable layers.*[16–18] The degree of relaxation in such layers can be a function of the growth temperature, as demonstrated by Whaley and Cohen in the InGaAs/GaAs system.[19] They used reflection high-energy electron-diffraction (RHEED) to monitor the value of $a_{||}$ in the epilayer during growth. The InGaAs relaxed much sooner when a high growth temperature (510°C) was used compared to a low temperature (470°C). Elman *et al.*[4] applied PL and transmission electron microscopy (TEM) to layers of InGaAs on GaAs and observed an increase in the critical thickness by a factor of seven when low

growth temperatures were used.

A potential problem with the use of metastable layers in devices is the possibility of layer relaxation during high-temperature processing steps or device operation. Peercy *et al.*[20] tested this hypothesis by annealing InGaAs/GaAs heterostructures in which the epilayer exceeded $t_{c,MB}$. They observed a dramatic decrease in photoluminescence intensity after the anneal, suggesting lattice relaxation. A similar photoluminescence experiment by Bertolet *et al.*[21] yielded the opposite results: InGaAs/GaAs heterostructures were thermally stable, despite exceeding $t_{c,MB}$.

Metastability was also investigated by Fitzgerald *et al.*[22] who compared the growth of strained layers of InGaAs on GaAs mesas and planar substrates. They found that the dislocation density was lower for the growth on mesas. The results are explained by the limited number of threading dislocations in the mesas and the lack of sufficient energy for the homogeneous nucleation of additional dislocations. Fitzgerald concludes that different apparent critical layer thicknesses may be observed, depending on the active dislocation sources.

1.5 Growth Modes

In fig. 1.2, cases A and B, we illustrated a simple model in which growth proceeds in a layer-by-layer fashion, with the introduction of misfit dislocations to relieve strain. The Matthews-Blakeslee theory is based upon this type of model. In recent years, it has become clear that growth of strained layers is often more complex. For example, both phase separation and three-dimensional growth have been observed in strained InGaAs and InAlAs epilayers.

Epitaxial growth has been classified into three distinct modes.[23,24] We will briefly review each mode and then discuss experimental results for InGaAs and InAlAs. In the *Frank-van der Merwe* mode, epitaxial growth takes place in a two-dimensional manner, with the completion of one monolayer before the next begins.† In the *Volmer-*

†Recent work on the AlGaAs/GaAs system suggests that the growth front may actually extend over a few monolayers in so-called layer-by-layer growth.[25]

Weber mode, epitaxial growth occurs in a three-dimensional manner by the formation and coalescence of islands. The third mode, *Stranski-Krastanov*, is a hybrid with initial layer-by-layer growth followed by the formation of islands. The growth mode of any system will be determined by the surface energies of the layer and substrate and the interfacial energy. Strain can be an important factor because it results in a higher surface energy for the layer.[26,27]

Tanaka and Ohkouchi[28] investigated the growth of GaAs on InP by scanning tunneling microscopy. They observed a Stranski-Krastanov mode, with 2-D growth for the first two monolayers, followed by island formation. Hopkinson *et al.*[29] grew quantum wells of InAs on InP. Based upon cross-sectional TEM, the growth remained planar to at least 30 Å. Similarly, de Miguel[30] observed 2-D growth of up to 30 Å of InAs on $In_{0.52}Al_{0.48}As$/InP. Since the Stranski-Krastanov mode occurs in these extreme cases of mismatch, we believe that growth of InGaAs or InAlAs on InP will not occur in the Volmer-Weber mode under normal conditions. Throughout this thesis, we will often use the term 3-D growth when actually referring to Stranksi-Krastanov growth.

We define a threshold thickness, t_{th}, as the thickness at which the growth mode changes from 2-D to 3-D. In general, we are interested in both t_{th} and t_c, the critical thickness for formation of misfit dislocations. We wish to know which thickness is smaller and the degree of layer degradation when each thickness is exceeded.

One view of strained layer growth is: a layer initially grows in a 2-D mode; after the critical layer thickness is exceeded, misfit dislocations form to relieve strain; the dislocations serve as sites for the nucleation of clusters and the growth mode becomes 3-D.[31,32] An alternative view, supported by experimental work in both the SiGe/Si[33] and InGaAs/GaAs[34,35] systems, suggests that strained layers may switch to the 3-D growth mode in the absence of misfit dislocations.[‡] This so-called "coherent Stranski-Krastanov" mode is explained by the accomodation of mismatch by elastic deformation around islands, as illustrated in fig. 1.2D.

[‡]We note that the authors[33–35] used electron microscopy to image islands in which no dislocations were visible. One cannot, however, prove the absence of dislocations in this way. Hence, it is more precise to say that 3-D growth occurred in the absence of significant numbers of misfit dislocations.

Snyder *et al.*[34] examined InGaAs layers on GaAs by both RHEED and TEM. Based upon the experimental results, they postulate that the strain initially induces a roughening of the layer. Eventually, as strain energy builds up with each successive mismatched monolayer, islands form in a "kinetically controlled coarsening process." This scenario allows for a transition to 3-D growth without the formation of misfit dislocations.

Based upon a theoretical analysis of strain energies in 2-D and 3-D growth, Berger *et al.*[36] demonstrate that the lowest energy surface of an epilayer may be 3-D in the presence of strain. They apply their results to the InGaAs/GaAs system and estimate that 3-D growth should occur when the mismatch exceeds 2%. Several experimental studies have confirmed 3-D growth for mismatches greater than about 2%.[37–42] Only Chang *et al.*[39] characterized relatively thick layers with mismatches less than 2%. They saw no signs of 3-D growth for a 1.0 μm layer with a 1% mismatch.

Very recent work by Gendry *et al.*[43,44] examined the growth mode for compressively-strained layers of InGaAs on InP. Using RHEED oscillations, they observed a transition from 2-D to 3-D growth for mismatches of 2% and 3%. The value of t_{th} increased with decreasing growth temperature. Apparently, growth at higher temperatures increases the mobility of surface atoms, allowing the formation of islands. For a mismatch of 1%, the layer remained in a 2-D growth mode up to 2200 Å; thicker layers were not grown. The Gendry results support the idea that coherent islands may form in some situations.

Lievin and Fonstad[45] measured RHEED oscillations during the growth of compressively-strained InAlAs on InP with mismatches from 1 to 3%. They observed the apparent onset of 3-D growth at thicknesses ranging from 10 Å (3%) to 100 Å (1%). 3-D growth began earlier for layers in tension with comparable mismatch. They attribute this to the lower In composition and resulting decrease in average cation mobility at a growing surface.

It is clear that strained InGaAs and InAlAs layers frequently grow in a 3-D mode. If the islands are coherent, the material quality may remain relatively high. Even in this case, however, the variation in thickness of a quantum well could broaden the

luminescence peak width. Coherent islands can only accomodate a relatively small amount of strain. Eventually, islands will coalesce, forming undesirable defects such as edge dislocations, stacking faults, and threading dislocations.[34,39,46]

Another possible occurrence during the growth of epitaxial layers is a modulation of the composition in a direction parallel to the sample surface. This phenomenon is often referred to as phase separation, and is analogous to spinodal decomposition in bulk alloys.[47] Theoretical work[48,49] has shown that layers with composition modulation may have a lower energy than homogeneous layers. We show a schematic of the modulation in fig. 1.2C. Note the change in lattice parameter, corresponding to a change in composition, for layers near the surface.

Composition modulation has been observed in ternary and quaternary alloys of III-V compounds.[50–53] In the case of InGaAs/InP, the period of oscillation varied from 2000 to 4000 Å, and decreased with increasing thickness for a fixed mismatch.[51] The composition modulation was present for layers with thicknesses of $1 - 2 \times t_{c,MB}$, but no lattice defects were observed. For thicker InGaAs layers, both composition modulation and stacking faults were found. These results suggest that composition modulation can accomodate a limited amount of layer strain, but eventually other defects will be introduced.

1.6 Summary

In summary, the theory of Matthews and Blakeslee predicts an equilibrium critical layer thickness for strained epitaxial layers. Experimental work suggests that layers thinner than $t_{c,MB}$ are always free of misfit dislocations. The M-B limits, however, place severe constraints on the use strained layers in electronic and optical devices. Layers exceeding $t_{c,MB}$ are clearly desirable in many applications.

Several important questions remain for the $In_xGa_{1-x}As/InP$ and $In_yAl_{1-y}As/InP$ material systems: What are the limits on layer mismatch and thickness for high-quality heterostructures? What mechanisms (misfit dislocations, three-dimensional growth, composition modulation, etc.) degrade the mismatched layers? Are strained

layers thermally stable? Why or why not? This thesis will address these questions.

1.7 Outline of Thesis

As mentioned above, any serious study of strained layer epitaxy requires a careful analysis of the characterication techniques. In **chapter 2**, we analyze the use of high-resolution x-ray diffraction (HRXRD) to assess the composition, relaxation, and structural quality of mismatched epilayers. We demonstrate that the crystalline quality of InGaAs and InAlAs layers consistently remains high to thicknesses up to 3-9 times the Matthews-Blakeslee critical layer thickness. For thicker layers, lattice relaxation occurs in an asymmetric manner, with a change in crystal symmetry from tetragonal to orthorhombic.

Chapter 3 describes a new characterization technique we developed known as variable azimuthal angle ellipsometry. It reveals large optical anisotropies in mismatched InGaAs and InAlAs layers. We attribute the anisotropy to strain-induced surface roughening.

In **chapter 4**, we assess the thermal stability of strained InGaAs and InAlAs layers. Using HRXRD and Hall mobility measurements, we demonstrate that high-quality layers beyond the Matthews-Blakeslee critical thickness are relatively stable to temperatures of at least 800-850°C. We explain this result by the limited source of threading dislocations and the lack of sufficient thermal energy to homogeneously nucleate half-loop dislocations during annealing.

As mentioned earlier, the motivation for the study of strained layers is their potential application in devices. We applied our findings to the HFET. As described in **chapter 5**, we grew HFETs with strained $In_xGa_{1-x}As$ channels and $In_yAl_{1-y}As$ pseudo-insulators. The $In_yAl_{1-y}As$ layers were about twice the Matthews-Blakeslee critical thickness. HRXRD showed the heterostructures to be of good crystalline quality. The device results were excellent, suggesting that if misfit dislocations were present, they did not affect the device performance in any appreciable way.

In **chapter 6**, we discuss our results and the relevance of theories for lattice

relaxation and strained layer growth. We concur with the idea that a source of lattice imperfections is sometimes necessary to provide the nucleation sites for misfit dislocations. This model can explain the thermal stability of our high-quality layers as well as the instability of other layers reported in the literature. If the surface of a strained layer roughens or the layer grows in a 3-D mode, the resulting defects can serve as a source of misfit dislocations for strain relaxation during subsequent growth or annealing.

The key conclusions are summarized in **chapter 7**. We also discuss promising directions for future research including experiments which could verify our model for thermal stability and lattice relaxation.

The growth of over 200 InGaAs/InP and InAlAs/InP heterostructures by solid-source MBE was an important part of this work. We generally used well-established growth procedures which are documented in the literature. We describe our epilayer growth in **appendix A**. In **appendix B**, we compile the important materials properties of InP, InAs, GaAs, and AlAs. We frequently use interpolations from these values throughout this thesis. **Appendix C** gives the equations for the Matthews-Blakeslee critical layer thickness and its extension to the case of elastically anisotropic materials.

Chapter 2

Characterization by High-Resolution X-Ray Diffraction

High-resolution x-ray diffraction (HRXRD) is routinely used to measure the composition and strain of epitaxial layers of semiconductor alloys such as $In_xGa_{1-x}As$.[54-59] We apply it for this purpose throughout the thesis and investigate the accuracy of such measurements. We focus our efforts on the use of HRXRD to determine the crystalline quality of epitaxial layers. Compared to characterization techniques such as transmission electron microscopy and the fabrication and testing of heterostructure devices, HRXRD is relatively fast and simple. Hence, we are able to characterize a large number of layers covering a wide range of thickness and mismatch. The results allow us to determine the range of thickness and mismatch for MBE growth of high-quality InGaAs and InAlAs layers on InP. In later chapters, we apply HRXRD to measure the thermal stability of strained layers and correlate HRXRD measurements of crystalline quality with electron mobility and device performance.

In section 2.1, we briefly review the theory and experimental techniques required to measure layer composition. We also discuss the role of simulations based upon the dynamical theory of x-ray diffraction. Then, we present our contributions in three areas: Section 2.2 describes our measurements of layer quality and its relationship

to lattice mismatch and thickness. We demonstrate that high-quality InGaAs and InAlAs layers can be grown to thicknesses beyond the Matthews-Blakeslee critical thickness. In section 2.3, we show that partially relaxed layers of both InGaAs and InAlAs exhibit orthorhombic distortion as a result of an asymmetry in dislocation density. This fact must be taken into account when measuring the composition of such layers. In section 2.4 we determine the range of thicknesses for which layer composition can be accurately determined from a single HRXRD scan. This information is important for the design of calibration layers and can also be applied to multilayer structures including devices. The work is summarized in section 2.5.

2.1 Background

When electromagnetic radiation with a wavelength comparable to the atomic spacing strikes a crystal, atomic scattering will result in constructive interference and a diffracted beam in certain directions. The fundamental equation describing the diffraction is Bragg's law:

$$n\lambda = 2dsin\theta_B \tag{2.1}$$

where θ_B is the Bragg diffraction angle, λ is the wavelength of the radiation, n is the order of the diffraction, and d is the interatomic spacing. d is related to the lattice constant, a, by:

$$d = \frac{a}{\sqrt{h^2 + k^2 + l^2}} \tag{2.2}$$

where (hkl) are the indices of the diffracting plane.

Constructive interference results when (2.1) is satisfied. If a single crystal is scanned through θ to produce a plot of intensity versus angle, a peak will be observed at θ_B. The spectral width of the source combined with beam divergence will result in a peak width of several minutes of arc. This resolution is not good enough to measure the small lattice constant differences typically found in epitaxial semiconductor layers.

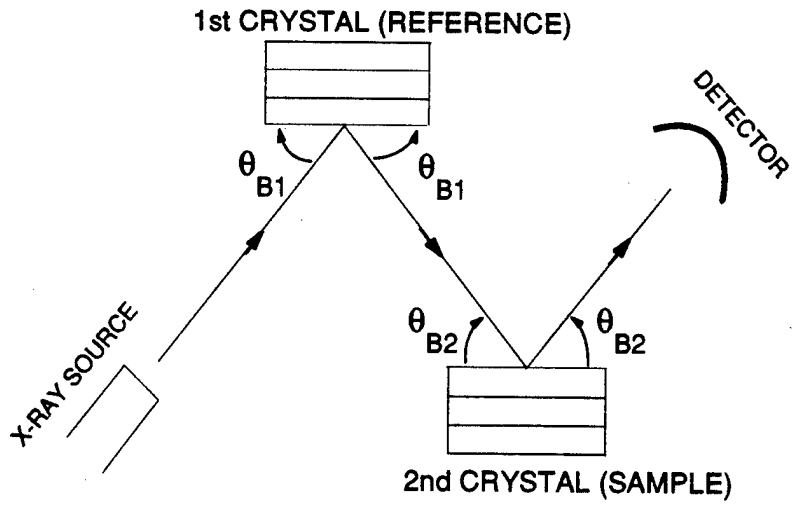

Figure 2-1: Schematic of double-crystal x-ray diffraction system. The case of symmetric reflections from both crystals is shown.

If instead an x-ray source is diffracted off a reference (first) crystal and the diffracted beam is then used to produce a rocking curve off a second crystal (the sample), peak widths as small as a few arc-seconds can be achieved. This measurement technique is known as double-crystal x-ray diffraction and is illustrated in fig. 2.1. For some applications, the addition of a third and even fourth crystal can be advantageous. We use the term high-resolution x-ray diffraction to refer to any system employing two or more crystals.

When using HRXRD to measure layer composition, the only parameter required from the experiment is $\Delta\theta_B$, the difference in Bragg angle of the substrate and epilayer. To derive the relationship between $\Delta\theta_B$ and composition, we combine (2.1) and (2.2):

$$a = \frac{n\lambda\sqrt{h^2 + k^2 + l^2}}{2sin\theta_B} \tag{2.3}$$

We consider the symmetric case in which the diffraction planes are parallel to the substrate surface, and the incidence angle equals the exit angle. Differentiating (2.3) with respect to θ and dividing the resulting equation by (2.3) yields:

$$\left(\frac{\Delta a}{a}\right)_{\perp} \cong -\frac{\Delta\theta_B}{tan\theta_B} \tag{2.4}$$

where we have used a small-angle approximation. We can also express (2.4) as:

$$\left(\frac{\Delta a}{a}\right)_{\perp} \cong -K\Delta\theta_B \tag{2.5}$$

where K is a constant determined by the lattice constant of the substrate and the diffraction plane, and $\Delta\theta_B$ is expressed in arc-sec. We include the $\perp$ subscript in (2.4) and (2.5) because a symmetric measurement is only sensitive to the lattice mismatch perpendicular to the substrate/epilayer interface, $(\Delta a/a)_{\perp}$ (see fig. 1.2). Measurement of the lattice mismatch parallel to the interface, $(\Delta a/a)_{||}$, requires asymmetric measurements and will be discussed in section 2.3.

In order to relate composition to lattice mismatch, it is convenient to define a parameter known as the *relaxed lattice mismatch.* It is the mismatch a layer would have if it were totally relaxed or in bulk form, and is conventionally expressed as:[59]

$$\left(\frac{\Delta a}{a}\right)_r = \frac{1-\nu}{1+\nu}\left(\frac{\Delta a}{a}\right)_{\perp} + \frac{2\nu}{1+\nu}\left(\frac{\Delta a}{a}\right)_{||} \tag{2.6}$$

where ν is Poisson's ratio for the layer. For III-V semiconductors, ν is typically about 1/3. If a layer is fully relaxed, $(\Delta a/a)_{\perp} = (\Delta a/a)_{||} = (\Delta a/a)_r$. For partially relaxed layers, $(\Delta a/a)_{||} < (\Delta a/a)_r < (\Delta a/a)_{\perp}$. If a layer is coherent, $(\Delta a/a)_{||} = 0$, and:

$$\left(\frac{\Delta a}{a}\right)_r \cong \frac{1}{2}\left(\frac{\Delta a}{a}\right)_{\perp} \tag{2.7}$$

The final step is to relate the relaxed lattice mismatch to the layer composition. We use Vegard's law which assumes that the lattice constant of an alloy (*e.g.* $In_xGa_{1-x}As$) is a linear function of the lattice constants of the constituent binaries (*e.g.* InAs and GaAs). For $In_xGa_{1-x}As$, we have:

$$x = 14.48\left(\frac{\Delta a}{a}\right)_r + 0.5322 \tag{2.8}$$

using the lattice parameters in appendix B. Similarly, for $In_yAl_{1-y}As$:[60]

$$y = 14.82\left(\frac{\Delta a}{a}\right)_r + 0.5210 \tag{2.9}$$

We collected x-ray data with Bede model 300 and model 150 two-crystal systems using Cu-Kα radiation. The first crystal was always InP oriented for the (004) reflection. Rocking curves were measured for symmetric (004) as well as asymmetric (115) and (224) reflections off the second crystal (sample being characterized). In a typical scan, data points were collected every 2 arc-sec with a count time of 2 seconds per point. Such scans required 30-120 minutes, depending on the sample mismatch and resulting angular separation between substrate and layer peaks. When measuring very thin layers (100-200 Å), we often used count times of 5-10 seconds, requiring as long as 8 hours per scan. The spot size of the x-ray beam on the sample was approximately 1 mm by 2 mm.

A typical HRXRD scan is shown in fig. 2.2a. The sample consisted of a single layer of $In_yAl_{1-y}As$ on InP; the symmetric (004) reflection geometry was used. (We do not measure absolute Bragg angles, only differences between Bragg angles. Throughout this work, we set the InP peak to be at 0 arc-seconds for convenience.) In this case, both the substrate and the layer produce distinct peaks. The separation between the peaks, $\Delta\theta$, is -152 arc-sec. Since the layer has a smaller Bragg angle than the substrate, the lattice constant of the layer must be larger (eq. 2.1), making it InAs-rich compared to the lattice-matched composition of $In_{0.521}Al_{0.479}As$. From appendix B, the lattice constant of InP is 5.8688 Å. Using (2.1) and (2.2) with a wavelength of 1.54056 Å (CuKα_1), we obtain 31.668° for the (004) InP Bragg angle. The K in (2.5) is 7.8595×10^{-6}, and the perpendicular mismatch is +0.00119. If we now assume the layer is coherent ($(\Delta a/a)_{||} = 0$), (2.6) gives a relaxed mismatch of +0.000618. Using (2.9), the layer composition is $In_{0.530}Al_{0.470}As$. We will discuss the accuracy of such measurements in section 2.4.

In fig. 2.2b, we replot the data of fig. 2.2a on a logarithmic scale. We observe not only the substrate and layer peaks, but also a series of low-intensity peaks with constant spacing. These peaks result from interference effects between the sub-

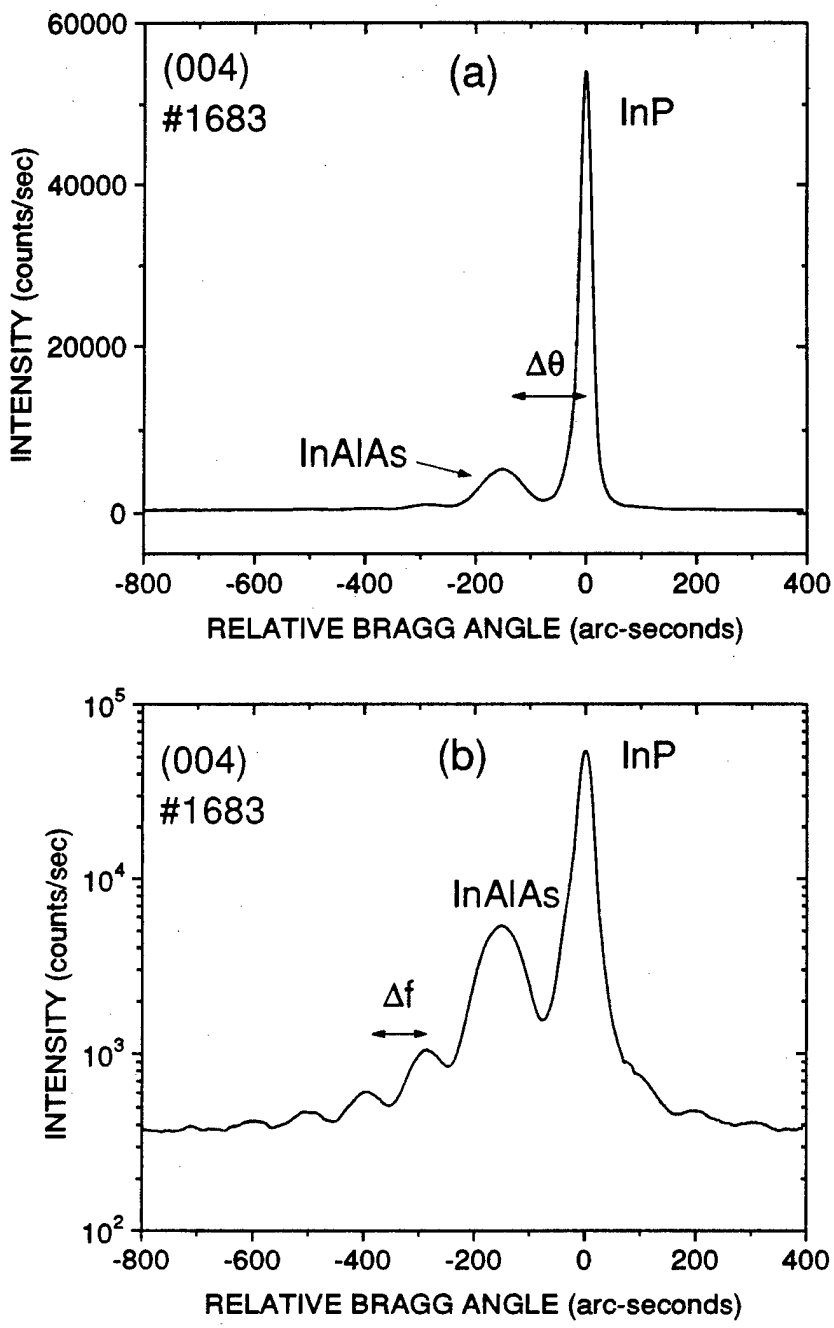

Figure 2-2: HRXRD (004) rocking curve for sample 1683, 1760 Å of $In_{0.530}Al_{0.470}As$ on InP plotted on linear (a) and semi-log (b) scales. Pendellosung fringes are clearly visible in (b).

strate/layer and layer/air interfaces and are known as *Pendellosung or interference fringes.* For a single layer, the spacing between the fringes, Δf, is related to the layer thickness, t, by:[55,59]

$$\Delta f = \frac{\lambda|\gamma_h|}{t sin(2\theta_B)} \tag{2.10}$$

where γ_h is the cosine of the angle between the diffracted beam and the surface normal. In the case of symmetric reflections, $\gamma_h = \cos(90\text{-}\theta_B)$. For the (004) reflection, (001) InP substrates, and CuKα radiation:

$$t = \frac{18.67}{\Delta f} \tag{2.11}$$

where t is in microns and Δf is in arc-sec. For sample 1683 in fig. 2.2, Δf = 106 arc-sec and t = 1760 Å.

We can now check our assumption of coherency for the epilayer in sample 1683. From appendix C, the modified Matthews-Blakeslee critical thickness, $t_{c,MB}$, for $In_{0.530}Al_{0.470}As$ is 3000 Å. Since $t < t_{c,MB}$, the layer is expected to be coherent, and our calculated composition should be correct.

The identification of diffraction peaks is usually straightforward in the case of a single layer on a substrate such as sample 1683. In many cases, however, we wish to characterize multi-layer heterostructures. In such cases, an x-ray scan often reveals a plethora of diffraction peaks. The clear distinction between primary diffraction peaks and Pendellosung fringes no longer applies. The best way to determine layer compositions and thicknesses is to compare the experimental rocking curve to simulated curves.

Both the kinematical and dynamical theories of x-ray diffraction have been used to simulate rocking curves. The kinematical theory simply sums diffracted intensity contributions from each unit cell, neglecting absorption losses and secondary reflections. In contrast, the dynamical theory provides an exact solution to Maxwell's equations throughout the entire structure.[55,59,61] The kinematical theory is computationally much simpler and has been shown to provide adequate approximations in

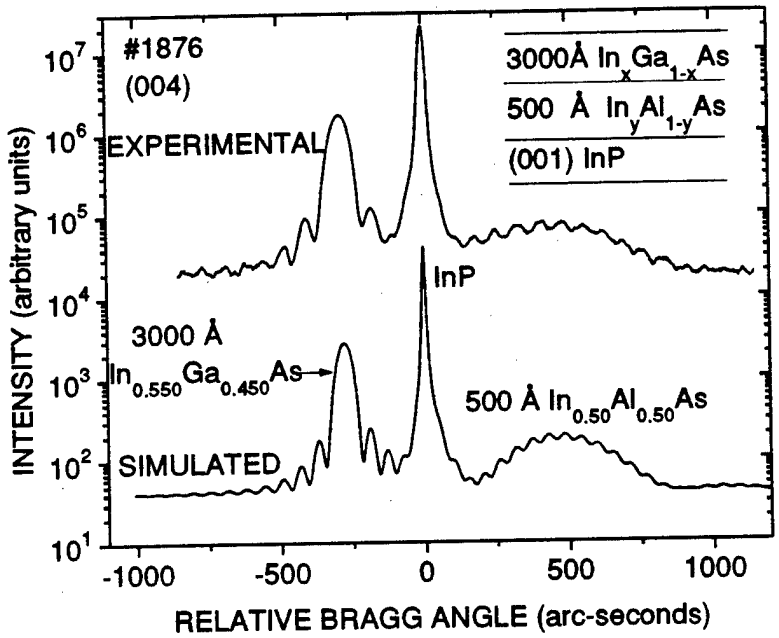

Figure 2-3: HRXRD (004) experimental and simulated rocking curves for sample 1876; heterostructure cross-section is shown.

some cases. With the continuing improvements in the speed of personal computers, however, it is now reasonable to apply the dynamical theory in all cases. We have used the commercial program RADS (Rocking curve Analysis by Dynamical Simulation) by Bede Scientific Instruments Limited throughout this thesis.[62,63]

We give an example of the use of simulations in fig. 2.3. The structure examined consists of (bottom to top) an (001) InP substrate, a 500 Å layer of $In_yAl_{1-y}As$, and a 3000 Å layer of $In_xGa_{1-x}As$. For the simulation, we kept the layer thicknesses fixed at their nominal values (which we believe to be accurate to within 10%), and adjusted the layer compositions until reasonable agreement with the experimental data was obtained. The resulting compositions are x = 0.550 and y = 0.50.

2.2 Crystalline Quality

Misfit dislocations relieve lattice strain, as illustrated in fig. 1.2. For a constant composition, as strain is relieved, the amount of tetragonal distortion and $(\Delta a/a)_\perp$ decrease. At the same time, $(\Delta a/a)_\parallel$ increases but $(\Delta a/a)_r$ is constant. One can

define lattice relaxation, R, as:[64]

$$R = \frac{\left(\frac{\Delta a}{a}\right)_{\|}}{\left(\frac{\Delta a}{a}\right)_{r}} \tag{2.12}$$

We often express R as a per-cent. For a fully strained layer, $R = 0\%$; for a completely relaxed layer, $R = 100\%$.

In theory, it should be possible to determine critical layer thickness by measuring the onset of relaxation by HRXRD. Multiple HRXRD scans are required to independently measure both relaxation and composition, as will be desribed in the next section. If the layer composition is already known, a single (004) scan will give R. For example, if thin (t< t_c) and thick (t> t_c) layers are grown under the same conditions, the composition of the thin layer can be measured by a single (004) scan since R will be zero. If we assume that the thick layer has the same composition, an (004) scan on the thick layer will give its R. Such an experiment is shown in fig. 2.4 for the InAlAs/InP system. The four epilayers were grown the same day with identical In, Al, and As cell temperatures. The 300, 1000, and 3000 Å layers have nearly equal InP-InAlAs peak separations, suggesting negligible relaxation (eq. 2.7 applies) and constant composition throughout the growth day. The peak separation for the 10,000 Å layer, however, is considerably reduced.

Using the $(\Delta a/a)_r$ measured for the thinner layers and (2.6), we can calculate $(\Delta a/a)_{\|}$. Equation (2.12) then gives $R = 32\%$. Apparently, misfit dislocations have formed, relaxing strain and hence reducing the tetragonal distortion and $(\Delta a/a)_{\perp}$. These measurements suggest the onset of relaxation for this composition occurs between $t/t_{c,MB} = 18$ (3000 Å layer) and $t/t_{c,MB} = 65$ (10,000 Å layer).

In similar studies of SiGe/Si[65] and InGaAs/GaAs,[7] the authors also observed the apparent onset of relaxation at $t_x >> t_{c,MB}$ and called t_x the critical layer thickness. As pointed out by Fritz,[13] however, direct measurement of relaxation by HRXRD can give anomalously large values of critical thickness. A substantial number of dislocations are required before the parallel lattice constant changes appreciably and HRXRD can detect the resulting change in strain. Hence, as will be confirmed in the

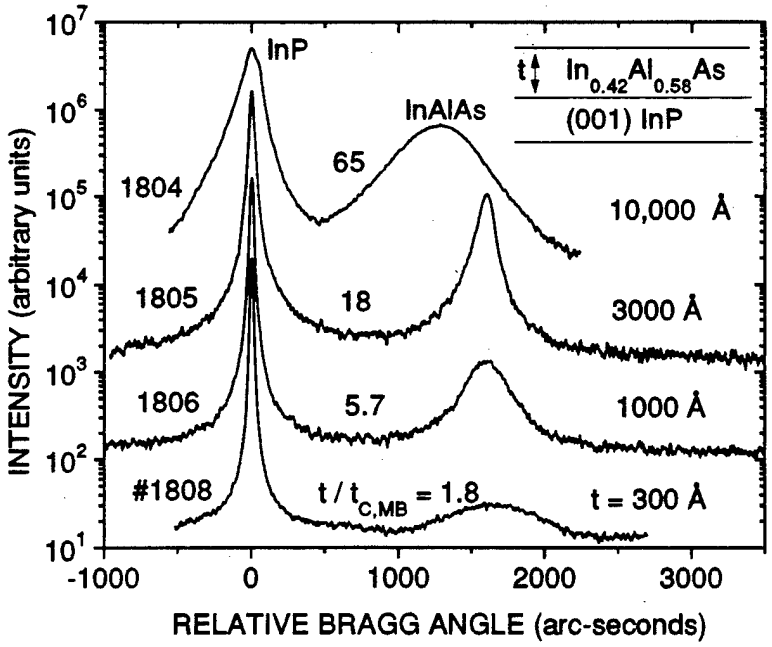

Figure 2-4: HRXRD (004) rocking curves for four $In_{0.42}Al_{0.58}As$ heterostructures with varying epilayer thickness. The InP-InAlAs peak separation for sample 1804 is reduced due to lattice relaxation.

experiments below, results such as those of fig. 2.4 do not yield a reliable measure of the critical layer thickness.

In addition to peak separation, the width of diffraction peaks in HRXRD contains important information. The full-width at half-maximum (FWHM) of a layer peak is often cited as a figure of merit for the epilayer. The FWHM is sensitive to crystalline imperfection. For example, the presence of misfit dislocations will result in a local tilting of lattice planes and a broadening of the peak.[59] Even for perfect crystals, however, the FWHM is a function of layer thickness, with thinner layers producing broader peaks. For example, in fig. 2.3 the 500 Å InAlAs peak is much broader than the 3000 InGaAs Å peak.

We determined the theoretical (004) FWHM for layers of InGaAs and InAlAs by simulations using dynamical diffraction theory.[63] We found that the theoretical FWHM of both InGaAs and InAlAs layers can be fit by the function:

$$FWHM = 5.1 + \frac{1.582 \times 10^5}{t} + \frac{2.598 \times 10^6}{t^2} \qquad (2.13)$$

where t is the layer thickness in angstroms and FWHM is in arc-seconds. Hence, as a figure of merit for crystalline quality, we take the ratio of the experimental to the theoretical FWHM for the (004) reflection. An additional measure of structural quality is provided by the presence or absence of Pendellosung fringes in the rocking curves. These fringes indicate a coherent, high-quality layer.[59]

For sets of samples with constant thickness and changing composition, as mismatch increases we typically observe a transition at which the (004) FWHM increases, presumably due to a degradation of crystalline quality.[66-68] In fig. 2.5, we show an example with sample 1876 of fig. 2.3 and four other samples grown the same day. The five heterostructures are nominally identical except for the composition of a 3000 Å $In_xGa_{1-x}As$ layer. In addition to the epilayer and substrate peaks, we observe a series of Pendellosung fringes on four of the samples. For samples 1876-1879 ($0.477 \leq x \leq 0.550$), the experimental-to-theoretical FWHM ratio is between 1.1 and 1.5 and interference fringes are present. For sample 1880 ($x = 0.466$), however, the FWHM ratio increases to 2.4 and the fringes disappear. The transition occurs when the layer thickness exceeds $t_{c,MB}$ by about a factor of eight.

We observe a similar transition for mismatched layers of $In_xGa_{1-x}As$ in compression ($x > 0.53$). In fig. 2.6 we show the rocking curves for four heterostructures, each consisting of a single 1000 Å layer of $In_xGa_{1-x}As$ on InP, with x varying from 0.515 to 0.69. For samples 1630, 1632, and 1633, the FWHM ratios are less than 1.5 and Pendellosung fringes are present, indicating high crystalline quality. (The fringes are less prominent than in fig. 2.5 because the InGaAs in fig. 2.6 is thinner and a second layer (InAlAs) is not present.) For 1634, however, the epilayer peak is substantially broadened and the fringes are absent, indicating a severe degradation in layer quality. In a separate experiment, we grew a multi-layer structure which included a 1000 Å layer of $In_{0.653}Ga_{0.347}As$ ($t/t_{c,MB} = 6.1$). The FWHM ratio was 1.3 and fringes were present, yielding a transition in the range $6 < t/t_{c,MB} < 8$ for 1000 Å compressively-strained layers of InGaAs on InP.

We also investigated sets of 1000 Å $In_yAl_{1-y}As$ epitaxial layers. In fig. 2.7 we show the rocking curves for five heterostructures under tension (AlAs-rich) with y varying

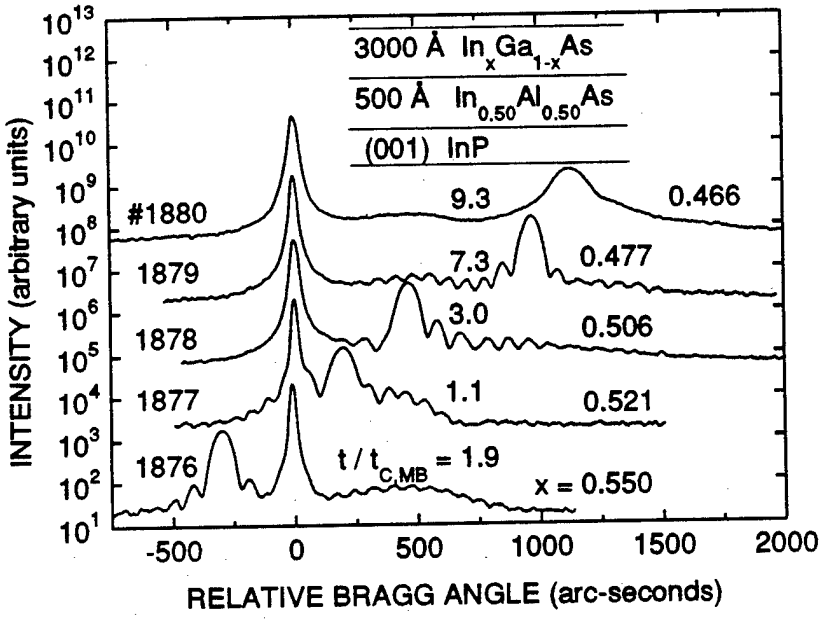

Figure 2-5: HRXRD (004) rocking curves for five heterostructures shown in inset. The largest peaks (at 0 arc-sec) are the InP substrate. The second-largest peaks (varying from -300 to +1200 arc-sec) are the 3000 Å InGaAs layers. The broad peaks at about +500 arc-sec are the 500 Å InAlAs buffer layers. $t/t_{c,MB}$ is the ratio of the InGaAs thickness to the anisotropic Matthews-Blakeslee critical layer thickness.

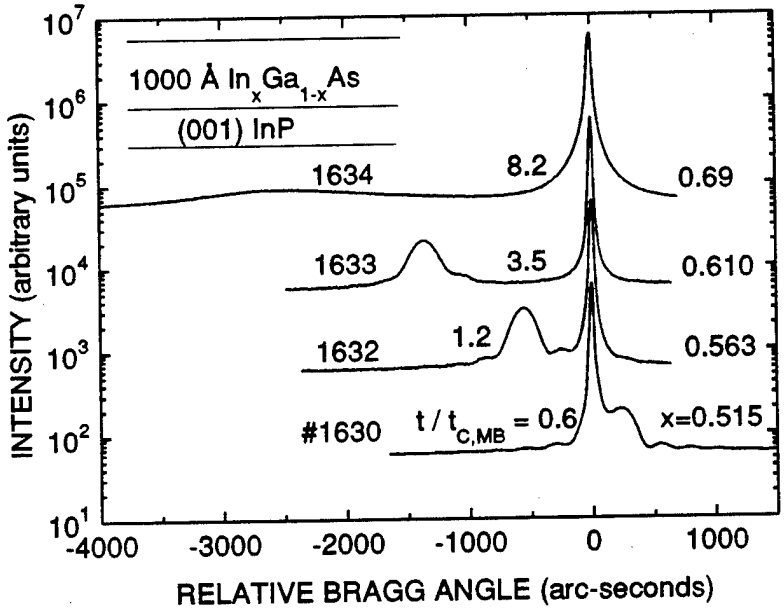

Figure 2-6: HRXRD (004) rocking curves for four 1000 Å layers of $In_xGa_{1-x}As$ in compression. The FWHM ratios for samples 1630, 1632, and 1633 are less than 1.5; Pendellosung fringes are also present for these three samples.

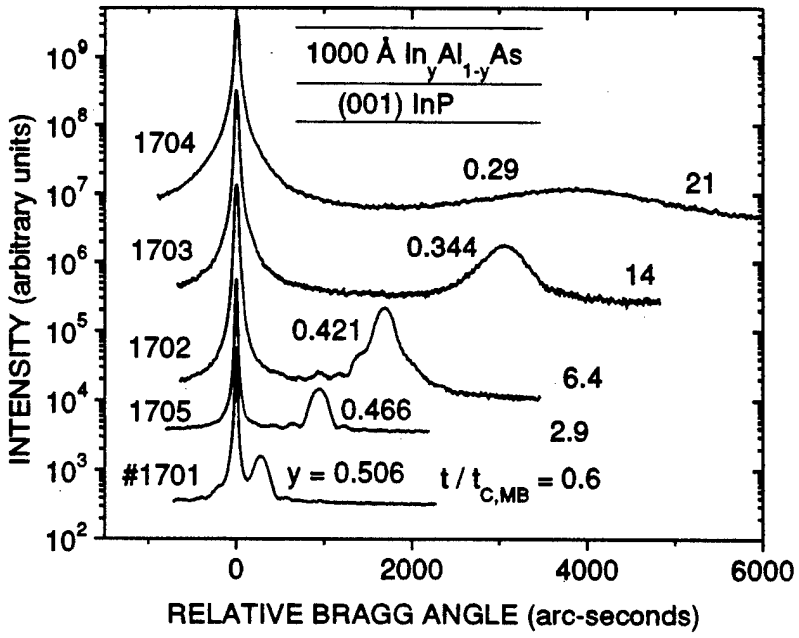

Figure 2-7: HRXRD (004) rocking curves for five 1000 $\AA$ layers of $In_yAl_{1-y}As$ in tension. Samples 1701, 1705, and 1702 exhibit Pendellosung fringes and peak widths within 30% of the theoretical value.

from 0.506 to 0.29. Samples 1701, 1705, and 1702 exhibit small FWHM ratios (1.2-1.3) and Pendellosung fringes, indicating high crystalline quality. For samples 1703 and 1704, the epilayer peaks are substantially broadened and the fringes are absent, indicating poor structural quality. For this set the transition is in the range $6 < t/t_{c,MB} < 14$.

We grew a complementary set of 1000 $\AA$ $In_yAl_{1-y}As$ layers in compression (InAs-rich). The results are shown in fig. 2.8. For the first sample, 3098, the lattice mismatch between the epilayer and substrate was too small to produce two distinct peaks. (The thickness required for resolvable peaks will be discussed in section 2.4.) For sample 3099, the FWHM ratio is 1.3 and fringes are present, indicating excellent structural quality. The other three samples exhibit very broad epilayer peaks with no fringes. We can compare these results to the InAlAs in tension. Samples 3100 (fig. 2.8) and 1702 (fig. 2.7) each have $t/t_{c,MB} \cong 6$, but the crystalline quality of 1702 is clearly much higher. Similarly, samples 3102 and 1703 are 14-15 times $t_{c,MB}$, but 1703 has a superior rocking curve. These results show that the crystalline quality

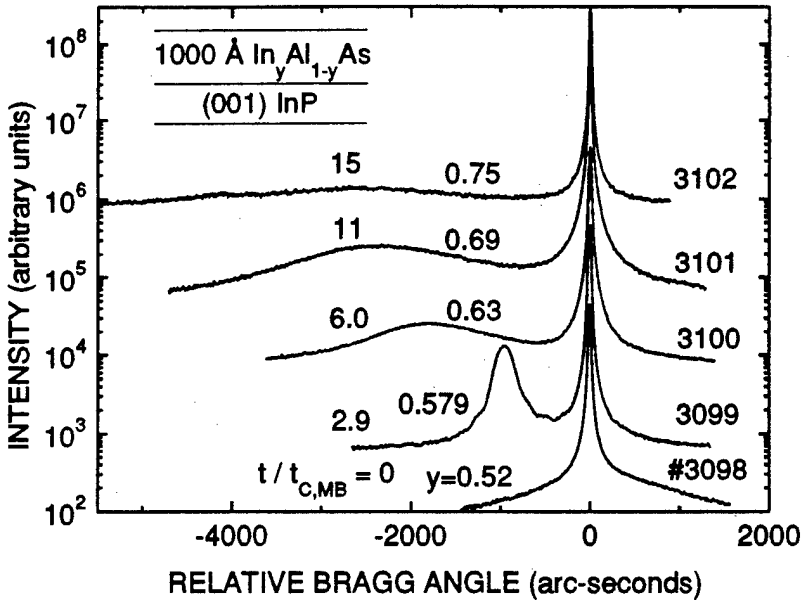

Figure 2-8: HRXRD (004) rocking curves for five 1000 $\AA$ layers of $In_yAl_{1-y}As$ in compression. Sample 3099 has Pendellosung fringes and a peak width within 30% of the theoretical value.

of 1000 Å InAlAs layers remains unperturbed to larger mismatches in tension than in compression. We have confirmed this finding for other InAlAs layers as well.[66] The reason for the differences in tension and compression is not clear, but we note that Lievin and Fonstad, using reflection high-energy electron diffraction (RHEED) oscillations, also observed differences in the growth of InAlAs in compression and tension, and related it to differences in cation mobilities.[45]

The previous figures illustrate the apparent degradation in layer quality when the lattice mismatch is too large. In some cases, however, factors other than mismatch result in poor crystalline quality. In fig. 2.9, we show (004) HRXRD rocking curves for samples 2006 and 2010. Each sample consists of a single, nominally lattice-matched layer of InAlAs on InP. The layer in 2010 gives a sharp diffraction peak and about 20 visible Pendellosung fringes. In contrast, 2006 shows only the InP peak with broad shoulders on either side. We believe that 2006 was grown at too low a temperature, resulting in the poor crystalline quality.

HRXRD can also be applied to device heterostructures. We will discuss applica-

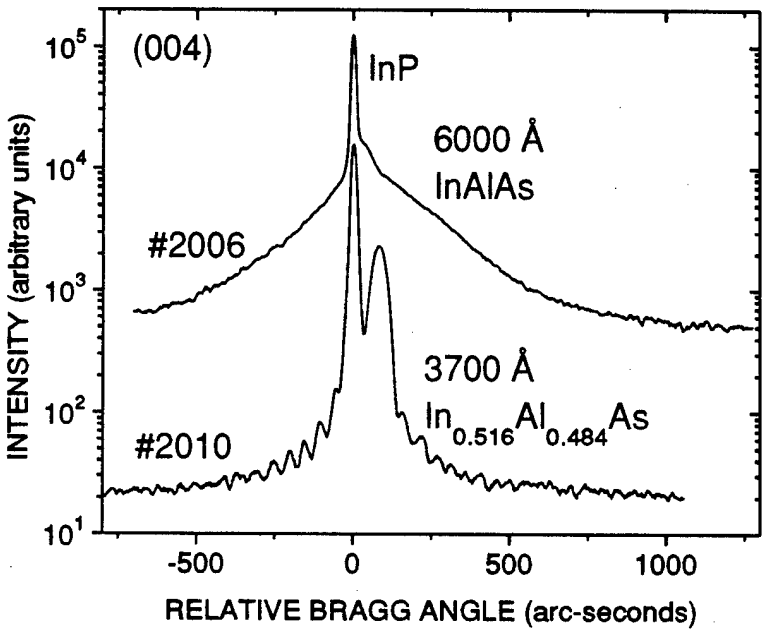

Figure 2-9: HRXRD (004) rocking curves for samples 2006 and 2010. The samples consist of single layers of InAlAs with approximately the same composition. #2010 exhibits multiple fringes and a narrow epilayer peak width, indicating excellent crystalline quality. The quality of #2006 is poor, apparently because the growth temperature was too low.

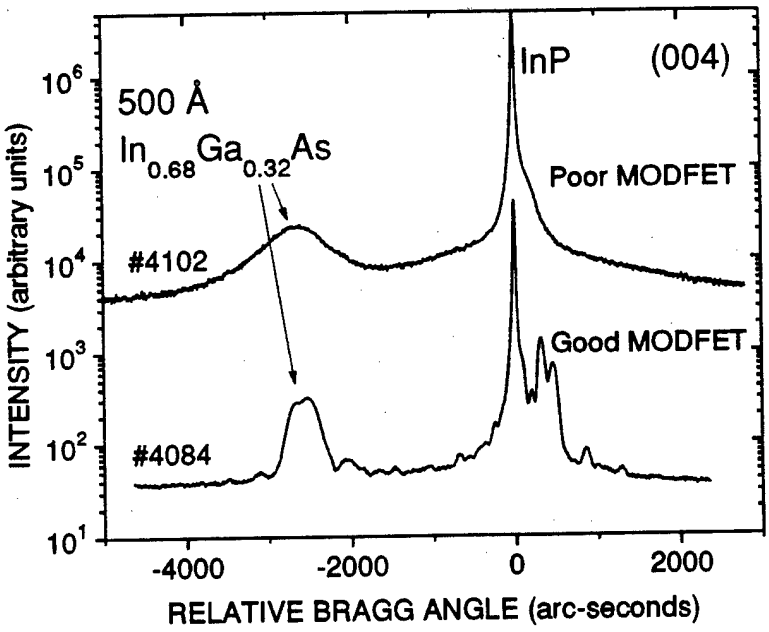

Figure 2-10: HRXRD (004) rocking curves for two MODFETs with nominally identical structures, including 500 Å channels of $In_{0.68}Ga_{0.32}As$. The electron mobilities of #4084 are 9200 and 40,000 cm^2/V-sec at 300 and 77 K, respectively. The mobilities of #4102 are 1900 and 2500 cm^2/V-sec at 300 and 77 K, respectively.

tions in more detail in chapter 5, but it is worthwhile to consider one example here. In fig. 2.10, we show the rocking curves for two modulation-doped field-effect transistors (MODFETs). The structures consist of several layers of both InGaAs and InAlAs (see chapter 4 for details). All the layers are nominally lattice-matched except for 500 Å layers of $In_{0.68}Ga_{0.32}As$ which serve as the channel of the device. We measured the electron mobility of both structures at 300 K and 77 K. For sample 4084, we obtained: μ_{300K} = 9200 cm^2/V-sec and μ_{77K} = 40,000 cm^2/V-sec. These mobilities are reasonable for this structure.[69,70] The FWHM of the channel peak is close to the theoretical value, and fringes are present. In contrast, sample 4102 has low mobility with μ_{300K} = 1900 cm^2/V-sec and μ_{77K} = 2500 cm^2/V-sec, and a poor rocking curve. We are not certain what went wrong in the growth of 4102. Possibilities include incorrect growth temperature and contamination in the MBE. The correlation between electrical and structural characteristics suggests that, in some cases, x-ray data can be used to decide whether to process a device heterostructure.

The growth of poor quality epilayers due to incorrect growth temperature or other

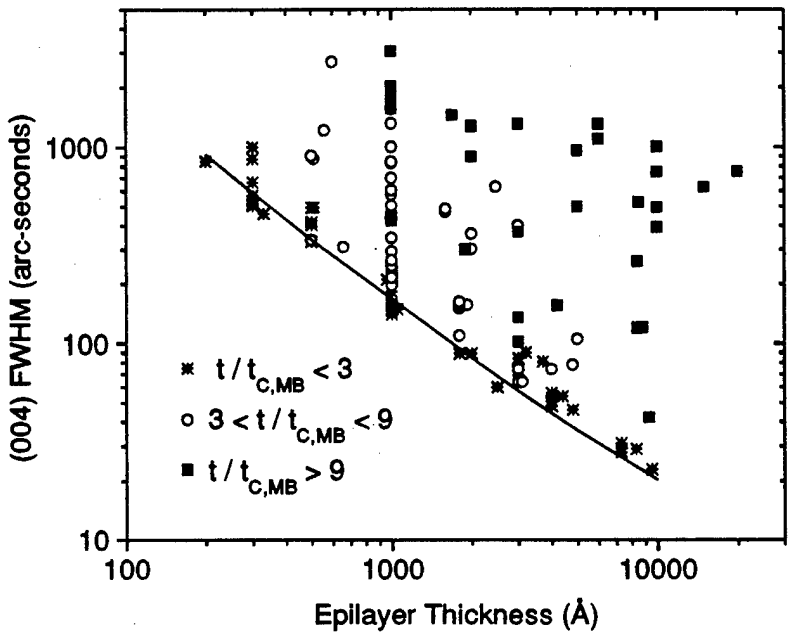

Figure 2-11: HRXRD (004) peak width versus InGaAs or InAlAs thickness for layers in compression and tension. Samples are coded based upon the ratio of layer thickness to anisotropic Matthews-Blakeslee critical thickness. Solid line is from simulations using dynamical diffraction theory (see eq. 2.13).[63]

unknown reasons was relatively rare, occurring less than 10% of the time. We eliminated such samples from our data set. In fig. 2.11, we show the (004) HRXRD epitaxial peak width as a function of thickness for the remainder of our sample set which includes InGaAs and InAlAs samples in both compression and tension. The samples are coded based upon the ratio of the layer thickness to $t_{c,MB}$. The theoretical values of FWHM for perfect layers (represented by the line) are a lower limit to our results, with experimental FWHM's approximately equal to the theoretical values for layers ranging from 200 Å to 10,000 Å. We observe that it is not necessary for the layer to be thinner than $t_{c,MB}$ in order to achieve a FWHM ratio close to one.

This result is more clearly illustrated by fig. 2.12 in which we plot the FWHM ratio versus the ratio of thickness and $t_{c,MB}$ for InGaAs (a) and InAlAs (b). For $t/t_{c,MB} < 3$ the FWHM ratio is always between 0.9 and 1.8, independent of $t/t_{c,MB}$. We observe a transition region for $3 < t/t_{c,MB} < 9$, with the FWHM ratio varying from 1.0 to 10. For $t/t_{c,MB} > 9$, the ratio ranges from 2 to 60. In fig. 2.12 the samples are coded for layers in tension or compression. For InGaAs, there is no clear

difference between the two. For InAlAs, we observe the same trend illustrated in figs. 2.7 and 2.8: higher crystalline quality for layers in tension than in compression (at constant $t/t_{c,MB}$).

Our results for InAlAs are in contrast to a recent report by Tournié *et al.*[71] They investigated nearly lattice-matched 1.3 μm layers of InAlAs on InP. For substrate temperatures of 480-520°C, the (004) HRXRD FWHM's were 240-440 arc-sec, compared to a theoretical value of only 18 arc-sec. They achieved FWHM's of less than 50 arc-sec only when a high substrate temperature (600°C) or a superlattice buffer was used. As shown in fig. 2.12b, however, when the mismatch is not too large we consistently obtain FWHM's close to the theoretical value for InAlAs grown directly on InP at 460-510°C. A possible explanation for this discrepancy is errors in the measurement of growth temperature.

In fig. 2.13, we compare the relaxation and crystalline quality criteria by plotting thickness versus lattice mismatch for InGaAs (a) and InAlAs (b). We separate the samples into three distinct groups. For $t/t_{c,MB} < 3$, the FWHM ratio appears to be randomly scattered between 0.9 and 1.8 (see fig. 2.12). Hence, we choose 1.8 as a cut-off point and consider layers with a smaller FWHM ratio to be of high crystalline quality. For all samples with $\bar{R} > 10\%$, the FWHM ratio was greater than 1.8. For all samples with a FWHM ratio less than 1.8, the layer relaxation was less than 10%. The remaining samples fall into a third intermediate group with $\bar{R} < 10\%$ and the FWHM ratio greater than 1.8.

In fig. 2.13, we include curves **R** separating layers based upon relaxation, with a cut-off at $\bar{R} = 10\%$. (We use $\bar{R}$ to refer to an average relaxation, as discussed in section 2.3.) The minimum detectable relaxation depends upon layer thickness (which influences the width and intensity of the peak), experimental background noise, and lattice mismatch. For most samples, the smallest relaxation we can measure is 5-10%. Our empirical curves **R**, obtained with this $\bar{R} = 10\%$ criterion, are actually similar to the calculated People-Bean critical layer thickness[72] and estimates from HRXRD.[7,65]

We also include curves **C** in fig. 2.13. They separate the samples based upon crystalline quality as determined by the FWHM ratio with a cut-off of 1.8. A com-

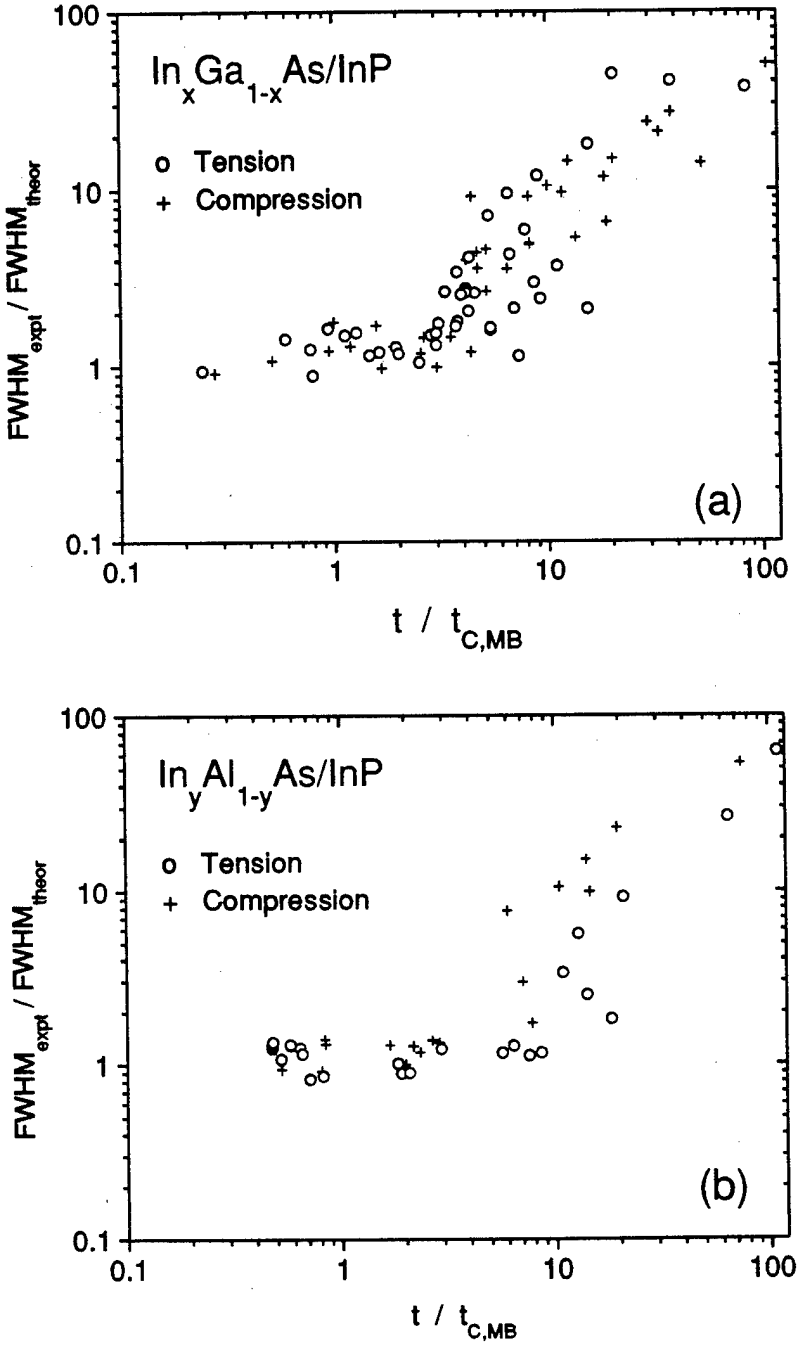

Figure 2-12: Ratio of experimental to theoretical HRXRD (004) peak width versus ratio of thickness to anisotropic Matthews-Blakeslee critical thickness for (a) InGaAs and (b) InAlAs layers. Samples are coded for compression and tension.

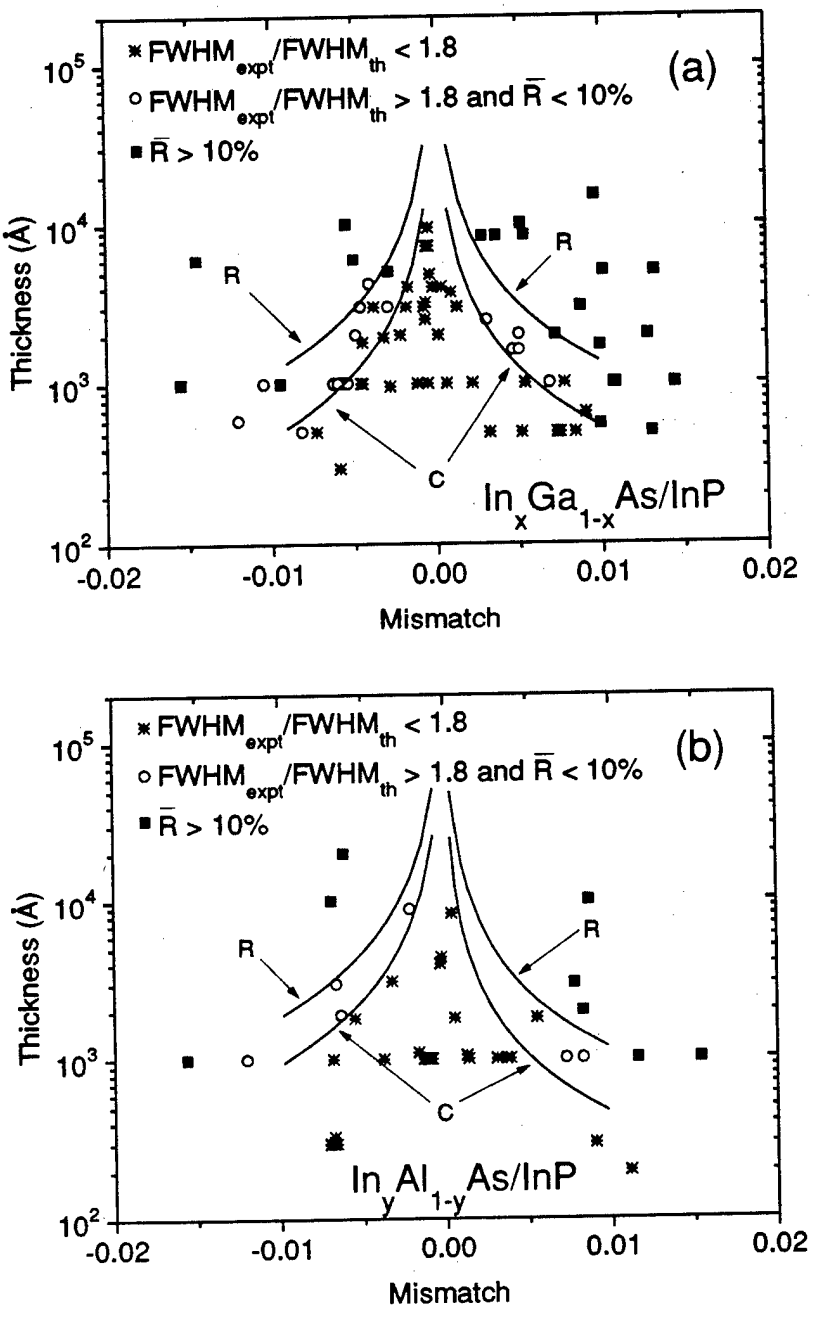

Figure 2-13: Thickness versus relaxed lattice mismatch for a) InGaAs and b) InAlAs in both compression and tension on InP. Samples are coded by the HRXRD peak-width ratio and lattice relaxation. Curves **C** and **R** are empirical, showing the degradation of crystalline quality and significant lattice relaxation, respectively.

parison of **C** and **R** confirms that the FWHM ratio is more sensitive to crystalline imperfection than direct measurements of lattice relaxation. From a practical point of view, we also note that measurement of the FWHM ratio is much faster, requiring only a single (004) scan rather than a complete set of asymmetric scans (see section 2.3).

The FWHM of an epitaxial layer can be broadened by a variety of factors. One, as mentioned earlier, is the finite thickness effect. We removed this effect by examining the FWHM ratio. Another potential broadening factor is the warpage of lattice planes resulting from strain.[73] To test for warpage effects, we performed a series of scans with varying aperture size on the x-ray collimator. We used a sample with a FWHM ratio of 2.4. The results showed that the epitaxial peak width was independent of the x-ray spot size. From this, we conclude that lattice warpage does not have a significant effect on the epitaxial peak width for our samples. Improper instrument alignment can also broaden x-ray peaks. We have achieved InP substrate peaks as narrow as 9 arc-sec, the theoretical minimum,[63] implying proper alignment.

Having eliminated the above sources of peak broadening, we conclude that the peak broadening observed for samples with FWHM ratios greater than 1.8 is primarily the result of crystalline imperfection. Traditionally, such broadening in strained layers has been attributed to misfit dislocations. Recent work has suggested the possibility of 3D growth without misfit dislocations.[33,34] Such growth could lead to imperfections (*e.g.* stacking faults) which might also broaden an HRXRD peak and eliminate Pendellosung fringes. Hence, we may be observing the effects of misfit dislocations, 3D growth, or both. We will return to this topic in chapter 6.

We have shown that the epilayer FWHM ratio and Pendellosung fringes can be a sensitive, non-destructive means to assess crystalline quality of mismatched epilayers. Our results do not necessarily imply the total absence of misfit dislocations for samples with Pendellosung fringes and FWHM ratios near unity. Although we cannot rule out the possibility of dislocations in layers with, for example, $t/t_{c,MB} = 3$, such layers do exhibit high crystalline quality and may be useful for many device applications. Knowledge of the degree of strain (relaxation) is also important for both active and

buffer layers in device heterostructures. Our results show that layers remain fully strained well beyond $t_{c,MB}$.

According to some reports, growth temperature may play an important role in the relaxation of mismatched epitaxial layers.[19,4] The temperature range over which we could obtain high-quality InGaAs and InAlAs was only about 50°C. In addition, the uncertainty in our temperature measurements was about 30°C. Hence, we were not able to make a systematic study of growth temperature effects for our MBE layers. We did, however, examine InAlAs/InP samples grown by MOCVD.† These showed FWHM ratios close to 1.0 and Pendellosung fringes for 1000 Å layers of $In_yAl_{1-y}As$, y=0.41 and 0.42, with $t/t_{c,MB} = 7$. The InAlAs was grown at 625°C, over 100°C higher than our MBE samples. This result suggests that high crystalline quality beyond $t_{c,MB}$ is not restricted to our growth conditions. We also performed post-growth annealing experiments on our MBE layers as described in chapter 4.

2.3 Lattice Relaxation and Orthorhombic Distortion

In the previous section, we showed that when mismatch is too large, the HRXRD epilayer peak broadens. For some samples, we found that this broadening was a function of azimuthal angle.[74] Fig. 2.14 illustrates the geometry of our measurements. The angle of incidence is fixed at the Bragg angle. The sample is rotated, and measurements are taken at different azimuthal angles, α. At $\alpha = 0°$, the incident x-ray beam is orthogonal to the primary flat and parallel to the [110] direction. At $\alpha = 90°$, the beam is parallel to the $[1\bar{1}0]$ direction. The array of misfit dislocations will be explained below.

In fig. 2.15, we show the (004) rocking curves at $\alpha = 0°$ and 90° for sample 1503, a 1700 Å layer of $In_{0.60}Ga_{0.40}As$. For this layer, $t/t_{c,MB} = 5.2$ and the theoretical FWHM is 99 arc-sec. The layer peak is broadened in both directions, but the FWHM

†MOCVD samples were supplied by Noren Pan of Raytheon Corporation

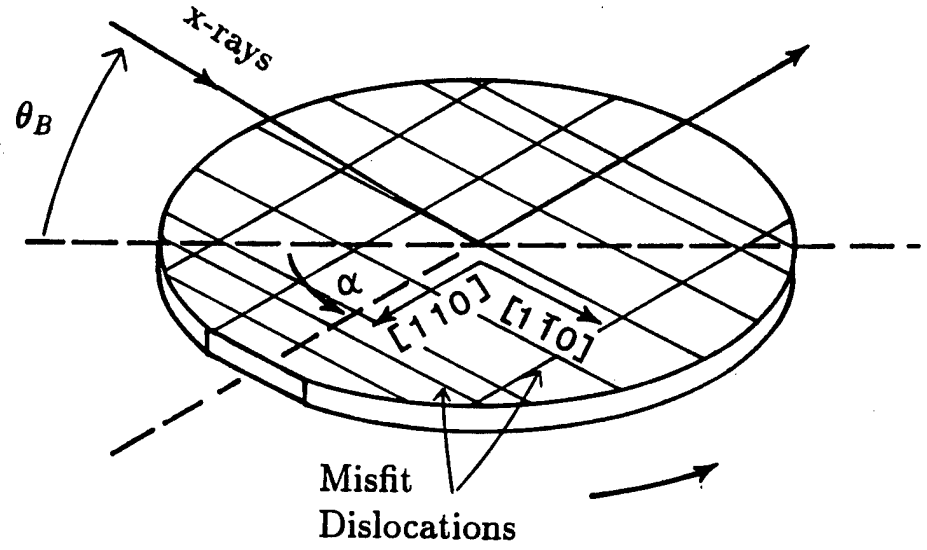

Figure 2-14: Geometry of x-ray measurements; α is the azimuthal angle (angle of rotation) of the projection of the beam on the sample with respect to the [110] direction. An asymmetric array of misfit dislocations is also shown.

is substantially larger at $\alpha = 0°$ (683 arc-sec) than at $\alpha = 90°$ (486 arc-sec). To confirm this effect, we made (004) measurements at eight different azimuthal angles for sample 1503; the results are plotted in fig. 2.16. The data approximately follow a cosine law, with FWHM minima at $\alpha = 90$ and 270°. We obtained similar results for samples of InGaAs in tension as well as InAlAs in both tension and compression.[66,74] In all cases with significant FHWM variations, the minima occurred when the incident beam was parallel to the $[1\bar{1}0]$ and $[\bar{1}10]$ directions.

In zinc-blende semiconductors such as InGaAs, the $[1\bar{1}0]$ and $[\bar{1}10]$ directions are equivalent. The [110] and $[\bar{1}\bar{1}0]$ directions are also equivalent, but $[1\bar{1}0]$ is not equivalent to [110].[75] In fact, several papers report an asymmetry in misfit dislocation density for mismatched III-V semiconductors, with a greater density in one $< 110 >$ direction than in the orthogonal direction for (001) substrates.[22,76–79] Misfit dislocations cause a local tilting of lattice planes. These tilted planes will satisfy the Bragg condition at angles that differ slightly from the Bragg angle for a dislocation-free layer. Based on these facts, we can now explain the data of figs. 2.15 and 2.16 as follows. If the number of dislocations along the $[1\bar{1}0]$ direction exceeds the number

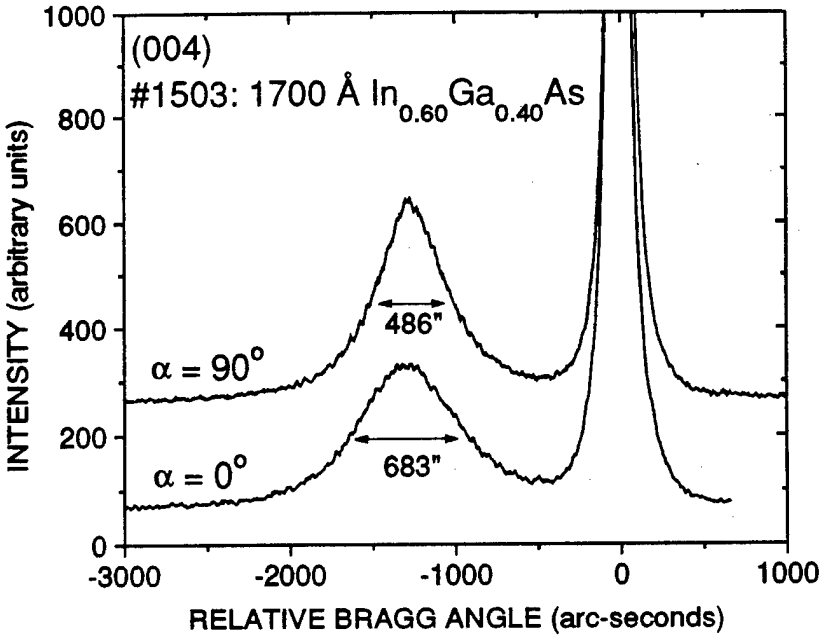

Figure 2-15: HRXRD (004) rocking curves for sample 1503, showing different epilayer peak widths at $\alpha = 0$ and 90°.

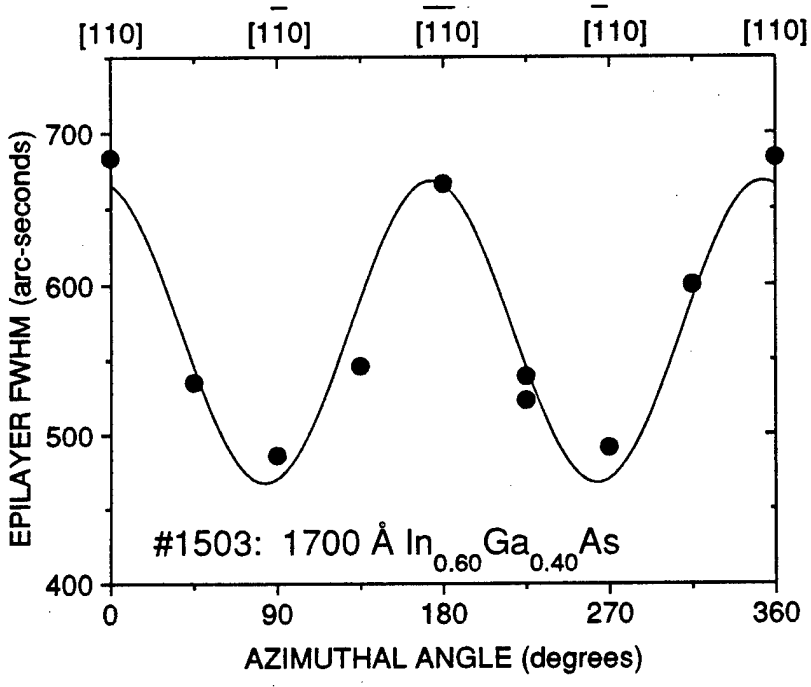

Figure 2-16: HRXRD (004) epilayer peak width as a function of azimuthal angle for sample 1503. Solid line is a least-squares fit to a cosine function.

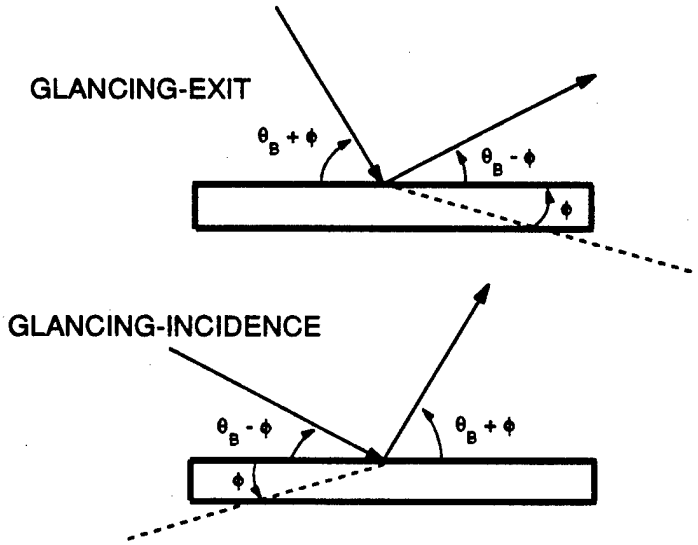

Figure 2-17: Geometry of glancing-exit and glancing-incidence asymmetric HRXRD measurements. θ_B is the Bragg angle and ϕ is the angle between the surface normal and the diffracting planes.

along [110] (as schematically illustrated in fig. 2.14), the peak width observed along [110] ($\alpha = 0°$) should be greater than that observed along [1$\bar{1}$0] ($\alpha = 90°$), as our experiments indicate. Such an anisotropic dislocation density distribution was observed with HRXRD by Grundmann *et al.* for InGaAs/GaAs heterostructures under compression.[80] Our work shows that similar behavior occurs for InGaAs/InP and InAlAs/InP under compression or tension.

Since misfit dislocations relieve epilayer strain, an asymmetry in misfit dislocation density should result in different parallel lattice mismatches in the orthogonal [110] and [1$\bar{1}$0] directions. We can measure the parallel mismatches with HRXRD by using asymmetric reflections. In an asymmetric reflection, the diffracting plane is not parallel to the surface. Hence, to obtain a Bragg reflection, the angle of incidence must be equal to $\theta_B \pm \phi$ where ϕ is the angle between the surface and the diffracting plane.[59] The detector is at $2\theta_B$, as in the case of symmetric reflections. The two asymmetric cases are illustrated in fig. 2.17 and referred to as glancing-incidence and glancing-exit reflections.

For asymmetric reflections, the measured peak separation between the substrate and layer peaks is no longer simply the difference in Bragg angles. Instead, it is given by:

$$\Delta\theta = \Delta\theta_B \pm \Delta\phi \tag{2.14}$$

where $\Delta\phi$ is the tilt of the substrate with respect to the epilayer.[81] In the case of tetragonal distortion, equivalent *asymmetric* planes of the substrate and layer are not parallel. Hence, $\Delta\phi$ is non-zero and contributes to the Bragg peak separation. The + and - signs refer to glancing-incidence and glancing-exit reflections, respectively.

The terms in (2.14) can be written in terms of lattice constant differences:[81]

$$\Delta\theta_B = -\left[\left(\frac{\Delta a}{a}\right)_\perp \cos^2\phi + \left(\frac{\Delta a}{a}\right)_{||} \sin^2\phi\right] \tan\theta_B \tag{2.15}$$

$$\Delta\phi = \left[\left(\frac{\Delta a}{a}\right)_\perp - \left(\frac{\Delta a}{a}\right)_{||}\right] \sin\phi\cos\phi \tag{2.16}$$

In the case of symmetric reflections such as the (004) reflection from (001) substrates, $\phi = 0°$ and (2.14)-(2.16) reduce to (2.4). Hence, the perpendicular mismatch can be calculated directly from an (004) rocking curve, as we did in section 2.1. For the general case, we combine (2.14), (2.15), and (2.16):

$$\Delta\theta = \left(\frac{\Delta a}{a}\right)_{||} (-\sin^2\phi\tan\theta_B \pm \sin\phi\cos\phi) + \left(\frac{\Delta a}{a}\right)_\perp (-\cos^2\phi\tan\theta_B \mp \sin\phi\cos\phi) \tag{2.17}$$

where the upper signs are for glancing-exit and the lower signs are for glancing-incidence reflections.

We made measurements of both (115) and (224) asymmetric reflections. Since the substrates are (001), it is straightforward to calculate: $\phi_{115} = 15.79°$ and $\phi_{224} = 35.26°$. Using (2.3) to calculate the Bragg angles, (2.17) reduces to the following four equations (for InP substrates only).

(115) glancing-incidence:

$$\Delta\theta = -1.125\left(\frac{\Delta a}{a}\right)_{\perp} + 0.193\left(\frac{\Delta a}{a}\right)_{\parallel} \tag{2.18}$$

(115) glancing-exit:

$$\Delta\theta = -0.601\left(\frac{\Delta a}{a}\right)_{\perp} - 0.331\left(\frac{\Delta a}{a}\right)_{\parallel} \tag{2.19}$$

(224) glancing-incidence:

$$\Delta\theta = -1.031\left(\frac{\Delta a}{a}\right)_{\perp} + 0.191\left(\frac{\Delta a}{a}\right)_{\parallel} \tag{2.20}$$

(224) glancing-exit:

$$\Delta\theta = -0.089\left(\frac{\Delta a}{a}\right)_{\perp} - 0.751\left(\frac{\Delta a}{a}\right)_{\parallel} \tag{2.21}$$

In the case of simple tetragonal distortion, two measurements are required to obtain both $(\Delta a/a)_{\perp}$ and $(\Delta a/a)_{\parallel}$. For example, we could measure the (115) glancing-exit and glancing-incidence reflections. If instead $(\Delta a/a)_{\perp}$ is known from an (004) measurement, then only one asymmetric measurement is required to determine $(\Delta a/a)_{\parallel}$. In this case, it is preferable to measure one of the glancing-exit reflections because $\Delta\theta$ will be more heavily weighted by the parallel mismatch according to (2.18)-(2.21).

In fig. 2.18 we show (224) rocking curves for sample 1245, 8500 $\AA$ of InGaAs under compression. Both the $CuK_{\alpha 1}$ and $CuK_{\alpha 2}$ components are visible for the InP peak. The peak separation, $\Delta\theta$, is different for the curves measured at $\alpha = 0$ and 90^{o}. Instead of a single $(\Delta a/a)_{\parallel}$, we have different values in the two orthogonal directions on an (001) substrate, $(\Delta a/a)_{\parallel[110]}$ and $(\Delta a/a)_{\parallel[1\bar{1}0]}$.

To calculate the parallel mismatches, we average scans separated by 180^{o} [$(\Delta a/a)_{\parallel[110]}$ is calculated from the average of $\Delta\theta_{(224)}$ ($\alpha = 0^{o}$) and $\Delta\theta_{(224)}$ ($\alpha = 180^{o}$); $(\Delta a/a)_{\parallel[1\bar{1}0]}$ is calculated from the average of $\Delta\theta_{(224)}$ ($\alpha = 90^{o}$) and $\Delta\theta_{(224)}$ ($\alpha = 270^{o}$)] to eliminate differences in $\Delta\theta$ caused by possible epilayer tilt. We also note that the epilayer peak is sharper for $\alpha = 90^{o}$ than for 0^{o}, presumably due to the same reason as the (004) peak width variation: an asymmetry in dislocation density.

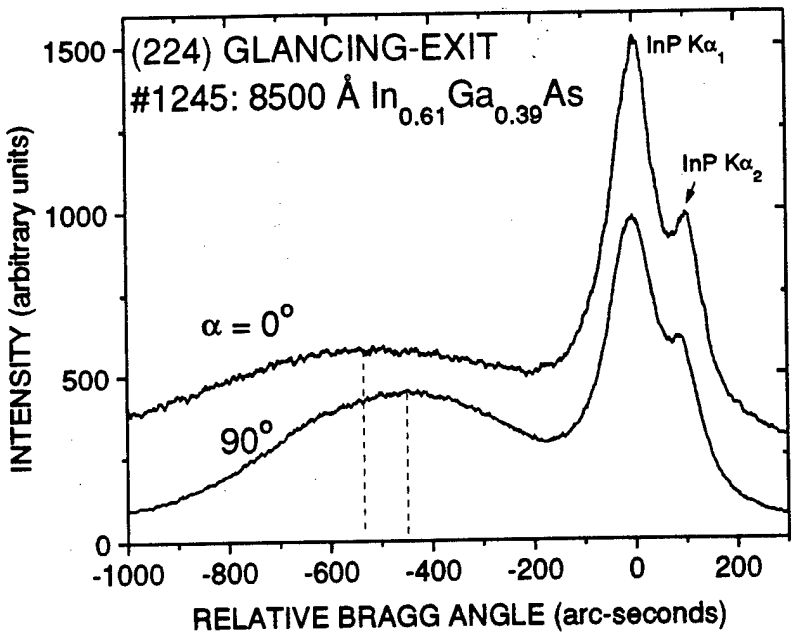

Figure 2-18: HRXRD rocking curves for (224) glancing-exit reflections of sample 1245 at azimuthal angles of 0° and 90°. The difference in peak separation for the two curves indicates asymmetric strain in the epilayer.

An epilayer lattice is now described by three mismatches: $(\Delta a/a)_{\perp}$, $(\Delta a/a)_{|||[110]}$, and $(\Delta a/a)_{|||[1\bar{1}0]}$. The conventional expression for the relaxed lattice mismatch, (2.6), must be modified. The new expression is:

$$\left(\frac{\Delta a}{a}\right)_r = \frac{1-\nu}{1+\nu}\left(\frac{\Delta a}{a}\right)_{\perp} + \frac{\nu}{1+\nu}\left[\left(\frac{\Delta a}{a}\right)_{|||[110]} + \left(\frac{\Delta a}{a}\right)_{|||[1\bar{1}0]}\right] \qquad (2.22)$$

where ν is Poisson's ratio. If $(\Delta a/a)_{\perp} \neq (\Delta a/a)_{|||[110]} \neq (\Delta a/a)_{|||[1\bar{1}0]}$, the distortion of the lattice is orthorhombic. For example, the data for sample 1245 of fig. 2.18 indicates that $(\Delta a/a)_{\perp} = 8.33 \times 10^{-3}$, $(\Delta a/a)_{|||[110]} = 2.94 \times 10^{-3}$, and $(\Delta a/a)_{|||[1\bar{1}0]} = 1.88 \times 10^{-3}$. Using $\nu = 1/3$, we find $(\Delta a/a)_r = 5.37 \times 10^{-3}$. From (2.8), the composition is $In_{0.610}Ga_{0.390}As$.

Whereas the degree of relaxation is defined by a single parameter in the case of purely tetragonal distortion, two parameters are needed to characterize orthorhombic distortion. One can define:

$$R_{[110]} = \frac{\left(\frac{\Delta a}{a}\right)_{\|[110]}}{\left(\frac{\Delta a}{a}\right)_{r}} \tag{2.23}$$

and

$$R_{[1\bar{1}0]} = \frac{\left(\frac{\Delta a}{a}\right)_{\|[1\bar{1}0]}}{\left(\frac{\Delta a}{a}\right)_{r}} \tag{2.24}$$

We also define the average relaxation, $\bar{R}$:

$$\bar{R} = \frac{R_{[110]} + R_{[1\bar{1}0]}}{2} \tag{2.25}$$

For symmetric relaxation, $R_{[110]} = R_{[1\bar{1}0]}$, eq. (2.25) reduces to (2.12), the conventional definition of relaxation. For sample 1245 we find: $R_{[110]} = 55\%$, $R_{[1\bar{1}0]} = 35\%$, and $\bar{R}$ $= 45\%$.

For most samples, we determined $\bar{R}$ from an (004) and four (115) or (224) HRXRD measurements, as discussed above. $\bar{R}$ can also be calculated from only the symmetric (004) rocking curve if the composition is known. The composition is estimated from other samples grown the same day and the measured activation energy of the Al or Ga cell. (The In cell temperature is held constant in our work.) We use this method for some thin epilayers ($t \leq 1000\mathring{A}$) because of the weak and broad asymmetric layer peaks in HRXRD. We show each partially relaxed layer on a plot of thickness versus mismatch for a) InGaAs and b) InAlAs in figure 2.19. The value of $\bar{R}$ is given for each sample. The uncertainties in $\bar{R}$ are 5-10%. We do not include samples with $\bar{R} < 5\%$.

In general, we observe the expected trends in fig. 2.19. At a constant mismatch, $\bar{R}$ generally increases with increasing thickness. For a fixed thickness, $\bar{R}$ usually increases with increasing mismatch (positive or negative). We note that one of the InAlAs layers is 114% relaxed. In this case, $(\Delta a/a)_{\|_{[110]}}$ and $(\Delta a/a)_{\|_{[1\bar{1}0]}}$ are slightly larger than $(\Delta a/a)_{\perp}$. A similar "overrelaxed" InGaAs layer was reported by Chu *et al.*[82] Apparently, more dislocations are introduced during growth than are required to fully relax the strain.

In section 2.2, we showed that the crystalline quality of epilayers begins to degrade

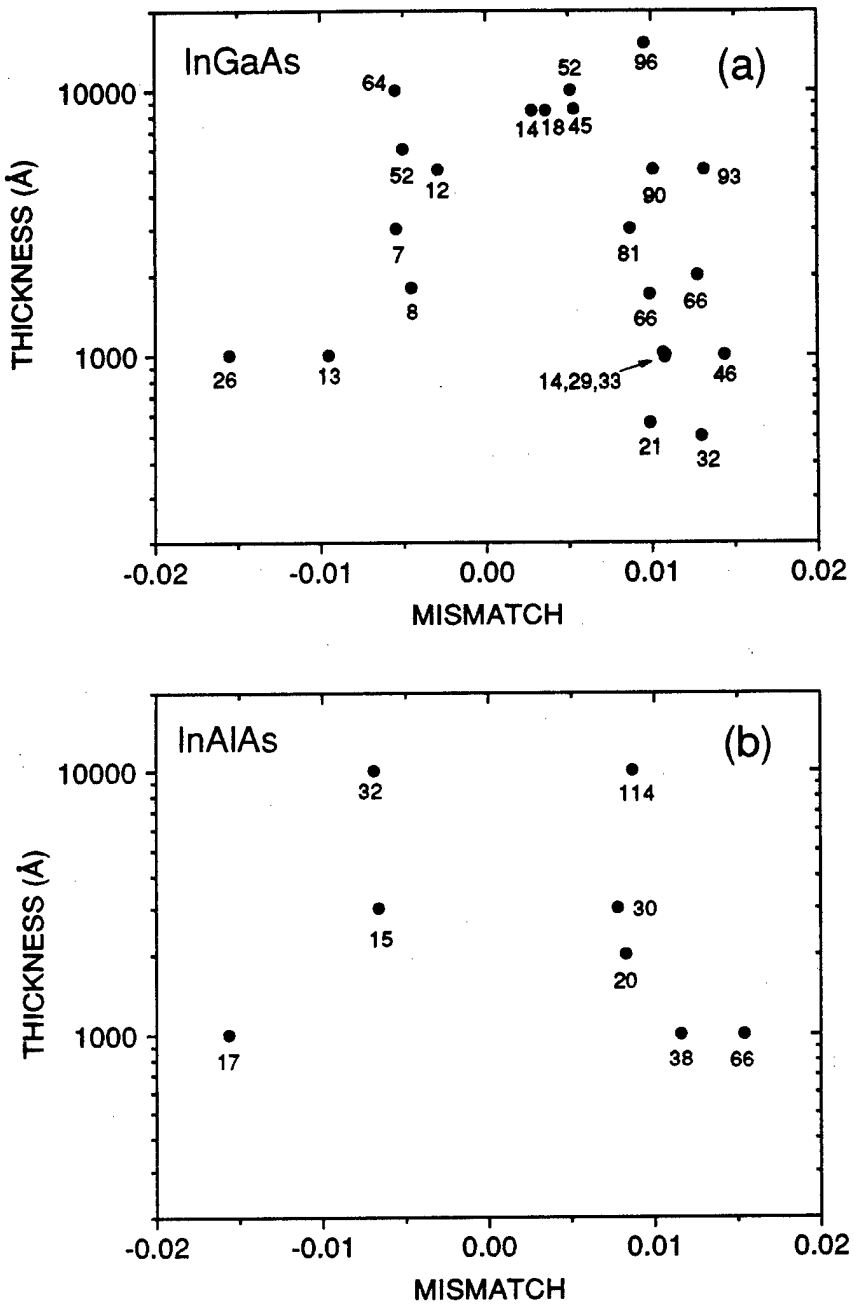

Figure 2-19: Thickness versus lattice mismatch for a) InGaAs and b) InAlAs. The average lattice relaxation, $\bar{R}$, is given for each sample. Samples with $\bar{R} < 5\%$ are not shown.

before significant lattice relaxation. Hence, all the partially relaxed samples in fig. 2.19 have a high density of structural defects, making them unsuitable as active layers in most device applications. There are some structures, however, in which the active regions of a device are grown on top of a fully relaxed buffer layer.[83,84] Only three of our samples are more than 90% relaxed. In each case, the layer is over 50 times thicker than $t_{c,MB}$. Hence, very thick layers are generally required for complete strain relaxation.

We have observed orthorhombic distortion in all of our heterostructures with $\tilde{R} >$ 10%. In fig. 2.20, we plot the difference in $R_{[110]}$ and $R_{[1\bar{1}0]}$ versus $t/t_{c,MB}$ for all samples on which a complete set of asymmetric x-ray scans were collected. The samples are coded by material and strain. For the two samples with $t/t_{c,MB} < 15$, the difference in relaxation is zero within the experimental error bars. The average relaxation is also negligible for these two samples. For all the other samples, ($R_{[110]}$-$R_{[1\bar{1}0]}$) > 0. We conclude that these partially relaxed layers are orthorhombically distorted, with maximum strain relief in the [110] direction, implying a greater density of misfit dislocations running parallel to the [$1\bar{1}0$] direction[‡] for layers of both InGaAs and InAlAs, in either tension or compression.

The magnitude of the relaxation asymmetry cannot be predicted from $t/t_{c,MB}$. For example, at $t/t_{c,MB} \cong 20$, the values of ($R_{[110]}$-$R_{[1\bar{1}0]}$) are 5, 9, 19, 31, and 37%. The extreme values of 5 and 37% were both measured for samples of InGaAs in compression. Since the relaxation asymmetry is often substantial and apparently cannot be predicted, a complete set of asymmetric x-ray scans must be measured to determine the composition of a partially relaxed epilayer.

We note that for many partially relaxed layers on which asymmetric rocking curves revealed orthorhombic distortion, the (004) FWHM did not vary as a function of azimuthal angle. We speculate that once the dislocation density reaches a certain value in both directions, the FWHM saturates and its angular dependence disappears. Hence, the absence of FWHM variations with α does not imply the absence

[‡]For the Sumitomo wafers used in this study, the majority of dislocations are parallel to the major flat and orthogonal to the oval defects.

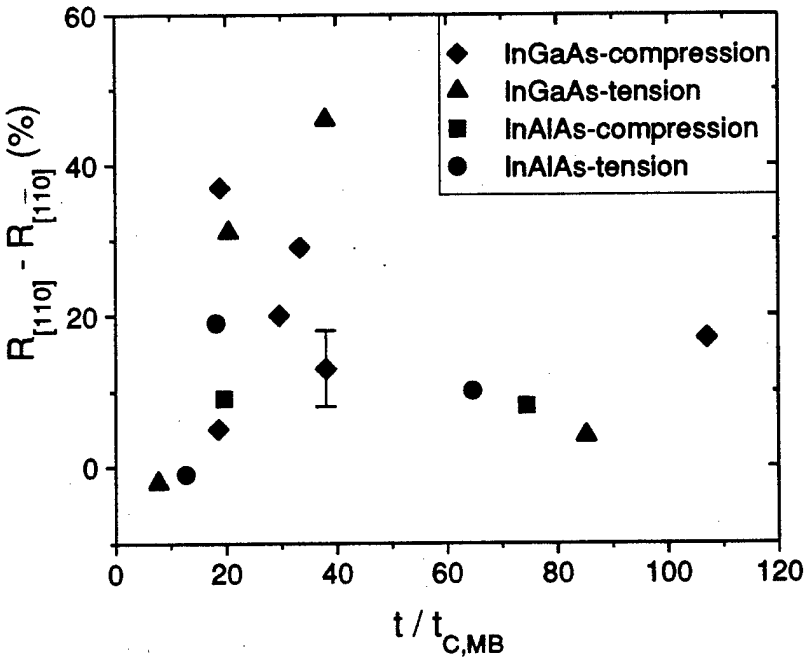

Figure 2-20: Difference in relaxation in the [110] and [1$\bar{1}$0] directions as a function of the ratio of thickness to Matthews-Blakeslee critical layer thickness. Most of the samples exhibit substantial orthorhombic distortion. The error bar shown is typical of the estimated error for all samples.

of orthorhombic distortion.

In fig. 2.21 we show a schematic view of lattice distortion suggested by our data. We assume the epilayer has a larger lattice constant than the substrate. For layers less than a critical thickness (t < t_c), tetragonal distortion results (fig. 2.21a). For t > t_c, misfit dislocations form in an asymmetric pattern, partially relaxing the strain and resulting in orthorhombic distortion (b,c). For t >> t_c, the strain is fully relieved by dislocations and the epilayer symmetry becomes cubic (d).

Although there are many reports showing an asymmetry in misfit dislocation density on (001) zinc-blende substrates, there is some confusion in the literature regarding which direction ([110] or [1$\bar{1}$0]) has the maximum density.[22,79,85] Using two different techniques, we have shown that the majority of dislocations are parallel to the [1$\bar{1}$0] direction for both InGaAs and InAlAs in compression or tension. In chapter 6, we will discuss the reason for the asymmetry in dislocation density. We will also show that relaxation may be more complex, with features such as elongated islands contributing to asymmetry.

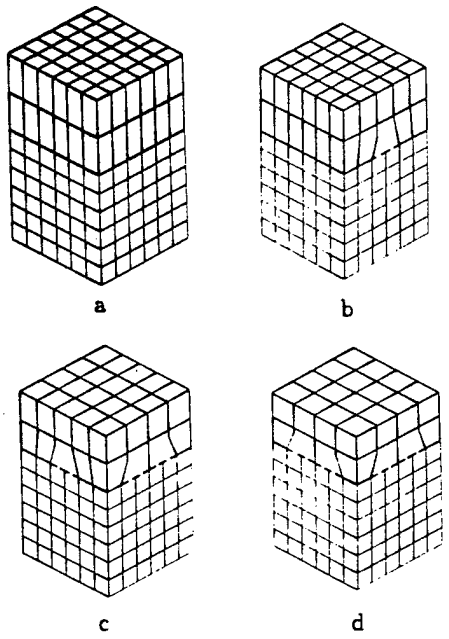

Figure 2-21: Schematic view of lattice distortion as a function of degree of relaxation for an epilayer with a larger lattice constant than the substrate: a) t < t_c, b) and c) t > t_c, d) t >> t_c.

2.4 Optimal Thickness for Composition Measurements

As a result of the orthorhombic distortion described in the previous section, at least five HRXRD scans are required to determine $(\Delta a/a)_r$ for partially relaxed InGaAs and InAlAs on InP. Since a single scan typically takes an hour or more, measuring the composition of a partially relaxed layer is very time-consuming. In addition, some commercial HRXRD systems are only designed to measure (004) symmetric reflections. Hence, when calibrating composition, the growth of relaxed epitaxial layers should be avoided to eliminate the need for asymmetric measurements.

Strain relaxation is illustrated by the four (004) rocking curves shown in fig. 2.4. As discussed in section 2.2, misfit dislocations formed in sample 1804, relaxing strain and hence reducing the tetragonal distortion and $\Delta\theta$. Hence, the (004) peak separation and the assumption of coherency would give the correct composition for samples 1808, 1806, and 1805, but an incorrect value for sample 1804. For this sample set, it is clear that significant relaxation does not occur until $t/t_{c,MB} > 18$.

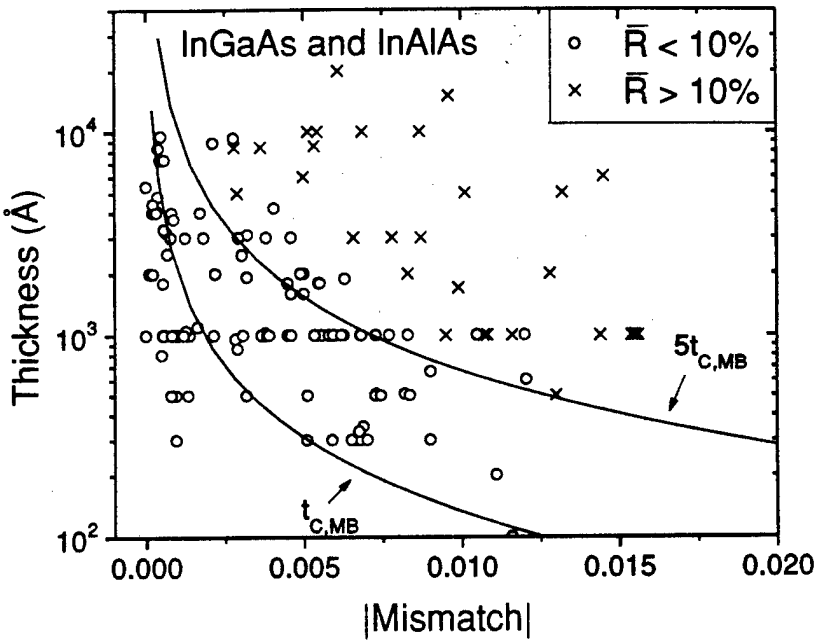

Figure 2-22: Thickness versus lattice mismatch for 150 samples of InGaAs and InAlAs on InP. Samples are coded by lattice relaxation. Both composition and relaxation were measured by HRXRD. Note that the lattice relaxation is always less than 10% for layers less than five times the Matthews-Blakeslee critical thickness.

We can confirm the findings from fig. 2.4 by examining our entire sample set, including both InGaAs and InAlAs in compression and tension. We plot the thickness of each sample as a function of mismatch in fig. 2.22. The samples are coded by average lattice relaxation, $\bar{R}$. We conclude that for these materials, a layer can exceed $t_{c,MB}$ by at least a factor of five with relaxation of less than 10%.

The possibility of layer relaxation puts an upper limit on the thickness of calibration layers. If layers are too thin, however, they cannot be detected by HRXRD. We illustrate this in fig. 2.23 which includes simulated rocking curves for single layers of $In_{0.60}Ga_{0.40}As$ on InP. The layer thicknesses are 100, 200, 500, and 1000 Å. Epilayer peaks are visible for the 200-1000 Å layers. As a result of the tail of the InP substrate peak, however, no peak is visible for the 100 $\AA$ layer. Hence, for this mismatch, the lower limit for layer thickness is between 100 and 200 Å. For smaller mismatches, thicker layers will be required because the substrate peak will be closer to the layer peak.

Based upon simulations such as fig. 2.23, we determined the minimum layer

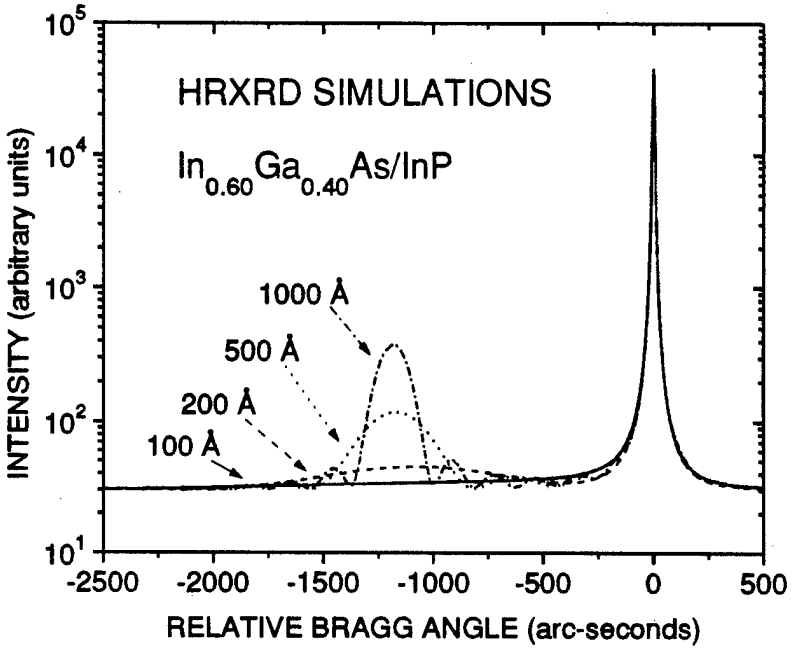

Figure 2-23: Simulated HRXRD rocking curves for $In_{0.60}Ga_{0.40}As/InP$ heterostructures with different epilayer thicknesses.[63]

thickness required to produce a resolvable peak. We plot the results for $In_xGa_{1-x}As$ layers on InP as a function of mismatch in fig. 2.24. To within 5%, the minimum thicknesses are the same for InGaAs and InAlAs in tension or compression. If the maximum thickness were limited by $t_{c,MB}$, the range of acceptable thicknesses would be quite small. Fortunately, as shown in figs. 2.4 and 2.22, layers can exceed $t_{c,MB}$ without substantial relaxation. We include our conservative upper limit of $5t_{c,MB}$ in fig. 2.24. We use $t_{c,MB}$ for InGaAs in compression, but the values are similar for the other three cases (see appendix C). The other items in fig. 2.24 will be discussed below.

The procedure used to obtain the minimum resolvable peak (MRP) simulations line in fig. 2.24 implicitly assumes "perfect" layers and a measurement system with infinite resolution (dynamic range). Although defect-free single crystals may be grown in some cases, there is always an experimental background count-rate which can make it more difficult to identify layer peaks. Hence, it is important to experimentally verify the MRP criteria. We did so by searching our sample set and selecting those layers which were reasonably close to the MRP line. We plot these samples as data points on

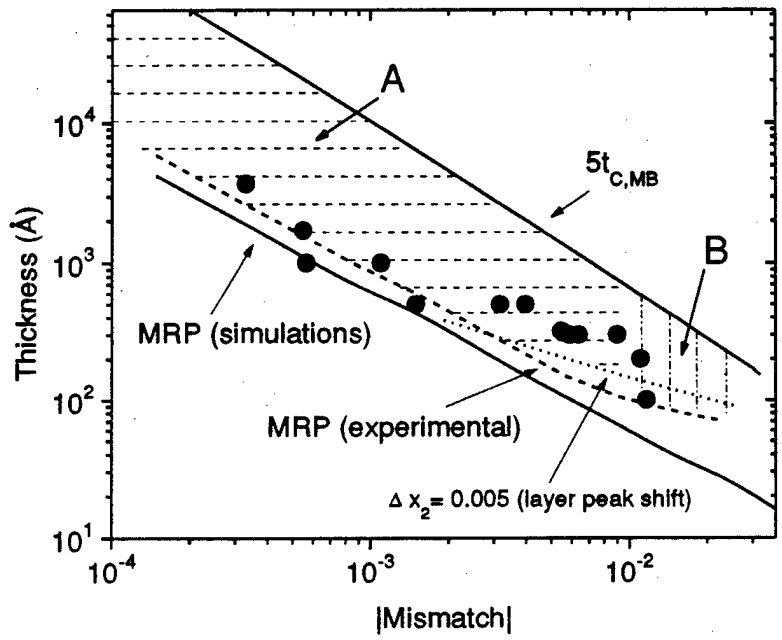

Figure 2-24: Epilayer thickness versus mismatch showing the minimum resolvable peak (MRP) criteria, the thickness at which the error in composition due to layer peak shift is 0.005, and the 10% relaxation threshold of $5t_{c,MB}$. Experimental data points are also shown. The estimated error in composition, Δx_T, is less than 0.01 for samples in region A. In region B, $\Delta x_T < 0.03$.

fig. 2.24. The rocking curve for each sample had a distinct layer peak. As an example, we consider sample 2010 in fig. 2.9. This sample was a typical single-layer calibration growth. We observe distinct peaks from both the substrate and the epilayer as well as interference fringes. The peak separation, $\Delta\theta$, is +84 arc-sec. Using (2.4), (2.6), and (2.9), we obtain a composition of $In_{0.516}Al_{0.484}As$. From simulations, the minimum thickness is 2000 Å for a resolvable peak at this mismatch. The experimental fringe spacing gives a thickness of 3700 Å for sample 2010. Considering the clear peak separation in fig. 2.9, we believe that layers of the same composition would produce resolvable peaks for thicknesses less than 3700 Å. Based upon our data points, we include a dashed MRP-expt line in fig. 2.24. Epilayer peaks should by resolvable by HRXRD for points above this line.

Our experimental results and simulations suggest that the composition of layers lying above the MRP-expt line and below the $5t_{c,MB}$ line can be measured by a single HRXRD scan. We now discuss six sources of error and the resulting accuracy for such measurements.

1. **Lattice constants and Poisson ratios:** Estimates of composition from HRXRD measurements require knowledge of lattice parameters of the substrate (InP) and end-members of the ternary alloy (InAs, GaAs, AlAs), as well as Poisson's ratio for the alloy. Until recently, the values of a_{AlAs} and ν_{AlAs} were not known to high precision. Two independent studies in 1991 established definitive values for these parameters.[60] For all four materials, the lattice constants are now known to within 0.001 Å, and the Poisson ratios to within 0.005.[86–89] We estimate that the resulting error in layer composition, Δx_1, is less than 0.003.

2. **Epilayer peak shift:** Another potential source of error results from the shift of epilayer peak position as a result of the tail of the substrate peak.[90] This effect is illustrated in fig. 2.23. Note that the separation between the InP and InGaAs peaks, $\Delta\theta$, increases with increasing InGaAs thickness. If the composition is obtained directly from $\Delta\theta$ via Bragg's law, the results for the 1000 Å, 500 Å, and 200 Å layers are x = 0.5995, 0.5988, and 0.5932, respectively. Using simulations, we calculated the thickness, as a function of mismatch, at which the error in composition, Δx_2, is

equal to 0.005. For mismatches less than 0.002, the resulting thicknesses were nearly identical to the MRP criterion. For larger mismatches, however, the values are greater than the MRP criterion, as shown by the dotted line in fig. 2.24. By comparison to simulations, one can always compensate for the epilayer peak shift; fig. 2.24 can be used to determine when such simulations are necessary.

3. **Relaxation:** We consider a worst-case scenario in which a layer with $\bar{R} = 10\%$ is assumed to be coherent. Using (2.6), (2.7), and Vegard's law, we obtain Δx_3, the error in composition:

$$\Delta x_3 = \frac{a_{InP}}{20(a_{InAs} - a_{GaAs(AlAs)})} \left(\frac{\Delta a}{a}\right)_r = k \left(\frac{\Delta a}{a}\right)_r \tag{2.26}$$

where k=0.72 for $In_xGa_{1-x}As/InP$ and 0.74 for $In_yAl_{1-y}As/InP$. For example, a layer of $In_{0.600}Ga_{0.400}As$ on InP has $(\Delta a/a)_r = 0.0047$ and $\Delta x_3 = 0.003$; the apparent composition is $In_{0.597}Ga_{0.403}As$, a tolerable error in most applications.

4. **Experimental errors in $\Delta\theta$** will translate into errors in the composition. Such errors are a function of several factors including layer thickness (peak width), mismatch, background countrate, count time per point, and the angular step size between points. We estimated the error, $\Delta\theta^E$, for the samples shown in fig. 2.24. For all the samples with mismatch less than 10^{-2}, $\Delta\theta^E < 90$ arc-sec, which translates to $\Delta x_4 < 0.005$. Errors are generally much smaller for layers thicker than 500 Å. For the 100 and 200 Å layers (mismatch of 0.011), $\Delta\theta^E < 180$ arc-sec, and $\Delta x_4 < 0.010$. We also note that poor crystalline quality can broaden epilayer peaks, possibly increasing $\Delta\theta^E$. By remaining below $t/t_{c,MB} = 5$, we will generally avoid substantial broadening due to lattice mismatch. Other factors such as improper growth temperature can also degrade layer quality and broaden x-ray peaks.

5. **Differential Form of Bragg's Law:** An additional error can result from using (2.4) when $\Delta\theta$ is not "small." The exact expression is:[59]

$$\left(\frac{\Delta a}{a}\right)_\perp = \frac{sin(\theta_B)}{sin(\theta_B + \Delta\theta)} - 1 \tag{2.27}$$

The error introduced by using (2.4), Δx_5, is only 0.001 when $(\Delta a/a)_r = \pm\ 0.0050$,

but increases to 0.010 for $(\Delta a/a)_r = \pm\ 0.017$. This error can be eliminated in all cases by using (2.27).

6. **Vegard's law:** The final potential source of error is deviation from Vegard's law. Based upon experimental studies of InGaAs[91-93] as well as theoretical considerations,[94] we believe that Vegard's law is a good approximation for the lattice constant of InGaAs and InAlAs. We do not, however, have sufficient information to make a good estimate of the probable error in composition measurements.

To obtain an estimate of the total error in composition, Δx_T, we use:

$$\Delta x_T = \sqrt{\Delta x_1^2 + \Delta x_2^2 + \Delta x_3^2 + \Delta x_4^2} \tag{2.28}$$

We note that for thinner samples, the $\Delta\theta$ and layer peak shift errors may be near their maxima, but the relaxation error will be negligible. For thicker samples, the opposite is generally true. Using (2.28), we find that $\Delta x_T < 0.01$ for the shaded region A in fig. 2.23. In many cases, Δx_T will be much smaller. Our data is limited for mismatches larger than 0.01, but we estimate $\Delta x_T < 0.03$ for region B.

Figure 2.24 can be used to determine the optimal thickness for calibration layers. For example, if the mismatch for a calibration layer is expected to be between 0.001 and 0.004, a thickness of 1000-2000 Å should be chosen to minimize Δx_T.

We note that the MRP criterion was developed for single layers on substrates, and hence is not strictly valid for multi-layer structures. Based upon simulated and experimental results on multi-layer structures including devices, however, we have found the MRP criterion is still approximately valid in most situations. One could construct heterostructures for which this would not be the case. For example, a 200 Å layer of $In_{0.70}Ga_{0.30}As$ would not give a distinct peak if a 2000 Å layer of $In_{0.69}Ga_{0.31}As$ were also present. Hence, fig. 2.24 may be used (with caution) to determine whether HRXRD can provide accurate measurements of layer composition in complex heterostructures including devices. In some cases, complete dynamical simulations will be necessary.

2.5 Summary

In summary, we used HRXRD to investigate the impact of lattice mismatch on epitaxial layers of InGaAs and InAlAs grown by MBE on InP. Measurement of (004) layer peak width and interference fringes is shown to be a sensitive, non-destructive technique to assess structural imperfection. We found that the crystalline quality of InGaAs and InAlAs epitaxial layers consistently remains largely unperturbed to thicknesses up to 3-9 times the Matthews-Blakeslee critical layer thickness for lattice mismatch up to $\pm$ 1%.

When layers begin to relax, misfit dislocations form in an asymmetric pattern, with the majority of dislocations parallel to the $[1\bar{1}0]$ direction for InGaAs and InAlAs in compression or tension. As a result, the crystal symmetry changes from tetragonal to orthorhombic. This orthorhombic distortion must be taken into account when measuring the composition of partially relaxed epilayers.

Based upon our measurements of both coherent and relaxed layers as well as HRXRD simulations, we have determined the range of epilayer thicknesses over which a single HRXRD scan yields the composition of $In_xGa_{1-x}As$ and $In_yAl_{1-y}As$ layers to within 1%. When possible, calibration layers should be grown within this range to allow fast and accurate characterization.

Chapter 3

Optical Anisotropy

In chapter 2, we used HRXRD to determine layer composition, relaxation, and crystalline quality. We did not, however, obtain any information on the mechanism of structural degradation. In this chapter, we use a new technique to measure the optical anisotropy (OA) of epilayers. We demonstrate that OA is related to the growth mode, with surface roughness (possibly associated with 3-D growth) causing large anisotropies. Based upon a comparison of OA values and HRXRD peak widths, we conclude that a large optical anisotropy is associated with a degradation in layer quality. Hence, measurement of OA is a potentially powerful technique for probing the limits of strained layer epitaxy.

In section 3.1, we briefly review optical properties of solids and their measurement by conventional ellipsometry. We developed a new optical characterization technique known as variable azimuthal-angle ellipsometry (VAAE). We describe the technique and our results in Section 3.2. We also measured selected samples by reflectance difference spectroscopy (RDS), a characterization tool which is extremely sensitive to optical anisotropy. Section 3.3 includes the RDS results and their correlation with VAAE. We consider the origin of the optical anisotropy in section 3.4 and summarize our findings in section 3.5.

3.1 Background

The application of an electric field, E, to a material results in an electric displacement, D. In scalar form, the relationship between these two quantities is:

$$D = (\epsilon_1 + i\epsilon_2)E \tag{3.1}$$

where $(\epsilon_1 + i\epsilon_2)$ is the dielectric constant of the material. The dielectric constant is related to the complex refractive index, N, by:

$$N^2 = (n + ik)^2 = \epsilon_1 + i\epsilon_2 \tag{3.2}$$

where n is the real refractive index and k is the extinction coefficient of the material. Another useful quantity is the absorption coefficient, α, which can be expressed as:

$$\alpha = \frac{4\pi k}{\lambda} \tag{3.3}$$

where λ is the wavelength of the light. The reciprocal of α is the penetration depth, δ; the intensity of light drops by a factor of 1/e for each δ.

Ellipsometry is used to determine optical constants of materials by measuring the state of polarization of light after reflection.[95,96] The transverse electric (TE) and transverse magnetic (TM) components of light behave differently upon reflection. In ellipsometry, the ratio of these two components is measured. The fundamental equation is:

$$\frac{r_p}{r_S} = tan(\psi)e^{i\Delta} \tag{3.4}$$

where r_p is the reflection coefficient for p-polarized (TM) waves, and r_S is the reflection coefficient for s-polarized (TE) waves. The experimentally measured quantities, ψ and Δ, are a function of the optical constants and layer thicknesses of a heterostructure, via the Fresnel reflection coefficients. Hence, given measured values of ψ and Δ one can estimate unknown thicknesses and/or optical constants.

Ellipsometry is commonly used to measure the thickness and refractive index of

dielectric films on semiconductors. Applications of ellipsometry to III-V epilayers, however, have been limited. This is partly due to the fact that the epilayers are usually opaque at the wavelength of conventional ellipsometers, making it impossible to measure layer thickness. Furthermore, the presence of surface oxides makes it difficult to accurately measure the optical constants of the epilayers.[97] Recently, spectroscopic ellipsometry has been applied to measure layer thicknesses in multi-layer heterostructures such as field-effect transistors.[98]

3.2 Variable Azimuthal-Angle Ellipsometry

We characterized our InGaAs and InAlAs epitaxial layers with a Gaertner model L116B automated ellipsometer. Both circularly and linearly polarized incident light from a He-Ne laser ($\lambda = 6328\mathring{A}$) were used with the angle of incidence fixed at 70° from vertical. For $In_{0.53}Ga_{0.47}As$, the absorption coefficient at 6328 Å is 9×10^4 cm^{-1}.[88] The corresponding penetration depth is 1100 Å. We estimate $\alpha = 4 \times 10^4$ cm^{-1} and $\delta = 2500$ Å for $In_{0.52}Al_{0.48}As$.

The ellipsometer is equipped with a rotating stage; measurements were made as a function of the azimuthal angle α as shown in fig. 3.1. We use the same convention as in chapter 2: $\alpha = 0°$ when the projection of the incident laser (x-ray) beam on the wafer surface is in the [110] direction. We refer to this technique as variable azimuthal-angle ellipsometry (VAAE).[99,100]

We typically observe a systematic variation of Δ as a function of azimuthal angle. As an example, we plot Δ versus α for sample 1530 in fig. 3.2. This sample consists of a single 1000 Å layer of $In_{0.38}Ga_{0.62}As$ on InP. We note the two-fold symmetry with maxima at $\alpha = 90°$ and 270°, corresponding to incident light parallel to the $[1\bar{1}0]$ and $[\bar{1}10]$ directions. The data can be fit with a cosine function of the form:

$$\Delta = A_\Delta + B_\Delta cos[2(\alpha - C_\Delta)] \tag{3.5}$$

where A_Δ, B_Δ, and C_Δ are fitting parameters. The best-fit to (3.5) was calculated by least squares and is shown as a solid line in fig. 3.2. The parameters are: $A_\Delta =$

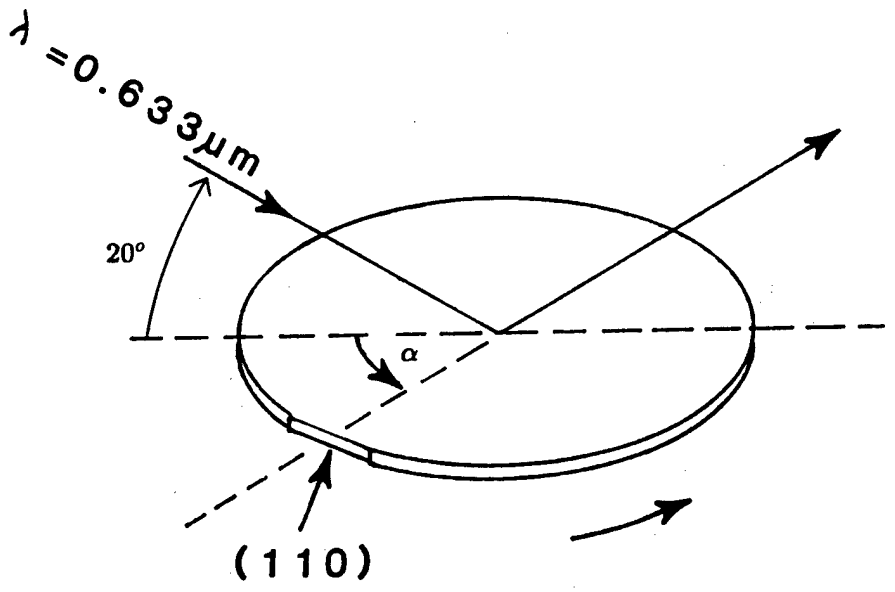

Figure 3-1: Geometry of ellipsometry measurements; α is the azimuthal angle (angle of rotation) of the projection of the beam on the sample with respect to the [110] direction. The angle of incidence is fixed at 20° from horizontal.

145.1°, $B_\Delta = 8.21°$, and $C_\Delta = 90.7°$. For this layer, $t/t_{c,MB} = 9$. As a result of the large mismatch, the crystalline quality is poor, as illustrated by an HRXRD FWHM ratio of 12.

For layers with small mismatch, we still observe cosine-shape variations of Δ with α, but the amplitude of the cosine function, B_Δ, is always small. As an example, we show the data for sample 1877 in fig. 3.3. For this InGaAs layer, $t/t_{c,MB} = 1.1$, the HRXRD scan (fig. 2.5) indicates high crystalline quality, and $B_\Delta = 0.31°$. (The InGaAs layer in 1877 is too thick for a significant portion of the light to reach the InAlAs.)

For a few samples with very large azimuthal variations in Δ, we also observe a small but systematic variations in ψ, with a cosine shape and maxima at $\alpha = 90°$ and 270°. For most samples, however, the variation in ψ with α appears random. We conclude that Δ is more sensitive to optical anisotropy than ψ. Hence, we take B_Δ as a measure of optical anisotropy.

We also observe variations in A_Δ and A_ψ, the average values of Δ and ψ, from sample to sample. We have found, however, that A_Δ and A_ψ vary substantially with

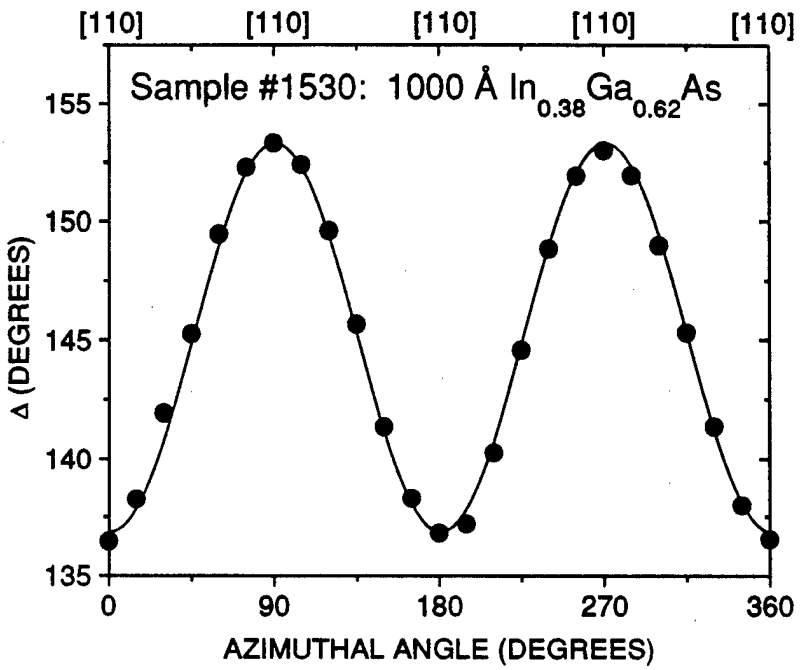

Figure 3-2: Ellipsometric parameter Δ as a function of azimuthal angle for sample 1530, mismatched InGaAs in tension. Solid line is a least-squares fit to eq. (3.5).

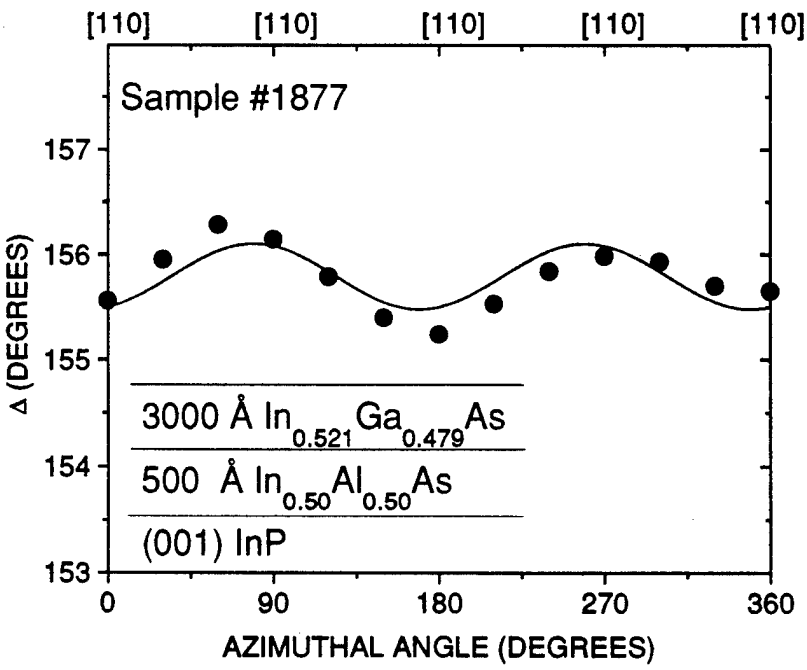

Figure 3-3: Ellipsometric parameter Δ as a function of azimuthal angle for sample 1877, nearly lattice-matched InGaAs. Solid line is a least-squares fit to eq. (3.5).

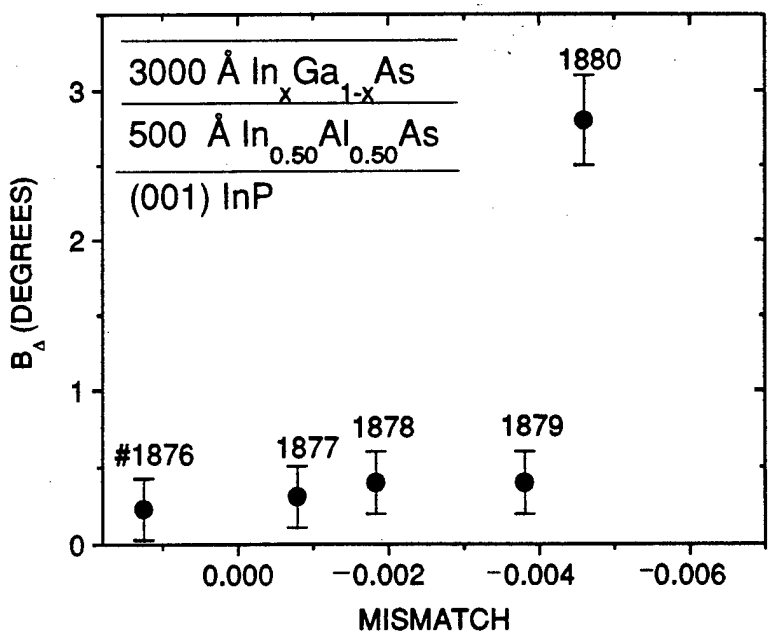

Figure 3-4: Amplitude of the cosine function fits for the ellipsometric parameter Δ as a function of lattice mismatch for a set of InGaAs layers in tension.

position on a single sample. In addition, sample cleaning changes A_Δ and A_ψ. In contrast, B_Δ is relatively insensitive to sample cleaning and position.

We now examine B_Δ for sets of InGaAs layers in tension and compression. In fig. 3.4, we plot B_Δ as a function of mismatch for samples 1876-1880, 3000 Å layers of InGaAs in tension. The HRXRD rocking curves for this set are shown in fig. 2.5. Within the experimental error bars, the OA is constant ($B_\Delta = 0.2 - 0.4°$) for 1876-1879; these samples have HRXRD FWHM ratios close to unity and Pendellosung fringes. In contrast, sample 1880 exhibits degraded crystalline quality and a larger OA, with $B_\Delta = 2.8°$.

The OA follows a similar pattern for samples 1630-1634, 1000 Å layers of InGaAs in compression. B_Δ is plotted as a function of mismatch in fig. 3.5; the HRXRD scans were given in fig. 2.6. The OA is small for the samples with narrow x-ray peaks (1630, 1632, and 1633) and large for the sample (1634) with a broadened x-ray rocking curve.

Optical anisotropy was also observed for InAlAs layers.[66] As an example of a structure with large anisotropy, in fig. 3.6 we plot Δ versus α for sample 1843,

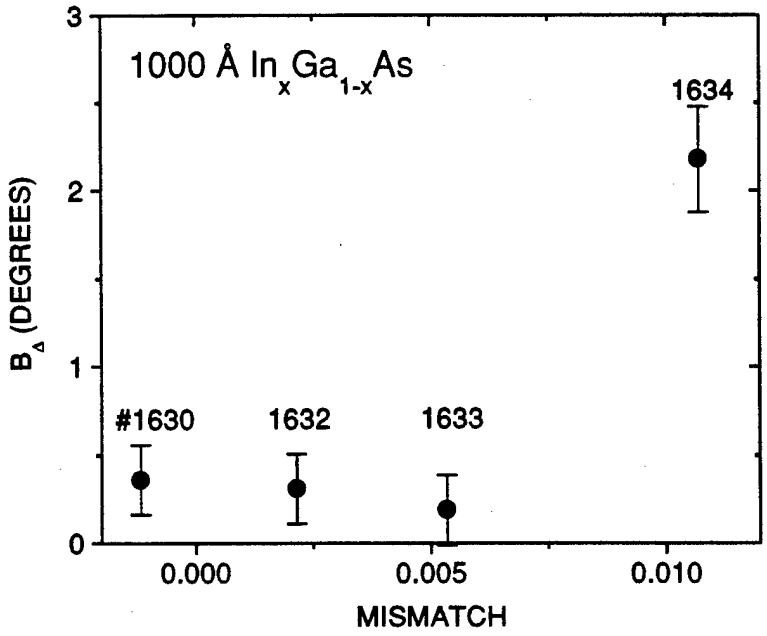

Figure 3-5: Amplitude of the cosine function fits for the ellipsometric parameter Δ as a function of lattice mismatch for a set of InGaAs layers in compression.

a 3000 Å layer of $In_{0.65}Al_{0.35}As$. As with InGaAs, the data approximately follow a cosine law with maxima at $\alpha = 90°$ and 270°. The OA of InAlAs samples also correlates with HRXRD results. For 1843, the HRXRD FWHM ratio is 23, $B_\Delta = 7.1°$, and $t/t_{c,MB} = 20$. In fig. 3.7, we plot B_Δ versus lattice mismatch for samples 3098-3102, 1000 Å layers of InAlAs in compression (see fig. 2.8 for HRXRD scans). The anisotropy is largest for samples 3100, 3101, and 3102. These three samples have inferior HRXRD rocking curves.

As shown in the figures 3.2-3.7, we have observed large optical anisotropies for InGaAs in tension, InGaAs in compression, and InAlAs in compression. In each case, the orientation dependence is the same. We usually do not, however, observe large anisotropies for InAlAs in tension (AlAs-rich). For the 1701-1705 sample set, HRXRD scans (fig. 2.7) revealed structural degradation for two samples, but B_Δ was about 0.3° for all five samples. In chapter 6, we will discuss possible reasons for the differences in InAlAs layers in tension and compression.

We have demonstrated that OA is small for small lattice mismatch and usually becomes large when mismatch increases and crystalline quality deteriorates. For sev-

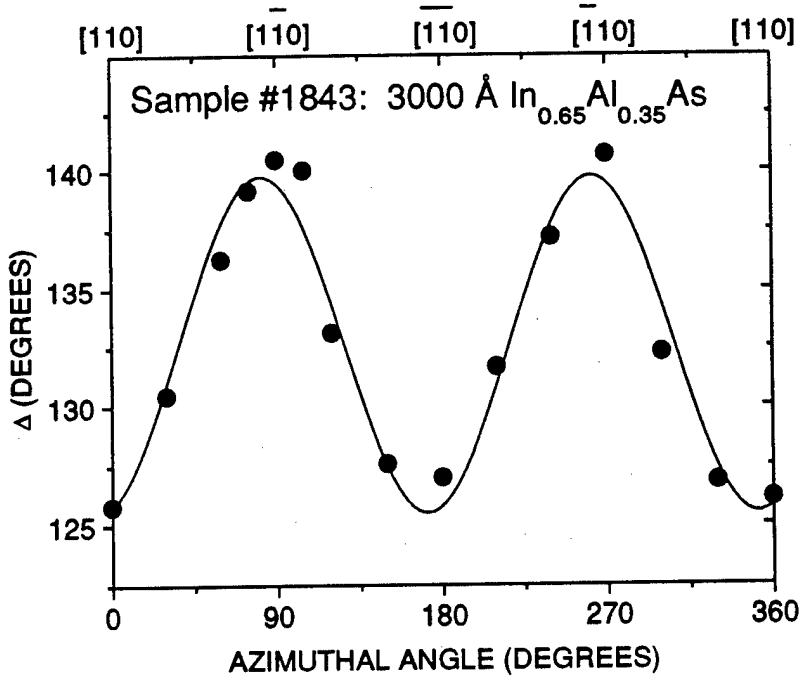

Figure 3-6: Ellipsometric parameter Δ as a function of azimuthal angle for sample 1843, InAlAs in compression. Solid line is a least-squares fit to eq. (3.5).

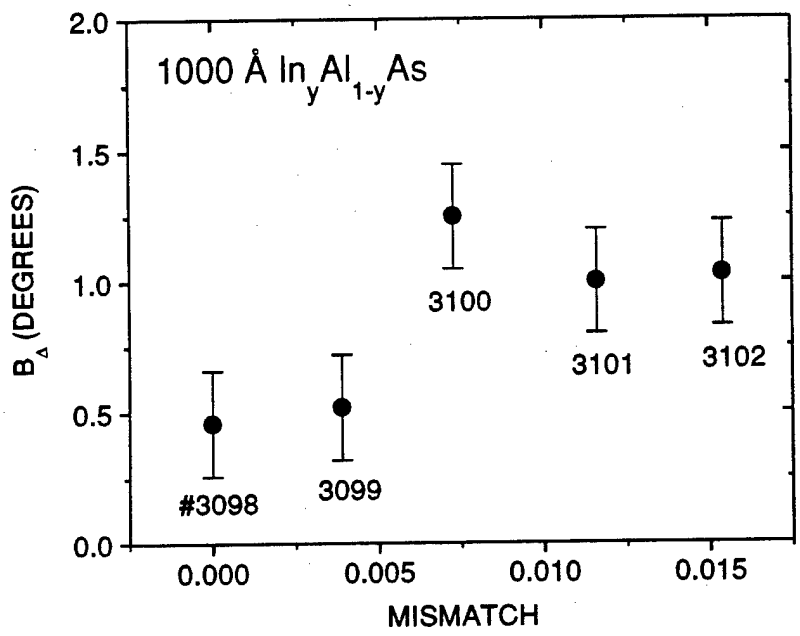

Figure 3-7: Amplitude of the cosine function fit for the ellipsometric parameter Δ as a function of lattice mismatch for a set of InAlAs layers in compression.

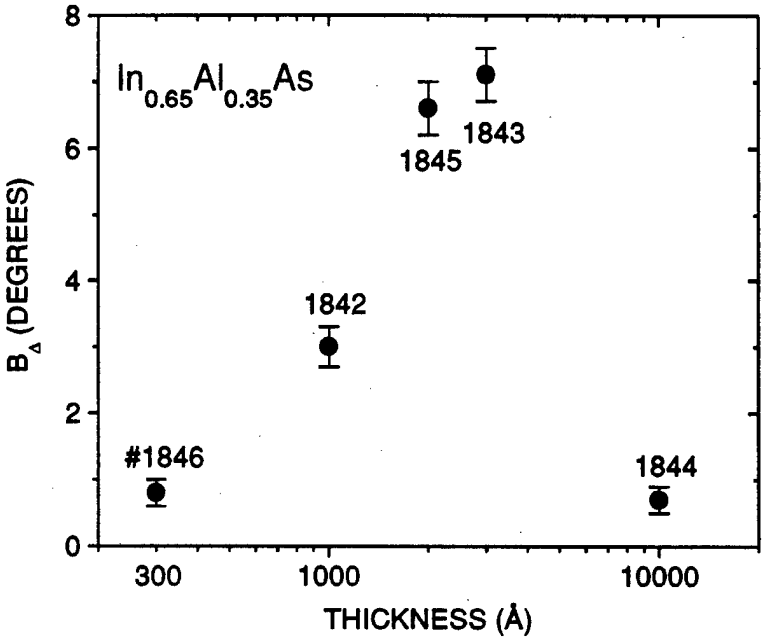

Figure 3-8: Amplitude of the cosine function fit for the ellipsometric parameter Δ as a function of thickness for a set of InAlAs layers in compression.

eral sets of samples, we have also observed that the OA decreases when the mismatch or thickness becomes too large. An example is shown for samples 1842-1846 in fig. 3.8. Each sample contains a single layer of $In_{0.65}Al_{0.35}As$. The OA initially increases with layer thickness but then drops to a small value ($B_\Delta = 0.7°$) at 10,000 Å. We have also observed this behavior for InGaAs in tension and compression.

To confirm the apparent connection between OA and crystalline quality, we plot B_Δ versus the HRXRD FWHM ratio for our entire set of samples in fig. 3.9.[†] For InGaAs (fig. 3.9a) it is obvious that much larger values of optical anisotropy occur in tension than in compression, but several of the layers in compression have B_Δ's which are clearly larger than the values for nearly lattice-matched samples. The OA is always small ($B_\Delta < 0.8°$) when the FWHM ratio is less than 1.5. In chapter 2, we used a similar FWHM ratio, 1.8, as a cutoff for "high" crystalline quality.[‡]

[†]We excluded multilayer samples except for a few two-layer structures with a nearly lattice-matched buffer layer such as samples 1876-1880.

[‡]Three of the four layers in fig. 3.9a with $B_\Delta > 1.0°$ and FWHM ratios between 1.5 and 1.8 were thin ($t \leq 1000\mathring{A}$). For such thin layers, we expect HRXRD to be less sensitive to crystalline imperfection than for thicker layers because the peaks are intrinsically broad. Hence, for thin layers VAAE may detect degradation in crystalline quality before HRXRD.

For InGaAs, we conclude that large OA correlates with a degradation in crystalline quality. Figure 3.9a includes many samples with a large FWHM ratio and small B_Δ. Hence, a small value of OA does not always imply good crystalline quality.

For InAlAs (fig. 3.9b), we observe several compressively-strained samples with large optical anisotropies, but only one sample in tension has a B_Δ greater than 1°. We again observe that the OA is always small for samples with high crystalline quality. We also note that for both InAlAs and InGaAs, B_Δ is always positive, even for the samples with small OA. If the true OA were zero for nearly lattice-matched samples, we would expect experimental noise to result in positive and negative values of B_Δ. We conclude that even the small optical anisotropies are real.

Morris *et al.*[101] recently applied the VAAE technique to InGaAs grown by MOCVD. They measured significant anisotropies for 3.0 μm layers of $In_{0.16}Ga_{0.84}As$ on GaAs. Their observed maximum values of Δ were apparently in the same direction as ours. This result demonstrates that optical anisotropies are not confined to MBE-grown layers.

3.3 Reflectance Difference Spectroscopy

Reflectance difference spectroscopy (RDS) was invented in 1985.[102,103] In this technique, light is reflected from a sample at near-normal incidence and the reflectance is measured in 2 different directions. The incident light is linearly polarized. In the case of an (001) substrate, the light is polarized at 45° to the [110], hence illuminating the [110] and [1$\bar{1}$0] directions equally, as shown in fig. 3.10. The reflected light is measured in the [110] and [1$\bar{1}$0] directions. We define:

r_{110} = complex reflectance parallel to the [110] axis of substrate

$r_{1\bar{1}0}$ = complex reflectance parallel to the [1$\bar{1}$0] axis of substrate

If the sample is isotropic, $r_{110} = r_{1\bar{1}0}$ and the reflected light simply reconstructs the linear polarization of the incident light. Any anisotropy in the sample will result in $r_{110} \neq r_{1\bar{1}0}$. RDS can measure reflectance differences as small as 5×10^{-5}.[104]

A major difference between RDS and ellipsometry is that ellipsometric measure-

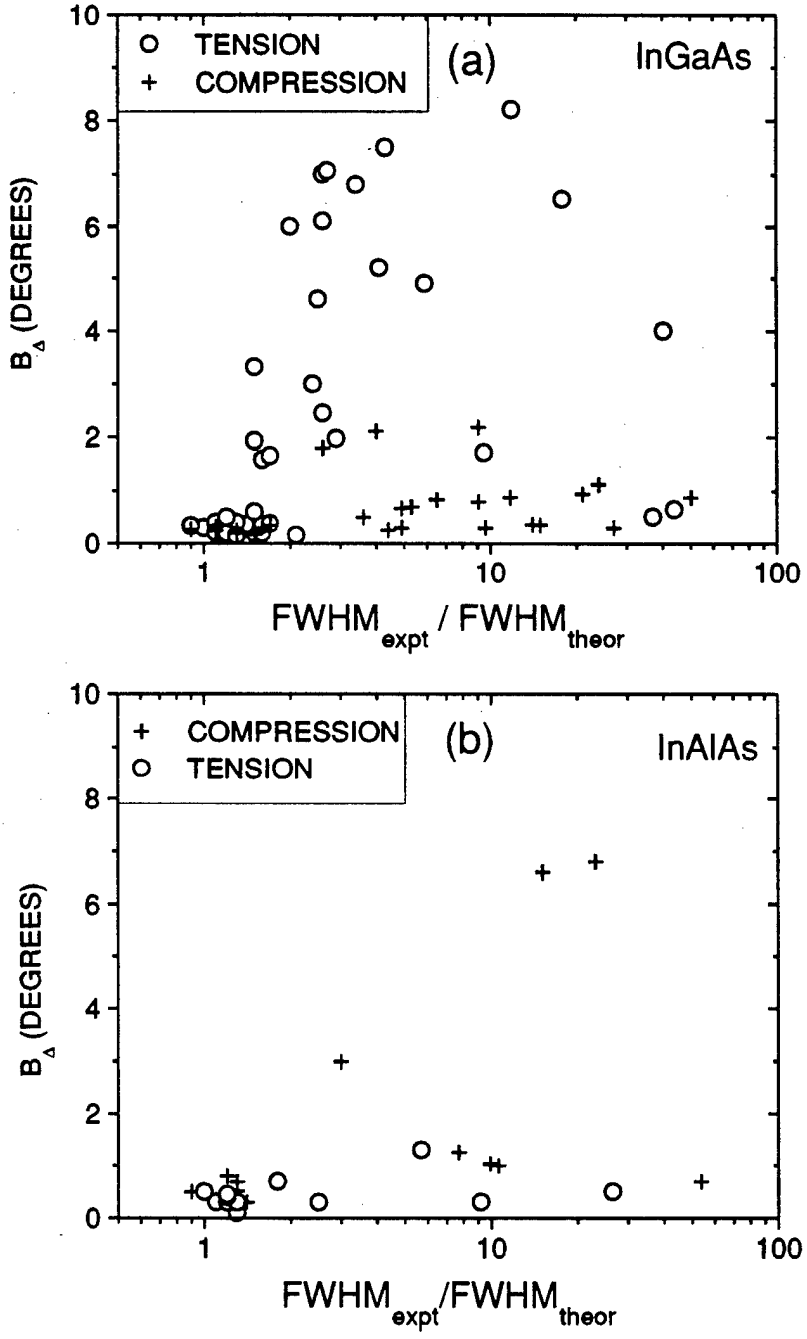

Figure 3-9: Amplitude of the cosine function fit for the ellipsometric parameter Δ as a function of the ratio of the HRXRD experimental and theoretical (004) peak widths for (a) InGaAs and (b) InAlAs layers.

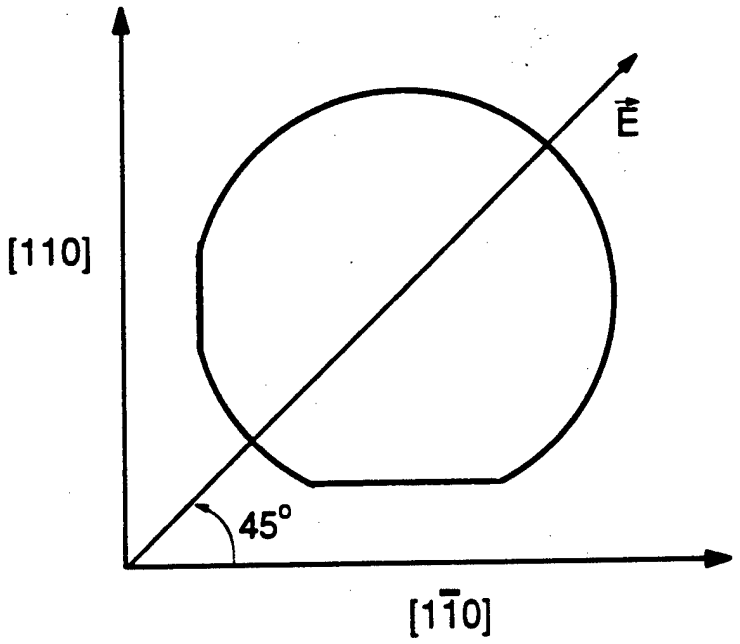

Figure 3-10: Polarization of incident light with respect to the crystallographic directions of the sample for reflectance difference spectroscopy on an (001) substrate.

ments are made at an oblique angle of incidence. Hence, even isotropic samples cause a change in polarization. It is this change in polarization that is measured and used to estimate layer thickness and refractive index in ellipsometry. If the sample is optically anisotropic, the analysis becomes very difficult. With RDS, however, the only factor that changes the polarization is optical anisotropy.

We investigated a variety of matched and mismatched InGaAs/InP and InAlAs/InP heterostructures, measuring reflectance differences over the energy range of 1.5 to 5.5 eV. Typical results are shown in figs. 3.11 and 3.12 where we plot both the magnitude, $|\Delta r/r|$, and phase, $\Delta\beta$, of:

$$\frac{\Delta r}{r} = \frac{r_{1\bar{1}0} - r_{110}}{r_{1\bar{1}0} + r_{110}} \tag{3.6}$$

for samples 1879 and 1880 (see figs. 2.5 and 3.4 for HRXRD and VAAE data). The vertical scales differ by a factor of ten on the two plots. The magnitudes of the optical anisotropies for 1879 are less than 0.004 over the entire spectral range.[§]

[§] $|\Delta r/r|$ and $\Delta\beta$ can be determined from a single RDS measurement. The resolution is improved if $|\Delta r/r|$ and $\Delta\beta$ are determined by subtracting two measurements which are taken 90° apart. We

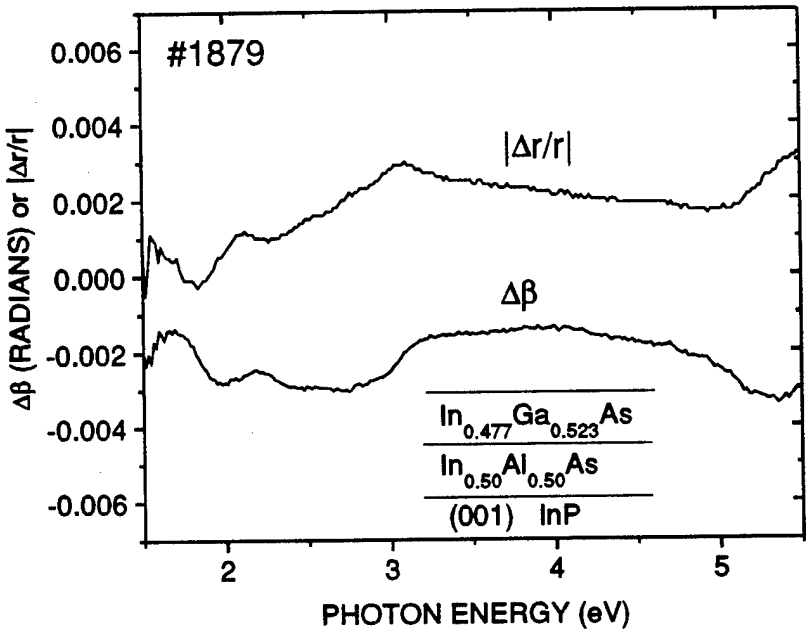

Figure 3-11: Magnitude and phase of RDS signal as a function of photon energy for 1879, a sample with good crystalline quality.

($|\Delta r/r|$ is dimensionless; $\Delta\beta$ has units of radians.) In contrast, 1880 exhibits much larger anisotropies, with $|\Delta r/r|$ and $\Delta\beta$ reaching 0.062 and -0.027, respectively. The relative magnitudes are in qualitative agreement with our ellipsometry measurements which yielded B_Δ values of 0.4° and 2.8° for 1879 and 1880, respectively.

For all 25 samples measured by RDS, we observed a strong correlation with the optical anisotropy measured by ellipsometry. Our ellipsometry measurements were made at a photon energy of 1.96 eV. For comparison, we plot the values of $|\Delta r/r|$ and $\Delta\beta$ at 1.96 eV versus B_Δ for both InGaAs/InP and InAlAs/InP structures in fig. 3.13. There is clearly a correlation between $|\Delta r/r|$ and B_Δ, and an even stronger correlation between $\Delta\beta$ and B_Δ.

3.4 Physical Origin of Optical Anisotropy

We first consider the cause of the relatively small optical anisotropies observed for layers of high crystalline quality. The RDS signal for samples such as 1879 is comparable

used this latter procedure; it accounts for the small, negative values of $|\Delta r/r|$ in fig. 3.11.

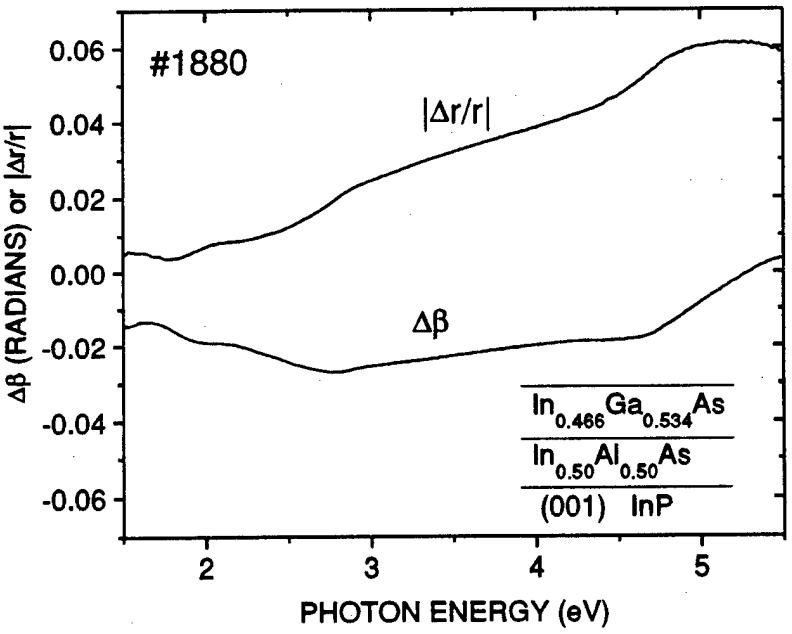

Figure 3-12: Magnitude and phase of RDS signal as a function of photon energy for 1880, a sample with degraded crystalline quality.

in magnitude to RDS signals from bulk GaAs. Aspnes attributed the GaAs results to surface chemistry: for example, the absorption associated with Ga-Ga surface dimer bonds.[104] Similar anisotropies are expected in nearly lattice-matched epilayers. Hence, for layers of high crystalline quality, we attribute the relatively small optical anisotropy (measured by RDS and VAAE) to surface chemistry.

We have observed large optical anisotropies in layers ranging from a few hundred angstroms to one micron. Since the penetration depth in our epilayers is 1000 to 3000 Å, virtually none of the light can penetrate through a one micron layer to the layer/substrate interface. We conclude that the origin of the large OA is in the top few thousand angstroms of epilayer, not the substrate or the interface.

One possible explanation for the large OA in mismatched layers is the piezo-optical effect, a strain-induced change in refractive index.[75,105] If piezo-optical effects were dominant, we would expect the largest anisotropies in samples with a large difference in strain in the [110] and [1$\bar{1}$0] directions. The strain in the [110] direction is equal to $(\Delta a/a)_r - (\Delta a/a)_{\|[110]}$ and similarly for the [1$\bar{1}$0] direction. Hence, the difference in strain is $(\Delta a/a)_{\|[110]} - (\Delta a/a)_{\|[1\bar{1}0]}$. In fig. 3.14, we plot B_Δ as a function of the

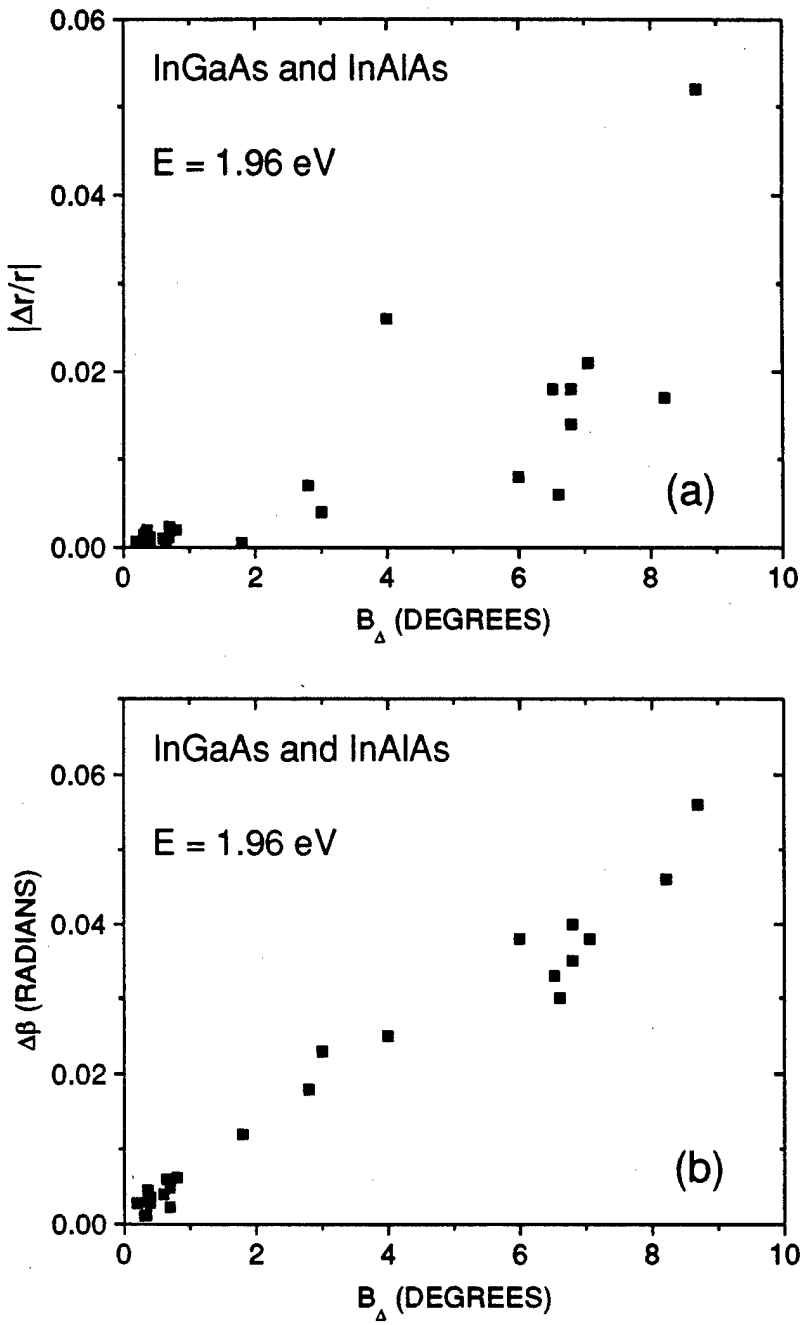

Figure 3-13: Comparison of a) magnitude, and b) phase, from reflectance difference spectroscopy with anisotropy parameter from variable azimuthal angle ellipsometry. The photon energy is 1.96 eV for both techniques.

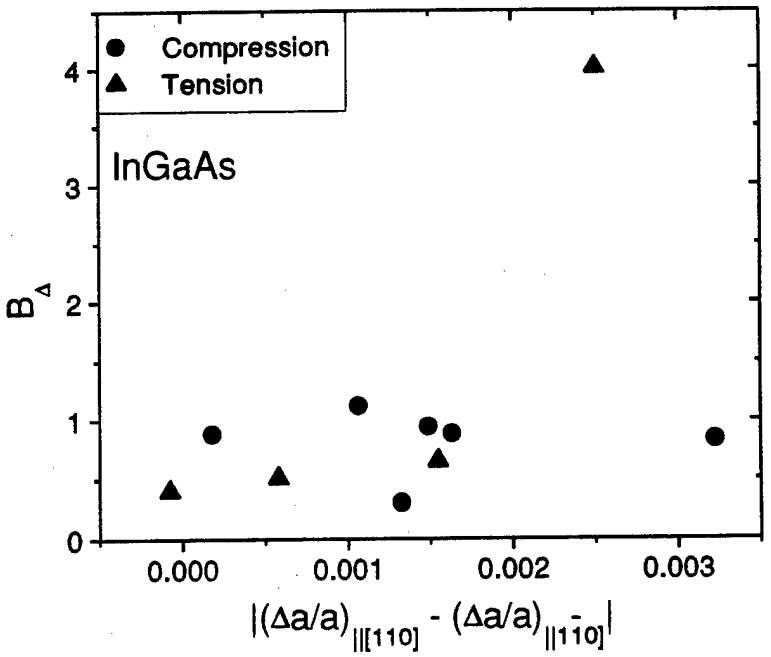

Figure 3-14: Optical anisotropy as a function of the difference in strain in the [110] and [1$\bar{1}$0] directions for partially relaxed InGaAs layers.

strain difference for partially relaxed InGaAs layers. With one exception, the samples do not have large OA, despite the large asymmetries in strain. Many samples (see fig. 3.9) exhibit large OA, but are essentially unrelaxed and hence do not have strain asymmetries. Furthermore, piezo-optical effects should produce a reversal in the direction of the OA when changing from tension to compression. Our epilayers exhibited the same pattern for both tension and compression. In addition, piezo-optical effects are expected to exhibit large changes near the critical points in energy, but we observe no such features in our RDS data. Hence, we conclude that piezo-optical effects are not the dominant mechanism for optical anisotropy.

As mentioned in chapter 1, composition modulation may occur in InGaAs and InAlAs layers. We considered it as a potential cause of optical anisotropy. We obtained plan-view transmission electron microscopy (TEM) images of eight samples.[¶] One of the InAlAs samples, 3099, exhibited contrast modulation as shown in fig. 3.15. The contrast modulation has a period of 365 Å. We believe it is associated with variations in composition. X-ray measurements on this sample (fig. 2.8) reveal good crystalline

[¶]TEM by F. Peiro and Prof. A. Cornet at the Univ. of Barcelona

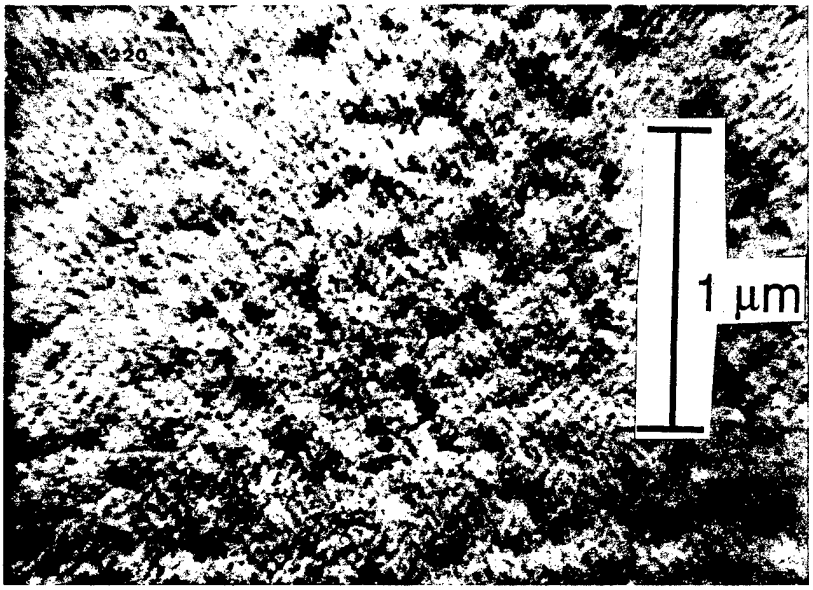

Figure 3-15: Plan-view transmission electron micrograph for sample 3099, 1000 Å of $In_{0.579}Al_{0.421}As$. A bright-field, two-beam image with g=[220] was used. A contrast modulation with a period of 365 Å is visible along the < 100 > directions.

quality. The OA (fig. 3.7) was small. The lack of OA in a single sample with composition modulation is not definitive. We note, however, that the modulation is in a < 100 > direction. This is in agreement with other reports.[51,52,106] The < 100 > directions correspond to α = 45, 135, 225, and 315° on figures such as 3.2. Hence, composition modulation could only produce optical anisotropies in these directions, not along the [110] and [1$\bar{1}$0] as observed.

Sun *et al.* reported large asymmetries in the electron mobility for MOCVD-grown InGaAs/GaAs heterostructures.[107] They suggest that the formation of islands is responsible. Islands are known to extend faster in the [110] direction than in the [1$\bar{1}$0] direction in MOCVD.[108] Such a mechanism might also explain our results. In MBE, the preferential growth direction is perpendicular to that in MOCVD.[109,110] Thus, we could expect islands elongated along the [1$\bar{1}$0] direction when three-dimensional growth occurs. Such islands were observed in the InGaAs/GaAs system.[35] It is plausible that elongated islands would affect a layer's optical properties.

Further support to the theory of elongated islands is found in the work of Acher *et al.*[111,112] They performed *in situ* RDS measurements during the growth of InAs

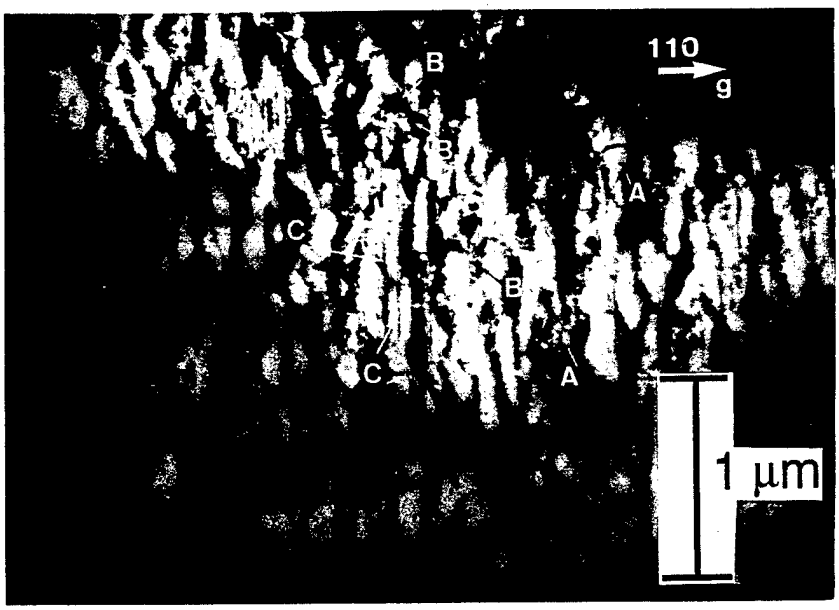

Figure 3-16: Plan-view transmission electron micrograph for sample 1530. The image was taken under bright-field, two-beam conditions with g = [220]. Agglomerations of threading dislocations are observed (A). Islands aligned along [1$\bar{1}$0] are clearly visible (B). Misfit dislocations appear to have formed (C) but are partially masked by other features.

on InP and InP on GaAs by MOCVD. Optical anisotropies up to 5% for InAs/InP and over 100% for InP/GaAs were observed. They attempted to fit their data with models based upon roughness anisotropy at both the epilayer/substrate interface and the epilayer surface. The models (with fitting parameters) gave reasonable agreement to the observed optical anisotropies as a function of growth time.

To confirm the existence of elongated islands or roughness anisotropy, we obtained TEM micrographs of sample 1530 which has a large OA (fig. 3.2). In fig. 3.16, we show the plan-view image. The TEM micrograph reveals three-dimensional growth with islands along the [1$\bar{1}$0] direction. Cross-sectional TEM (fig. 3.17) shows that the film is continuous, but has a very irregular morphology, with layer thickness ranging from 830 to 1400 Å. Stacking faults are also observed.

We also obtained plan-view TEM micrographs of samples 1879 and 1880, figs. 3.18 and 3.19. For 1879, the surface morphology was smooth, indicative of two-dimensional growth. Only a few misfit dislocations were found. The intersection of two dislocations is shown in the figure. These dislocations were confirmed to be

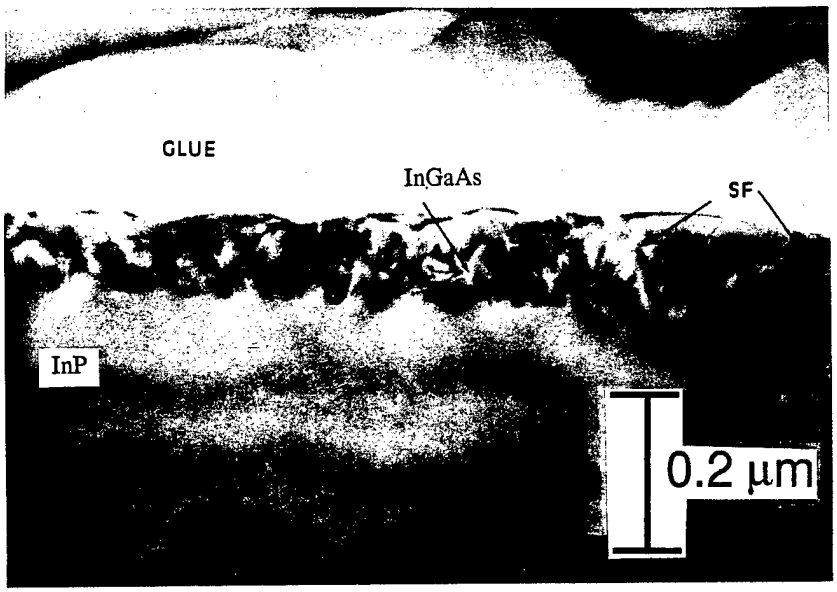

Figure 3-17: Cross-section transmission electron micrograph for sample 1530. The image was taken in the [110] direction under a g = [2$\bar{2}$0] bright-field condition. Note the variations in epilayer thickness and stacking faults (SF).

of the 60°-type.[113] This sample exhibited excellent crystalline quality (fig. 2.5) and small OA (figs. 3.4 and 3.11). In contrast, TEM reveals a rough surface morphology with hillocks for sample 1880. Dislocations are also visible, but in the [1$\bar{1}$0] direction only, with an average spacing of about 1.5 μm. The sample has a large OA (figs. 3.4 and 3.12) and degraded structural quality (fig. 2.5). Elongated islands are not clearly visible on sample 1880 as they were on sample 1530. The OA for sample 1880, although large compared to lattice-matched samples, is much smaller than sample 1530.

As mentioned earlier, we often observe that the OA of mismatched layers returns to a small value when the layer thickness becomes too large. This usually occurs when the layer begins to relax substantially ($\bar{R} > 10\%$). A TEM image of such a sample (not shown) revealed poor crystalline quality, with $> 10^{10}$ cm^{-2} threading dislocations and stacking faults. We do not believe that the layer has returned to smooth, two-dimensional growth. Instead, the growth is thought to be rough or three-dimensional, but relatively isotropic. We note that Acher *et al.* also observed the OA returning to a small value when the thickness of InAs on InP reached 3000 Å.[112]

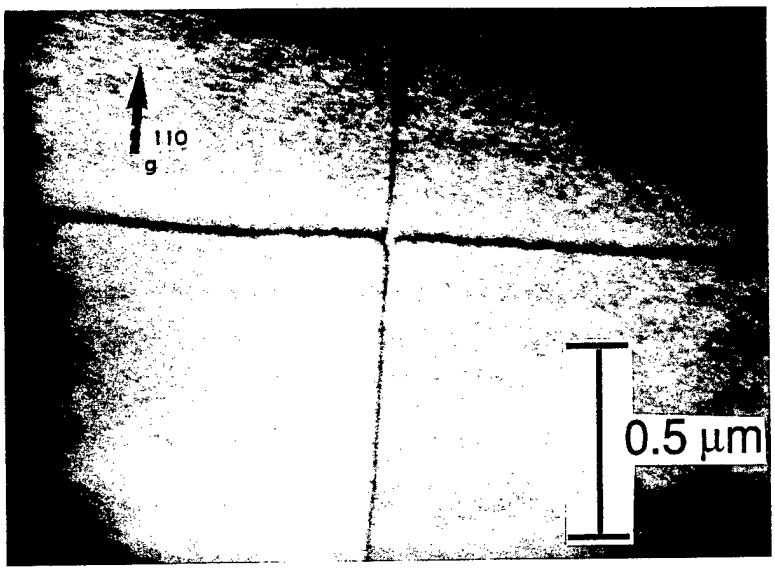

Figure 3-18: Plan-view transmission electron micrograph for sample 1879 with g = [220]. Two intersecting 60° misfit dislocations are visible. The morphology is smooth, indicating two-dimensional growth.

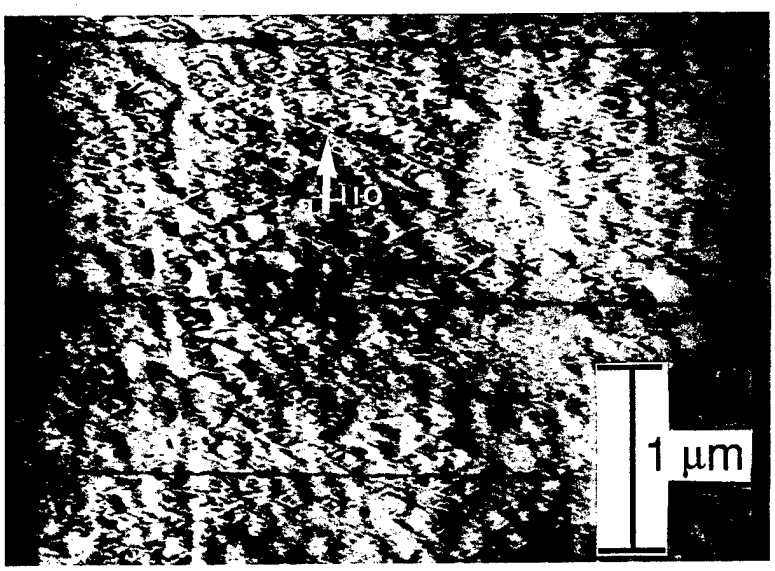

Figure 3-19: Plan-view transmission electron micrograph for sample 1880 with g = [220]. Misfit dislocations are visible along the $[1\bar{1}0]$ direction only. The surface morphology is rough, with hillocks elongated toward [110] and $[1\bar{1}0]$.

3.5 Summary

We developed a new technique, variable azimuthal-angle ellipsometry, for measuring optical anisotropy. We observed anisotropy in InGaAs/InP and InAlAs/InP heterostructures using both VAAE and Reflectance Difference Spectroscopy. For nearly lattice-matched epilayers with high crystalline quality (measured by HRXRD), the optical anisotropy is always small but non-zero. We attribute this small anisotropy to surface chemistry. For samples with larger mismatch and degraded crystalline quality, the optical anisotropy is often large. Based upon a comparison to TEM images and other arguments, we conclude that large anisotropies result from strain-induced surface roughness, possibly associated with three-dimensional growth.

Chapter 4

Relaxation Kinetics and Thermal Stability

In chapter 2, we demonstrated that complete relaxation of epilayer strain does not occur when the equilibrium critical layer thickness is reached. Similar results in other material systems have been attributed to metastability. The assumption is that misfit dislocations do not form or propagate during growth due to kinetic barriers. This suggests that layers beyond $t_{c,MB}$ with high crytalline quality may relax during high-temperature processing steps or device operation. If so, they would not be suitable for most device applications. Our primary goals in this chapter are to assess the thermal stability of high-quality strained InGaAs and InAlAs layers and to understand the kinetics of relaxation during growth and annealing.

We assessed the thermal stability of our epilayers by two techniques. In section 4.1, we describe the use of HRXRD to measure structural changes resulting from high-temperature anneals. In section 4.2, we study the effect of annealing on the electron mobility in MODFETs with mismatched InGaAs channels. We examine relaxation kinetics in section 4.3, comparing our as-grown relaxation data to a published model. We then explain the thermal stability of our mismatched layers by considering the energetics for nucleation of dislocation half-loops. Our findings are summarized in section 4.4.

4.1 Annealing: Structural Stability

We assessed the thermal stability of mismatched InGaAs and InAlAs layers by HRXRD measurements before and after rapid thermal annealing (RTA). The anneals were performed in an AG Associates Heatpulse 210 system with a nitrogen ambient. Samples were placed face-down on a GaAs wafer during the anneal to minimize thermal decomposition. The temperature was measured by a thermocouple attached to a Si wafer and is believed to be accurate to within 10°C. For MBE-grown $In_xGa_{1-x}As$ and $In_yAl_{1-y}As$, we typically observe variations in x or y of 0.005 across a sample. Such variations could be mistaken for relaxation during annealing. To avoid this problem, we performed sequential anneals on small (~5 x 5 mm) pieces, measuring HRXRD rocking curves after each anneal.

We begin by considering a layer which relaxed substantially during growth. Sample 1441 consists of 1.0 μm of $In_{0.61}Ga_{0.39}As$ on InP. The (004) HRXRD rocking curve is shown in fig. 4.1. Based upon this and (115) scans, we determined that $\bar{R}$ was 52% before annealing. We annealed the sample for 60 seconds at 850°C. As shown in fig. 4.2, annealing caused the layer peak to move closer to the substrate peak. This shift results from additional relaxation, with $(\Delta a/a)_{||}$ increasing and $(\Delta a/a)_{\perp}$ decreasing. After the first anneal, $\bar{R}$ = 67%. We performed additional 2-minute and 7-minute 850°C anneals (not shown) on the same piece of 1441 and observed further relaxation, with $\bar{R}$ = 70% and 75%, respectively. We note that after the second and third anneals at 850°C, severe degradation of the surface was obvious to the naked eye, despite the use of a GaAs cap. Hence, it may not be feasible to achieve complete relaxation by annealing samples such as 1441. Based upon these results, we use 850°C as an upper limit for annealing temperature.

The InGaAs layer of sample 1441 was 33 times $t_{c,MB}$, and, as expected, exhibited poor crystalline quality even before annealing. For most device applications, layers of high crystalline quality are required. We devote the rest of this and the following section to the thermal stability of high-quality strained layers.

We are primarily interested in lattice relaxation, but interdiffusion may also occur

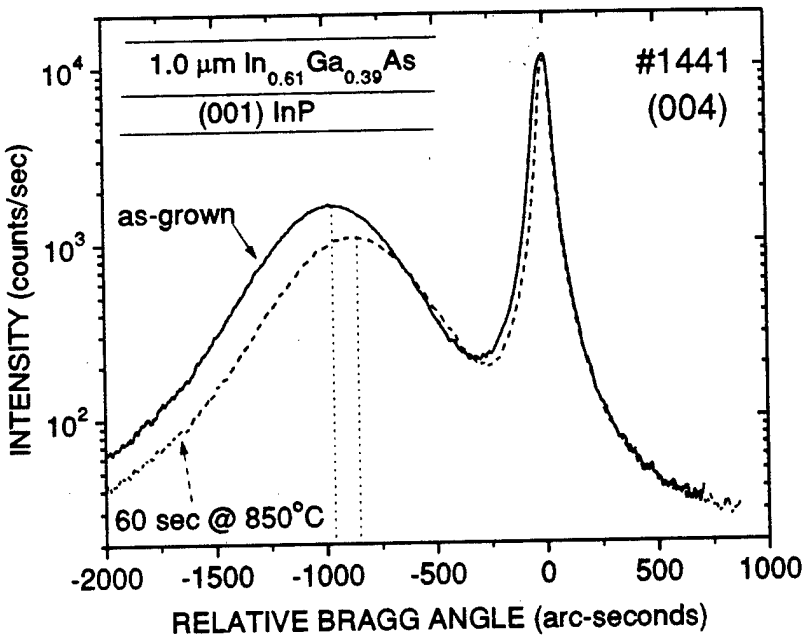

Figure 4-1: HRXRD scans of sample 1441, a partially relaxed layer of InGaAs with $t/t_{c,MB} = 33$, before and after annealing. The shift in the layer peak indicates lattice relaxation during the anneal.

during high-temperature anneals. Using an interdiffusion coefficient of $D_{int} = 10^{-14}$ cm^2/sec for InGaAs/InP at 850°C,[114] we calculate $\sqrt{D_{int}t} = 77$ Å for a 60 second anneal. This suggests that interdiffusion may degrade the interface. To determine the effect of interdiffusion on HRXRD rocking curves, we performed a series of anneals on a nearly lattice-matched epilayer. Sample 1331 consists of a single 4000 Å layer of $In_{0.537}Ga_{0.463}As$, with $t/t_{c,MB} = 0.5$. This layer should be thermodynamically stable with respect to misfit dislocations. In fig. 4.2, we show the rocking curves before anneals and after 60 seconds at 650, 750, and 850°C. The as-grown curve exhibits Pendellosung fringes and an epilayer FWHM ratio of 1.1, indicating high crystalline quality. Interdiffusion across the epilayer/substrate interface could cause a loss of fringes and a broadening of the layer peak. After annealing, there is a reduction in the fringe intensity on the low-angle side, but no change on the high-angle side. The FWHM ratio remained between 1.1 and 1.3. We conclude that if interdiffusion is occurring, its effect on the HRXRD rocking curves is small.

We now examine the thermal stability of high-quality layers beyond the Matthews-

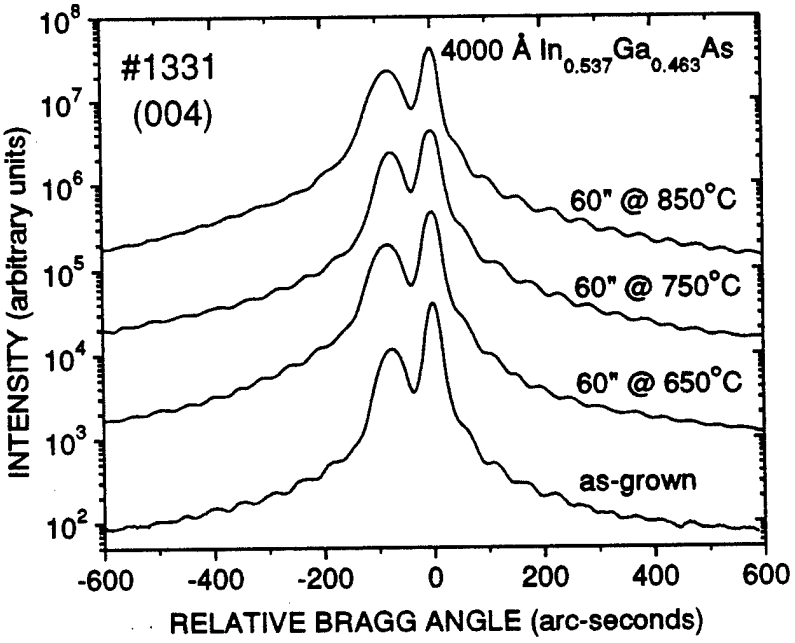

Figure 4-2: HRXRD scans of sample 1331, a coherent layer of InGaAs with $t/t_{c,MB} = 0.5$, before and after annealing.

Blakeslee critical layer thickness. Before discussing our results for InGaAs and InAlAs, it is instructive to consider a published result for the SiGe/Si system. A 1700 Å layer of $Si_{0.82}Ge_{0.18}$ was grown at 500°C and annealed at temperatures from 550°C to 850°C for 60 seconds.[115] The rocking curves are shown in fig. 4.3. For temperatures up to 600°C, almost no changes are observed. After a 650°C anneal, however, the Pendellosung fringes disappear. Higher temperatures cause a broadening of the layer peak and a decrease in the epilayer-substrate peak separation, indicating substantial lattice relaxation. We note that $t/t_{c,MB} = 8$ for this layer.

In fig. 4.4, we show the effects of annealing on sample 1879 which included a 3000 Å layer of $In_{0.477}Ga_{0.523}As$. For the InGaAs layer, $t/t_{c,MB} = 7.3$. The results are quite different than for the SiGe layer, although the growth temperature, layer thickness, and mismatch were similar. The only effect of annealing is a slight loss in fringe intensity, similar to 1331, the nearly lattice-matched "control." We conclude that the strained InGaAs layer is not relaxing during the anneals. As shown in fig. 4.5, InAlAs behaves in a similar way. In this case, the 1800 Å layer of $In_{0.44}Al_{0.56}As$ is 8.6 times $t_{c,MB}$. We will discuss the reason for the different behavior of InGa(Al)As

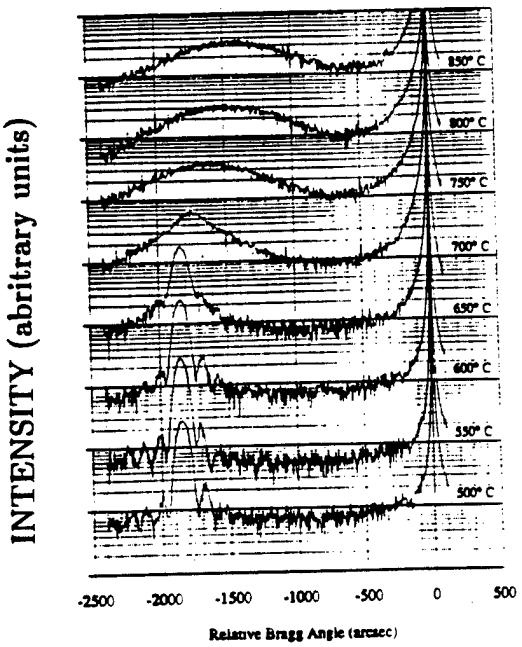

Figure 4-3: HRXRD scans of a 1700 Å layer of $Si_{0.82}Ge_{0.18}$ on Si with $t/t_{c,MB} = 8$. The layer was grown at 500°C and annealed for 60 seconds at 550-850°C.[115]

and SiGe in chapter 6.

We also used HRXRD to examine the structural stability of a device heterostructure. The cross-section of the modulation-doped field-effect transistor (MODFET) is shown in fig. 4.6. All the layers are nominally lattice-matched to the InP substrate except the 500 Å channel. We performed anneals on MODFET 4089 which has an $In_{0.64}Ga_{0.36}As$ channel, with $t/t_{c,MB} = 2.6$. HRXRD scans for as-grown and 60" @ 800°C are shown in fig. 4.7. In this case, different pieces of the wafer were used for the two measurements. Hence, the slight difference in the position of the channel peak is probably a result of wafer nonuniformity. The important finding is that fringes remain after annealing, demonstrating the thermal stability of this pseudomorphic device structure.

4.2 Annealing: Electronic Stability

As discussed in chapter 2, we have improved the sensitivity of HRXRD to crystalline imperfection by examining the FWHM ratio and interference fringes in addition to relaxation. We cannot, however, detect the first misfit dislocations. For example,

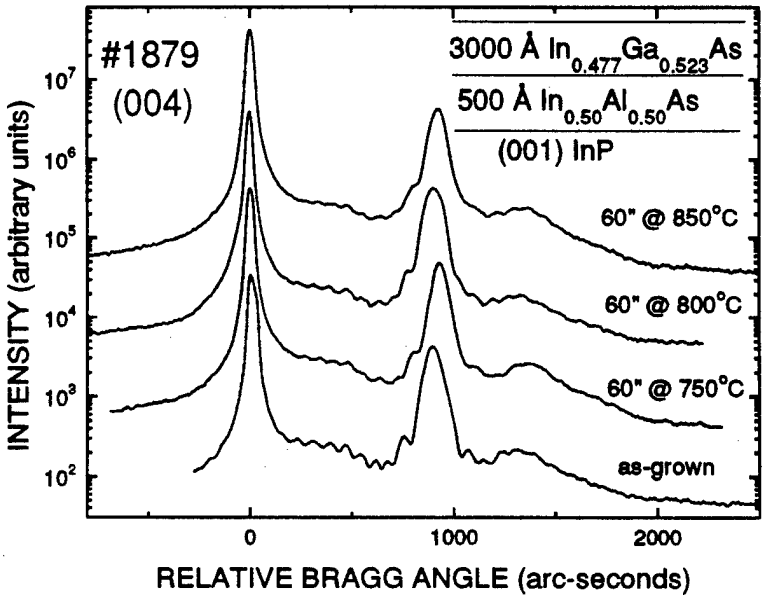

Figure 4-4: HRXRD scans of sample 1879 before and after annealing. The sample includes an InGaAs layer with $t/t_{c,MB} = 7.3$.

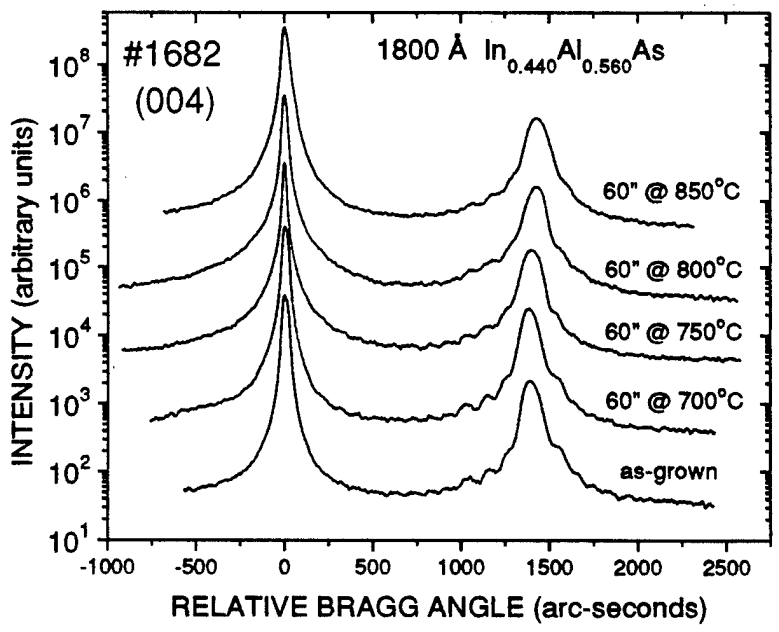

Figure 4-5: HRXRD scans of sample 1682, a single layer of InAlAs with $t/t_{c,MB} = 8.6$, before and after annealing.

50Å	$In_{0.53}Ga_{0.47}As$	cap
200Å	$In_{0.52}Al_{0.48}As$	spacer
200Å	n^+ $In_{0.52}Al_{0.48}As$	doped layer
100Å	$In_{0.52}Al_{0.48}As$	spacer
500Å	$In_xGa_{1-x}As$	channel
1000Å	$In_{0.52}Al_{0.48}As$	buffer
	(001) InP (Fe)	

Figure 4-6: Cross-section of modulation-doped structures used in this study. With the exception of the InGaAs channel, all epilayers are nominally lattice-matched to the InP substrate.

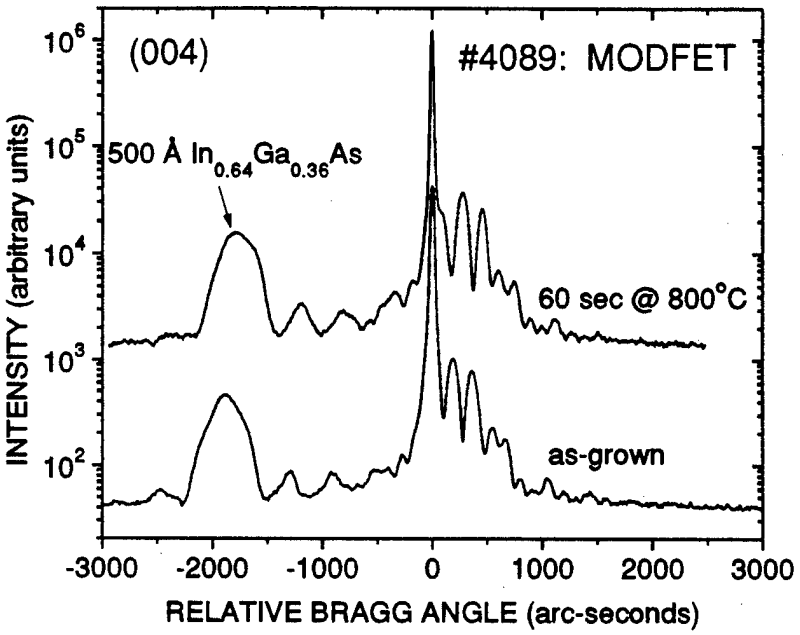

Figure 4-7: HRXRD scans of sample 4089, a MODFET heterostructure, before and after annealing. The InGaAs channel is a factor of 2.6 thicker than $t_{c,MB}$.

sample 1879 has a small FWHM ratio and fringes (fig. 2.5), but TEM reveals misfit dislocations (fig. 3.18); the density is too low to obtain a reliable density. Hence, it is possible that degradation is occuring during our high-temperature anneals, but HRXRD cannot detect it.

The mobility of modulation-doped structures is very sensitive to layer and interface quality.[116] To obtain a measure of thermal stability which is more sensitive than HRXRD, we grew MODFET structures with mismatched channels and measured the electron mobility before and after anneals. The basic structure was given in fig. 4.6. The Si dopant atoms are placed in a high band-gap InAlAs layer. Most electrons donated by the Si diffuse into the low band-gap InGaAs layer (channel) which is free of dopant atoms and hence has a high mobility. In this way, both high carrier concentration and high mobility are achieved simultaneously.

The mobility of MODFETs is a function of both the background carrier concentration in the channel and the abruptness of interfaces. Interdiffusion of In, Ga, and Al during annealing will make the interfaces less abrupt. In addition, Si might diffuse through the 100 Å spacer and into the channel, lowering the mobility. The diffusion

of Si in GaAs has been shown to occur via a Si^{+}_{Ga}-Si^{-}_{As} complex.[117] The diffusion coefficient for the complex is 2×10^{-13} cm^2/sec at 800°C. For a 5" anneal, $\sqrt{Dt} =$ 100 Å. The diffusion coefficient of Si in InAlAs is probably different, so this is at best an order-of-magnitude calculation. It does suggest, however, that Si diffusion may be a problem. We again need a control sample to let us separate the effects of interdiffusion and relaxation.†

We investigated three MODFET structures, each with a 500 Å $In_xGa_{1-x}As$ channel. Sample 4168 was nominally lattice matched. As expected, the channel did not give a distinct HRXRD peak, but we are confident that $x = 0.53 \pm 0.01$ and $t/t_{c,MB} \ll 1$. For MODFET 4089, HRXRD gives $x = 0.64$ (fig. 4.7), and $t/t_{c,MB} =$ 2.6. For MODFET 4084, $x = 0.68$ (fig. 2.10), and $t/t_{c,MB} = 3.8$.

Initially, we tried to perform successive anneals on a single piece of a sample. We observed anomalous results, apparently due to diffusion of the In used for ohmic contacts during the high-temperature anneals (600-800°C). Instead, we scribed each sample into several $\sim 5 \times 5$ mm pieces. Some pieces were annealed at high temperatures before the formation of the ohmic contacts and the Hall/van der Pauw (HVDP) measurements. Others were only subjected to a 375°C contact anneal, presumably yielding the as-grown mobility, μ, and sheet carrier concentration, n_S. We observed nonuniformities in μ and n_S of 5 to 15% across each sample.

We plot the electron mobility and sheet carrier concentration as a function of anneal temperature and time in fig. 4.8 (room-temperature HVDP measurements) and fig. 4.9 (77K). We measured 3-4 pieces without high-temperature anneals on each wafer. The error bars shown are the standard deviations of these measurements.

For sample 4168, the control, the changes in μ_{300K} with annealing are relatively small and may reflect as-grown nonuniformities. The changes in $n_{S,300K}$, however, are much larger than the error bar. Annealing causes a large reduction in $n_{S,300K}$, with a decrease of a factor of 5 after 60" at 800°C. It is well known that Si can be an amphoteric dopant in III-V compounds. We speculate that $Si^{+}_{In,Al}$-Si^{-}_{As} complexes are

†A complete separation of the effects may not be possible since strain is known to enhance diffusion.

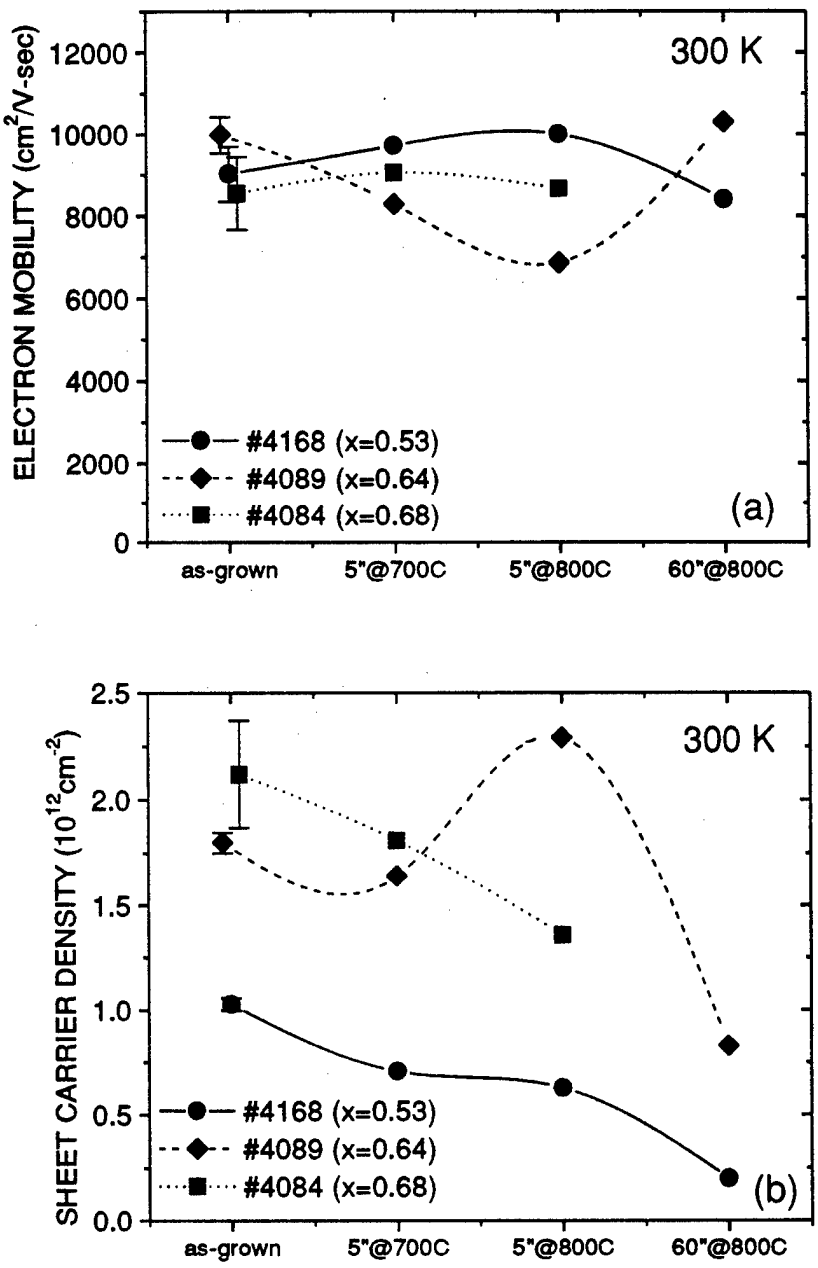

Figure 4-8: Electron mobility (a) and sheet carrier concentration (b) at 300 K as a function of annealing for MODFET heterostructures.

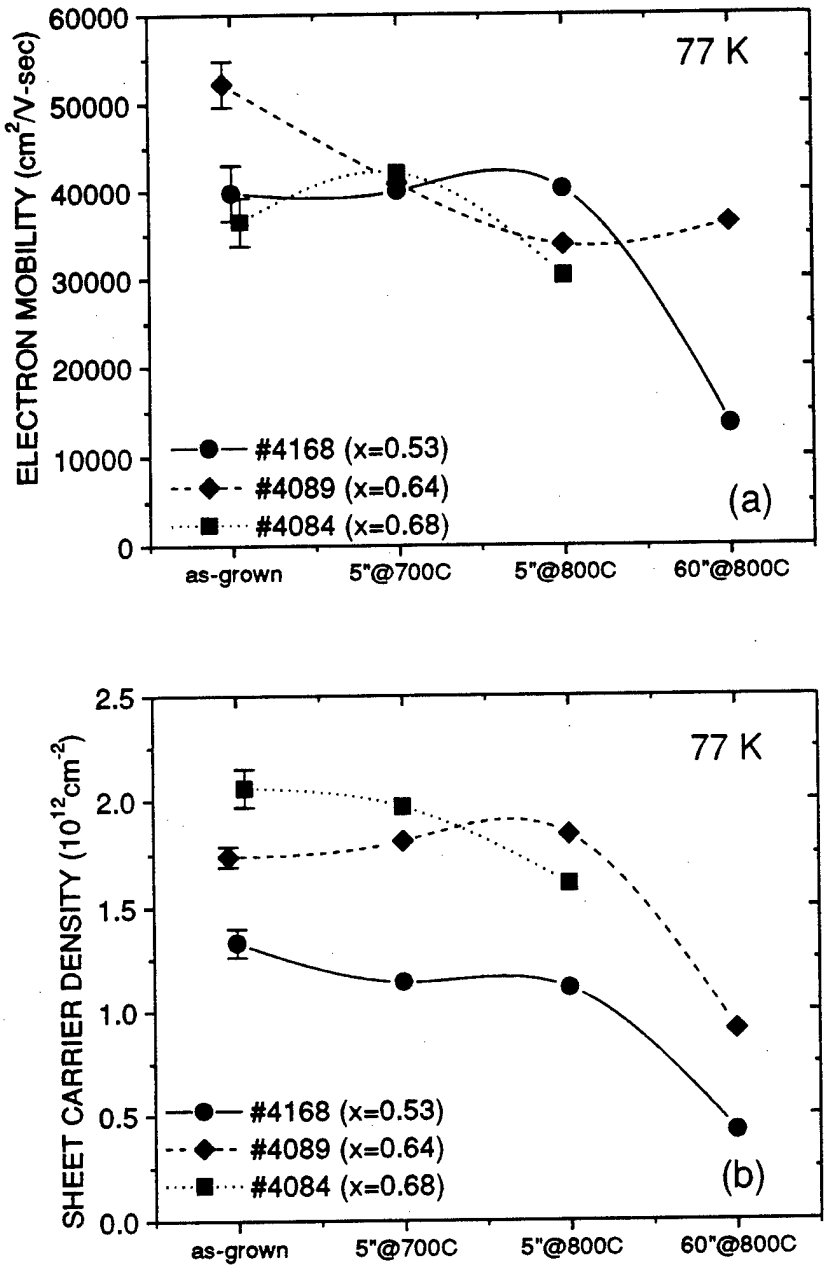

Figure 4-9: Electron mobility (a) and sheet carrier concentration (b) at 77 K as a function of annealing for MODFET heterostructures.

forming during the anneals, hence reducing the measured electron concentration.[117]

For sample 4084, μ_{300K} was essentially unchanged by 5" anneals at 700 and 800°C. For the same anneals, sample 4089 exhibited decreases in μ_{300K}. After 60" at 800°C, however, μ_{300K} = 10,300 cm^2/V-sec, about the same as the pre-anneal values. Also, we note that $n_{S,300K}$ was largest (2.3 $\times 10^{12}$/cm^2) for the 4089 sample with the lowest mobility, 5" at 800°C. In fact, for the three MODFET structures described here as well as all others that we grew, μ_{300K} was always less than 7500 cm^2/V-sec when $n_{S,300K}$ was greater than 2.1 $\times 10^{12}$/cm^2. This suggests that the variations in room-temperature mobility for 4089 are the result of wafer nonuniformities, not annealing.

The 77K mobility of both 4084 and 4089 dropped after 5" at 800°C, while the lattice-matched sample, 4168, was not affected. After 60" at 800°C the 77K mobility of 4089 dropped from 52,000 to 36,000 cm^2/V-sec, whereas the 300K mobility was apparently unchanged. We believe that the 77K drop is real, not a result of nonuniformity.[‡] After 60" at 800°C, μ_{77K} for 4168 dropped from 40,000 to 13,500 cm^2/V-sec, a much larger decrease than 4089 exhibited. A likely cause of the drop in mobility is Si diffusion into the channel. It is not clear why the effect is larger for the lattice matched structure.

In summary, the room-temperature mobility of our pseudomorphic MODFETs is not affected by anneals up to at least 60" at 800°C. The 77K mobility is more sensitive and decreases after 800°C anneals. Decreases in μ_{77K} also occur for a lattice-matched MODFET, suggesting that interdiffusion may be responsible. We conclude that significant lattice relaxation is not occuring during annealing. These results suggest that our high-quality epilayers beyond the Matthews-Blakeslee critical thickness are thermally stable and suitable for use in devices such as FETs.

[‡]A study of pseudomorphic InGaAs/InAlAs MODFETs (without annealing) also found that degradation in mobility appeared first at 77K and then at 300K.[69]

4.3 Relaxation Kinetics

Research on a variety of semiconductors including III-V compounds has demonstrated that relaxation processes are governed by both thermodynamic and kinetic constraints. The Matthews-Blakeslee theory discussed in chapter 1 and appendix C only considers thermodynamics: if the lowest (equilibrium) energy state of a heterostructure includes misfit dislocations, the layer is said to exceed the critical layer thickness. In MBE, however, layer growth occurs under conditions which are far from equilibrium, resulting in metastable structures. The degree of relaxation may be a function of the nucleation and growth of misfit dislocations.

Several theories have been proposed to explain the relaxation kinetics of strained layers. Intuitively, relaxation should increase with increasing mismatch or thickness. In addition, since the kinetics of dislocation nucleation and growth are involved, both time and temperature will be factors. If one is modeling the relaxation during growth, the time required to grow the layer and the growth temperature are the relevant parameters. One can also model the relaxation during post-growth annealing. In that case, the temperature and duration of the anneal are the appropriate parameters.

At this point, it is probably fair to say that none of the relaxation kinetics theories is widely accepted.[17,18,118,119] The theory by Dodson and Tsao[16,120] has shown some success in applications to SiGe/Si[65,121] and InGaAs/GaAs[64] heterostructures. We will briefly outline their model and apply it to our data.

Dodson and Tsao's model, in part based upon the earlier work of Alexander and Haasen,[122] considers both the kinetics of dislocation formation and the increase in dislocation density caused by dislocation multiplication. The result is a differential equation for $\gamma(t)$, the strain relief:

$$\frac{d\gamma}{dt} = D[\left(\frac{\Delta a}{a}\right)_r - \gamma(t) - r(h)]^2[\gamma(t) + \gamma_o] \tag{4.1}$$

where D is a phenomenological parameter describing dislocation mobility and multiplication and γ_o represents a source term for misfit dislocations; both D and γ_o are

"adjustable parameters."[§] The function r(h) is the homogeneous strain retained by the overlayer, given by:

$$r(h) = \frac{b(1 - \nu cos^2\alpha)\ln(4h/b)}{h4\pi(1+\nu)} \tag{4.2}$$

where h is the layer thickness, ν is Poisson's ratio, α is an angle describing the dislocation orientation (see appendix C), and b is the Burger's vector of the dislocations.

The strain relief in the Dodson-Tsao model, $\gamma(t)$, is equivalent to the parallel mismatch. Since orthorhombic distortion may be present, we have:

$$\gamma(t) = \frac{\left(\frac{\Delta a}{a}\right)_{\|[110]} + \left(\frac{\Delta a}{a}\right)_{\|[1\bar{1}0]}}{2} \tag{4.3}$$

We can also relate strain relief to the dislocation density by:[59]

$$\gamma(t) = \rho(t)b \tag{4.4}$$

where $\rho(t)$ is the linear density of misfit dislocations lying in the interface. We note that (4.4) is strictly valid only if misfit dislocations are the only defects relieving layer strain. Strain may also be relieved by defects such as stacking faults and edge dislocations which often result from three-dimensional growth (see chapters 1 and 6).

Previous work in the InGaAs/GaAs system suggests that the parameter D in the Dodson-Tsao model may be a function of lattice mismatch.[64] Thus, we apply the model to sets of samples with constant composition (mismatch) and varying thickness (see fig. 2.19 for our complete set of relaxation data). We begin with a set of four InGaAs samples with $(\Delta a/a)_r = +0.010$. We used the Runga-Kutta method of order 4 to numerically integrate the differential equation, (4.1). We adjusted D and γ_o until a reasonable fit to the experimental data was achieved. The fit was obtained with $D = 70$ sec^{-1} and $\gamma_o = 1 \times 10^{-3}$.[¶] The data and model fit are shown in fig.

[§]Our D is equivalent to Dodson and Tsao's "$C\mu^2$" where μ is the shear modulus. We note that the correct form of r(h) is given in Dodson and Tsao's erratum. However, the equation equivalent to our (4.1) apparently has a sign error in the erratum but is correct in the original paper.

[¶]In all cases, we use a t equal to the growth time plus 100 seconds to represent the cool-down period after growth. The results are not very sensitive to the t that is used.

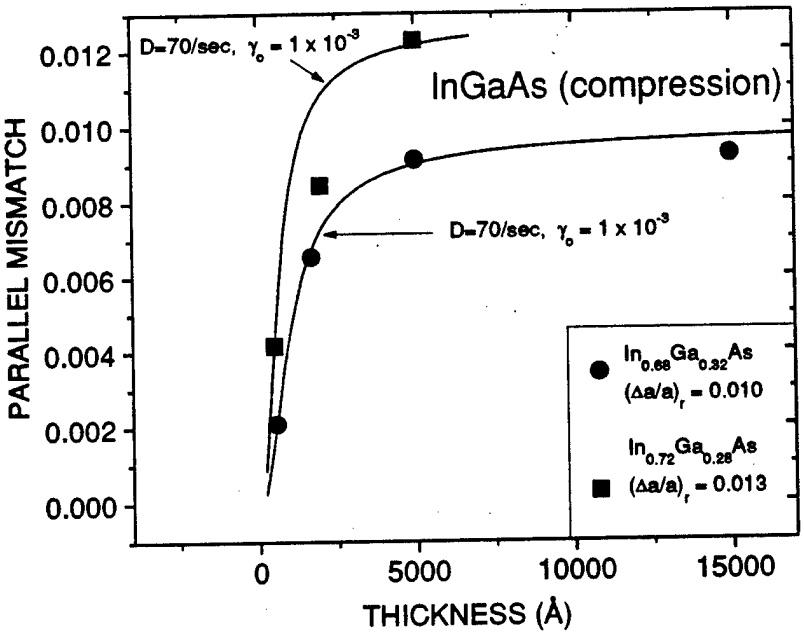

Figure 4-10: Parallel lattice mismatch as a function of layer thickness for two sets of InGaAs layers in compression. The solid lines are the predicted strain relief from the Dodson-Tsao model, eq. (4.1).

4.10. The fits are not very sensitive to the value of γ_o. We note that for a fixed D, relaxation decreases when γ_o increases, contrary to what one might expect for a dislocation source term. A second set of InGaAs in compression is also available for comparison. The relaxed lattice mismatch, 0.013, is larger than the previous set. We attempted to fit the data using the same values of D and γ_o. The predicted curve is a reasonable fit to the data, as shown in fig. 4.10.

We also used the Dodson-Tsao model to fit sets of InGaAs in tension (fig. 4.11) and InAlAs in compression (fig. 4.12), using D's of 55 and 70 sec^{-1}, respectively. We note that these values of D are within a factor of 1.5 of the SiGe results of Dodson and Tsao.[120] We were unable to fit the 10,000 Å data point in fig. 4.12. This is the sample with $\bar{R} = 114\%$. The model will never predict a relaxation greater than 100%.

In the case of InAlAs in tension, a 10,000 Å layer with a mismatch of -0.0066 is only 32% relaxed. In order to obtain a reasonable fit to this data set (fig. 4.13), we had to use a very small value of D, 0.05 sec^{-1}. This suggests that the relaxation mechanism is much different than the other three cases. We will return to this issue

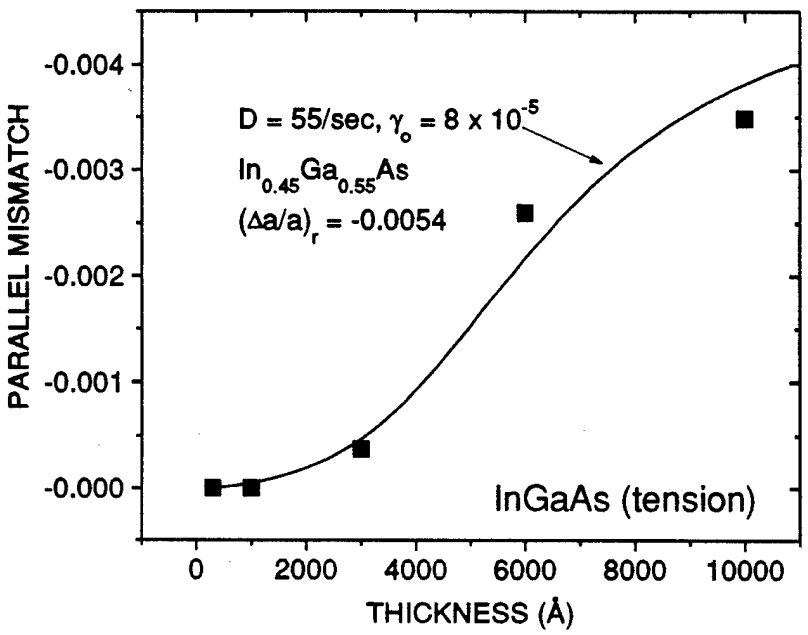

Figure 4-11: Parallel lattice mismatch as a function of layer thickness for InGaAs layers in tension. The solid line is the predicted strain relief from the Dodson-Tsao model, eq. (4.1).

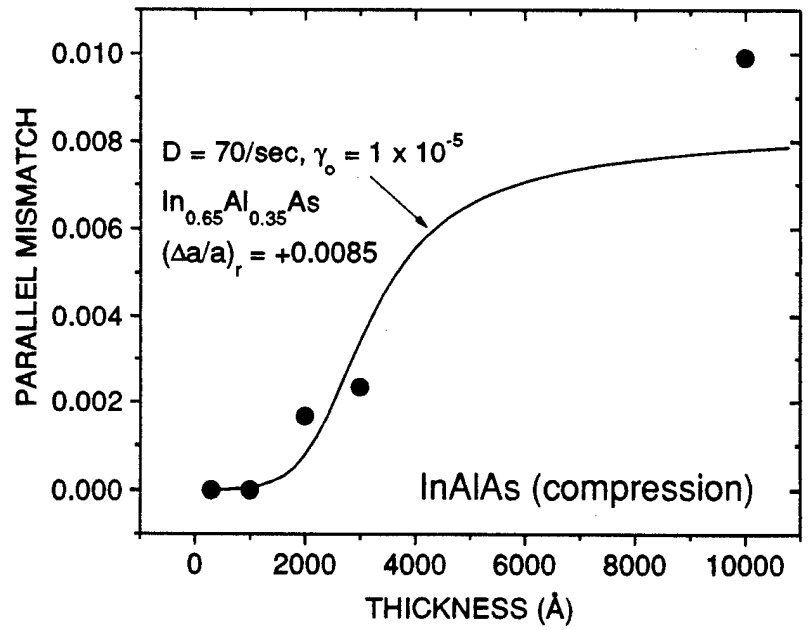

Figure 4-12: Parallel lattice mismatch as a function of layer thickness for InAlAs layers in compression. The solid line is the predicted strain relief from the Dodson-Tsao model, eq. (4.1).

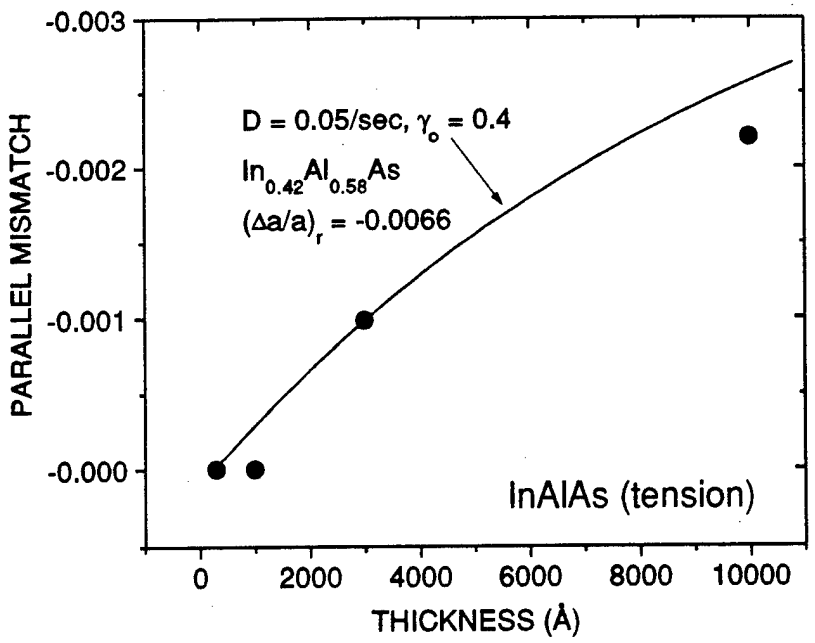

Figure 4-13: Parallel lattice mismatch as a function of layer thickness for InAlAs layers in tension. The solid line is the predicted strain relief from the Dodson-Tsao model, eq. (4.1).

in chapter 6.

We now consider the results of our annealing experiments. In sections 4.1 and 4.2, we demonstrated the thermal stability of high-quality InGaAs and InAlAs layers beyond the Matthews-Blakeslee (equilibrium) critical layer thickness. The fundamental question is: *If the layers are metastable, why is no relaxation observed for high-temperature anneals?*

In order for relaxation to occur, a source of misfit dislocations is required. One potential source is threading dislocations from the substrate. These threading dislocations can bend into misfit dislocations at the epilayer/substrate interface, as illustrated in fig. 4.14. Our InP wafers are guaranteed to have less than $5 \times 10^4/\text{cm}^2$ threading dislocations. As an order-of-magnitude calculation, we assume $2 \times 10^4/\text{cm}^2$ threading dislocations and consider a 1 cm by 1 cm sample. We also assume all the threading dislocations are bent into misfit dislocations and propagate to an edge of the sample. With these assumptions, the average length of a misfit dislocation is 0.5 cm and the linear density, ρ, is 5000/cm or $0.5/\mu$m. Using (4.4), we obtain $(\Delta a/a)_{||}$

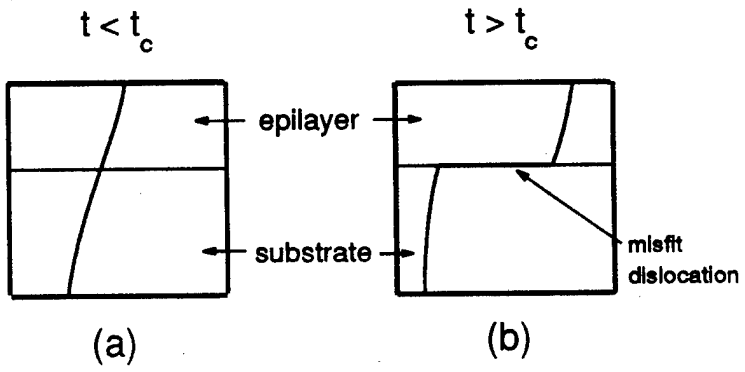

Figure 4-14: Behavior of substrate threading dislocations in strained-layer epitaxy. For layers below the critical thickness, threading dislocations propagate to the surface (a). For layers above the critical thickness, a misfit dislocation segment may form at the interface (b).

$= 2 \times 10^{-4}$ which is about the sensitivity limit of HRXRD, but is a factor of 30-60 smaller than the mismatch for the samples we annealed. We conclude that threading dislocations do not provide a sufficient source of misfit dislocations to substantially relax our strained layers.

Misfit dislocation segments can also be formed from half-loops propagating from the epilayer surface. These half-loops must overcome an energy barrier to nucleate. The energetics of half-loop nucleation was considered by Fitzgerald *et al.*[22] for the case of InGaAs on GaAs and Kamat and Hirth[123] for GaAs on other materials. We will apply the procedure of Fitzgerald to InGaAs/InP and InAlAs/InP heterostructures.

The change in energy due to the formation of a semicircular loop is:[22]

$$E = \frac{Gbr}{8(1-\nu)}\left[b(2-\nu)ln(\frac{8C_E r}{e^2 b}) - 8\pi r(\Delta a/a)_r(1+\nu)cos\lambda cos\phi - 2b(1-\nu)sin\alpha\right] \tag{4.5}$$

where r is the loop radius, C_E is the core energy factor, and the other parameters were

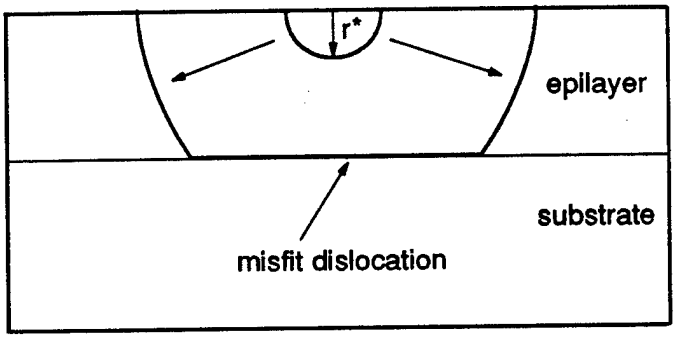

Figure 4-15: Formation of a misfit dislocation from a dislocation half-loop. The critical radius of the half-loop is r^*.

previously defined. We maximize this energy to obtain r^*, the critical loop radius for surface nucleation. The result is:

$$r^* = \frac{b(2-\nu)\left[\ln(8C_E r^*/e^2 b)+1\right] - 2b(1-\nu)sin\alpha}{16\pi(\Delta a/a)_r(1+\nu)cos\lambda cos\phi} \tag{4.6}$$

The energy of the system will be at a maximum if $r = r^*$. Hence, if a loop has sufficient energy to reach r^*, it can then spontaneously grow until it reaches the interface and forms a misfit dislocation as illustrated in fig. 4.15.

We solved (4.6) using Newton's method, assuming $C_E = 4$,[113] $\lambda = \alpha = 60^o$, and $\phi = 35.26^o$.[22] Other values were interpolated from appendix B. The result for InGaAs/InP is plotted in fig. 4.16a. As the magnitude of the mismatch increases, the size of the critical radius decreases. Using the calculated values of r^*, we can determine the critical energy, E^*, from (4.5). The result is shown in fig. 4.16b. As lattice mismatch increases, E^* decreases. In other words, homogeneous nucleation is more likely in highly strained systems. This makes physical sense because the amount of elastic energy released by a half-loop is proportional to the strain. The results for InAlAs, fig. 4.17, are similar. The critical energy for AlAs is higher than for InAs or GaAs

primarily because AlAs has a larger shear modulus.

We now consider the energy available for the nucleation of surface loops. Estimates for the energy available during growth are 50kT[124] and 88kT.[113] We assume that energy available during annealing is given by the same expressions. Using 88 kT and our maximum annealing temperature of 1123K, we obtain 8.6 eV. From figs. 4.16 and 4.17, the energy required for loop nucleation is always at least 25 eV. For the compositions used in our annealing experiments, E^* is 100-500 eV. We conclude that sufficient energy is not available for the homogeneous nucleation[‖] of surface half-loops during anneals.

Our findings are consistent with those of Fitzgerald *et al.*[22] and Kamat and Hirth.[123] Fitzgerald estimated that a mismatch of about 5% is required for half-loop nucleation during the growth of InGaAs on GaAs at 550°C. Kamat and Hirth calculated that a mismatch of at least 9% is required for homogeneous nucleation on a GaAs surface at 730°C.

4.4 Summary

In summary, we have shown that significant relaxation of InGaAs and InAlAs layers occurs during growth when the mismatch and thickness are relatively large. Layer thicknesses of 50-100 times $t_{c,MB}$ are required to achieve almost complete strain relaxation.

We examined the thermal stability and relaxation kinetics of strained layers. For a fixed mismatch, the degree of relaxation during growth can be fit by the kinetic model of Dodson and Tsao, although adjustable parameters are required. Using HRXRD, we observe additional relaxation when partially relaxed InGaAs layers are annealed. High-quality (unrelaxed) InGaAs and InAlAs layers with $t/t_{c,MB}$ = 3-9 do not exhibit relaxation during anneals up to 850°C. In addition, the room-temperature mobility of InGaAs/InAlAs MODFET heterostructures with pseudomorphic channels is not

[‖]Following the convention in the literature, we use the term *homogeneous nucleation* to refer to the nucleation of a dislocation half-loop on a defect- and particulate-free epilayer surface.

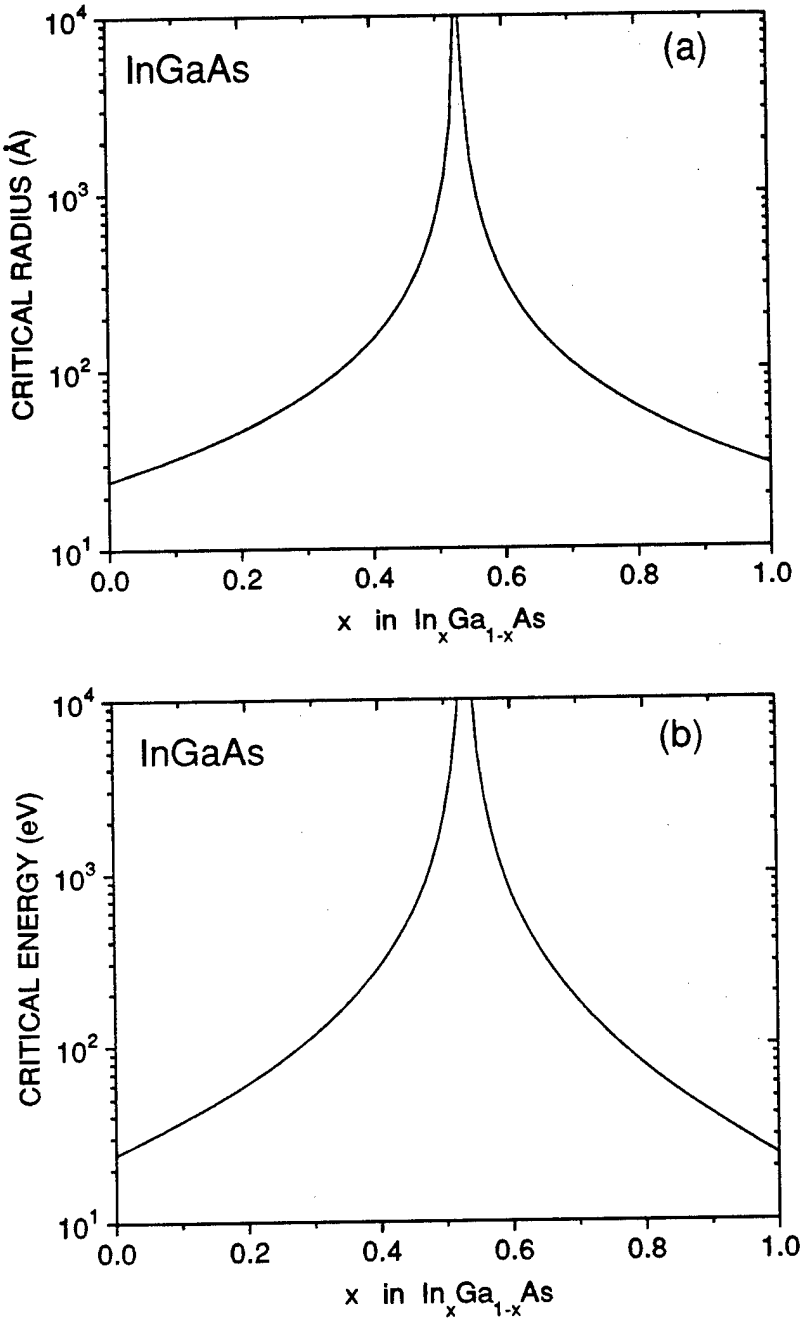

Figure 4-16: Critical radius (a) and energy (b) for homogeneous nucleation of dislocation half-loops in InGaAs.

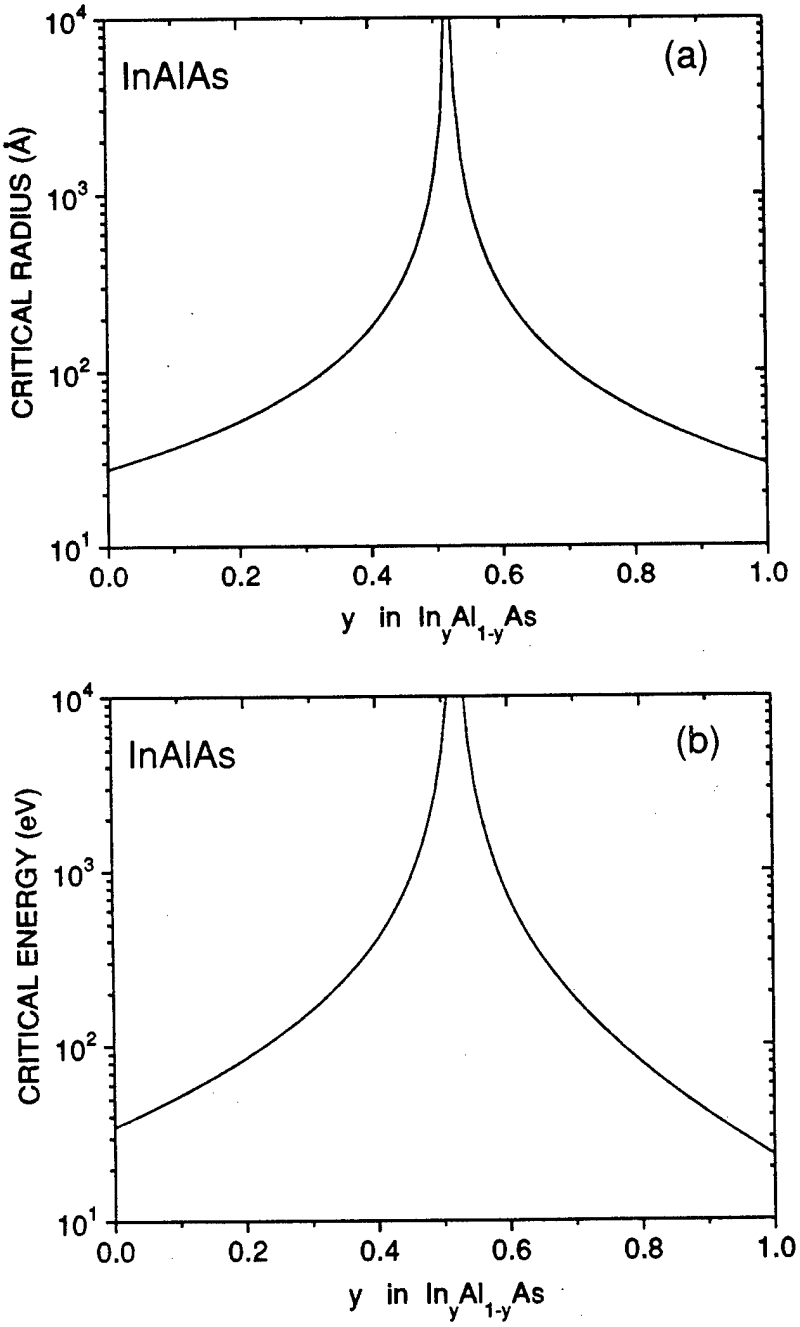

Figure 4-17: Critical radius (a) and energy (b) for homogeneous nucleation of dislocation half-loops in InAlAs.

affected by anneals up to 800°C. Degradation in the 77K mobility is observed, but is also present in a lattice matched MODFET. This suggests that interdiffusion, not relaxation, is the primary cause. We explain the thermal stability of our epilayers by the lack of sufficient energy to homogeneously nucleate half-loop dislocations and the absence of a sufficient number of threading dislocations in the substrate.

Chapter 5

Device Application: Heterostructure Field-Effect Transistors

The critical layer thickness of Matthews and Blakeslee, $t_{c,MB}$, is often used as an upper limit in the design of pseudomorphic device heterostructures.[2] As we showed in chapter 2, however, complete lattice relaxation does not abruptly occur when an InGaAs or InAlAs layer reaches $t_{c,MB}$. In fact, layers often retain high crystalline quality up to thicknesses several times $t_{c,MB}$. Such layers are thermally stable to temperatures of at least 800°C (chapter 4). These results suggest that layers thicker than $t_{c,MB}$ may be suitable for some device applications.

We fabricated heterostructure field effect transistors (HFETs) in the InAlAs/ InGaAs/InP materials system. In this chapter, we present both the HRXRD and device results for an HFET in which one layer exceeds $t_{c,MB}$. We also illustrate how HRXRD can be used to determine which samples should be processed into devices. Finally, we compile data from the literature for HFETs with strained InGaAs and InAlAs layers, and compare it to $t_{c,MB}$ and our HRXRD results.

50Å	$In_{0.53}Ga_{0.47}As$	cap
300Å	$In_{yi}Al_{1-yi}As$	insulator
100Å	n^+ $In_xGa_{1-x}As$	channel
75Å	$In_{0.53}Ga_{0.47}As$	subchannel
1000Å	$In_{yb}Al_{1-yb}As$	buffer
	(001) InP(Fe)	substrate

Figure 5-1: Cross-section of doped-channel InAlAs/InGaAs heterostructure field-effect transistor.

5.1 HFET Characterization by HRXRD

Our typical device structure is shown in fig. 5.1 and consists of (bottom to top): semi-insulating (001) InP(Fe) substrate, 1000 Å InAlAs buffer, 75 Å InGaAs sub-channel, 100 Å Si-doped n^+-InGaAs channel, 300 Å InAlAs pseudo-insulator, and 50 Å InGaAs cap. We note that unlike a MODFET, the dopants are located in the channel in our device. This results in lower channel mobility. However, these devices typically operate in the velocity saturation regime, and saturation velocity is not very sensitive to doping.[125] The doped-channel approach offers several advantages over MODFETs including higher breakdown voltage and lack of transconductance collapse.[126]

In the past, doped-channel HFETs were fabricated using lattice-matched layers of InGaAs and InAlAs on InP.[126] There are, however, advantages to using strained layers. Drain current, transconductance, and cutoff frequency can be increased by employing InAs-rich InGaAs channels.[127] If AlAs-rich insulating layers are used, the band-gap

of the InAlAs and the conduction band offset between the InGaAs and InAlAs are increased. This reduces hot-electron effects, improves electron confinement in the channel, and increases the breakdown voltage of the device.[85,128]

Both the channel and insulator were intentionally strained in HFET 1870. The channel was nominally doped to $6 \times 10^{18}/\text{cm}^3$. Hall/van der Pauw measurements yield a sheet carrier density of $2.1 \times 10^{12}/\text{cm}^2$ and an electron mobility of 3660 cm^2/V-sec at room temperature.

The (004) HRXRD scan of 1870 is shown in fig. 5.2. We simulated the structure using the nominal layer thicknesses (which we believe are accurate to within 10%) and adjusting the compositions to obtain a good match with the experimental data. The best-fit simulated rocking curve is shown as curve b) in fig. 5.2. The buffer is the thickest layer and hence gives the peak with the largest intensity and narrowest width (except for the InP substrate). We see that the composition of the buffer, $y_b = 0.506$, is close to the lattice-matched value, 0.521. The 300 Å insulator layer also gives a distinct but broader peak, with $y_i = 0.411$. The 100 Å channel, 75 Å subchannel, and 50 Å cap are too thin to produce distinct peaks (see section 2.4). The structure in the $\Delta\theta$ = -2000 to -200 arc-sec range is primarily caused by the nominally x=0.65 channel, but we cannot obtain an accurate measure of x from this sample. To demonstrate the sensitivity of HRXRD to the buffer and insulator compositions, we simulated a structure in which the buffer and insulator have InAs mole fractions which are 0.005 and 0.010 less than the best-fit values. The result is shown as curve c) in fig. 5.2. Clearly, changes in composition of this size can be detected by HRXRD.

The InAlAs pseudoinsulator layer in sample 1870 is a factor of 2.0 thicker than $t_{c,MB}$. The experimental FWHM of this layer is 520 arc-sec, compared to 500 arc-sec for the simulation.[63] This good agreement, along with the presence of Pendellosung fringes in the experimental curve, indicates a coherent heterostructure. The 100 Å $In_{0.65}Ga_{0.35}As$ channel is thinner than $t_{c,MB}$. Based upon our studies and the recent work of Gendry et al.,[43,44] we believe that higher InAs mole fractions (or thicker layers) could be used in the channel without degradation from lattice relaxation or three-dimensional growth. The resulting devices would be expected to have higher

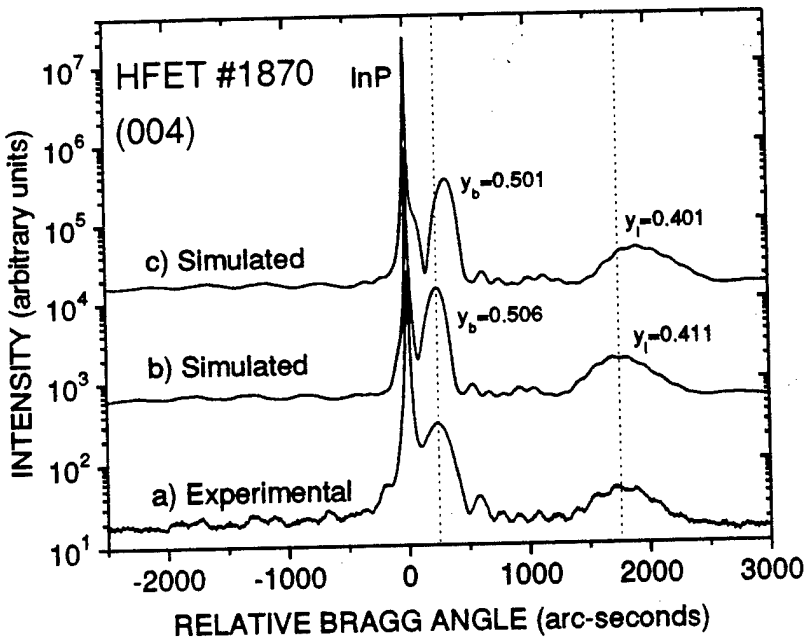

Figure 5-2: Experimental HRXRD rocking curve for HFET 1870; peaks from the InAlAs buffer and pseudo-insulator layers are visible. b) Best-fit simulation using structure of fig. 5.1. c) Simulation of heterostructure with different buffer and pseudo-insulator compositions.

transconductance but lower breakdown voltage than 1870.

5.2 Device Characteristics

The ultimate test of a strained-layer heterostructure is its device characteristics. In summary, devices† on sample 1870 with a 1.9 μm gate length (L_g) and a 200 μm gate width have a peak transconductance of 190 mS/mm, a maximum drain current of 302 mA/mm, and a power density of 0.40 W/mm.[129,130] The output I-V characteristics are shown in fig. 5.3. The device exhibits complete channel pinch-off and a breakdown voltage of 14 V.

The unity current gain cut-off frequency, f_t, and unity power gain cut-off frequency, f_{max}, are plotted as a function of gate-source voltage in fig. 5.4. The maximum values are: f_t = 15 GHz and f_{max} = 101 GHz. For this device, we calculate an electon velocity of 1.8 x 10^7 cm/sec and an $f_t \times L_g$ product of 28 GHz-μm. These values are

†Device processing and testing was performed by Sandeep Bahl at MIT.

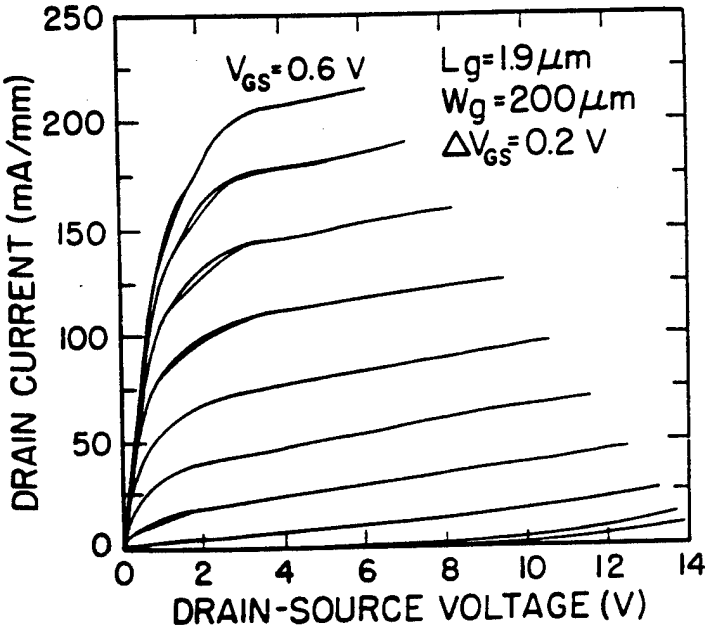

Figure 5-3: Output I-V characteristics for HFET 1870. The gate length was 1.9 μm and the gate width was 200 μm.

comparable to those obtained on lattice-matched MODFETs of similar gate length, but the power density and breakdown voltage of our device are 2-3 times higher.[131] We also measured device characteristics as a function of angular orientation on the surface and observed no asymmetries. The presence of asymmetries is an indication that misfit dislocations have formed.[85] We conclude that if dislocations are present in HFET 1870, their density is insufficient to degrade device performance in any appreciable way.

5.3 Heterostructure Evaluation

In addition to measuring layer composition, HRXRD can be used to determine which HFET structures should be processed into devices. As an example, we show the HRXRD rocking curves for two samples in fig. 5.5. Both samples have a structure similar to 1870 (fig. 5.1). For HFET 4164 (a), the nominal channel composition has been increased from x = 0.65 to x = 0.70. The channel is now clearly visible in the HRXRD scan. By comparison to simulations, we confirmed that x = 0.70 $\pm$ 0.02. In contrast, we do not observe distinct peaks for the channel, insulator, or buffer layers

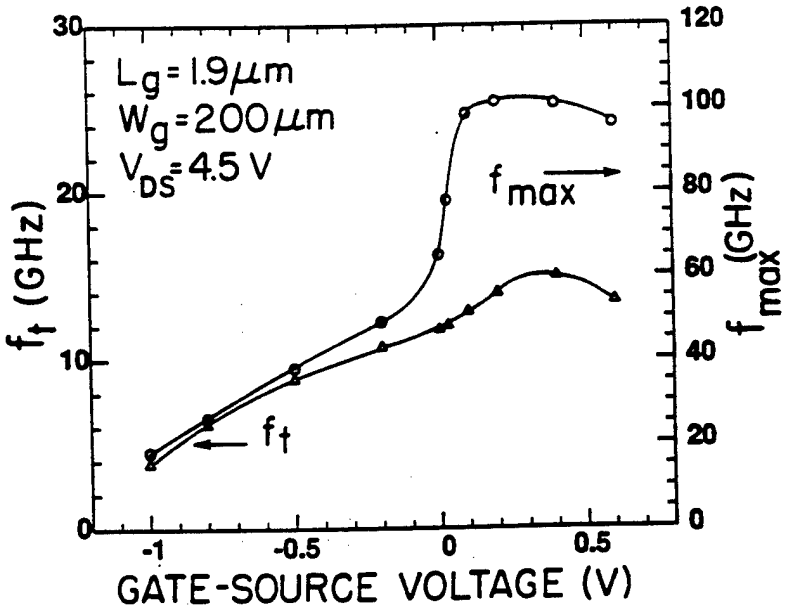

Figure 5-4: Unity current and power gain cut-off frequencies for HFET 1870. The drain-source voltage is fixed at 4.5 V.

of HFET 4143 (fig. 5.5b). The unintentional mismatch of the buffer layer normally produces a distinct peak. Since it is the first layer, the absence of a buffer layer peak for sample 4143 suggests that something went wrong with the growth from the beginning. One possibility is that the growth temperature was too low and the native oxide was not completely desorbed. Based upon the HRXRD results, 4164 should be processed but 4143 should not. This conclusion is supported by mobility measurements. The room-temperature electron mobility of sample 4164 is 4110 cm^2/V-sec, about what one would expect for an InGaAs layer doped at $6 \times 10^{18}/cm^3$.[129,132] The mobility for sample 4143 is only 230 cm^2/V-sec, confirming that the sample is poor.

We have not observed clear differences in the HRXRD scans between "good" HFET ($\mu_{300K} \approx 4000$ cm^2/V-sec) and "mediocre" HFET ($\mu_{300K} \approx 2000$ cm^2/V-sec) heterostructures. We also note that our biggest problem in device growth has been achieving the desired doping level. Hence, we routinely perform both HRXRD and Hall/van der Pauw measurements on all device heterostructures. Each measurement can be completed in less than one hour. We use the results to determine which samples to process and to make appropriate adjustments to Ga, Al, and Si cell temperatures for the next growths.

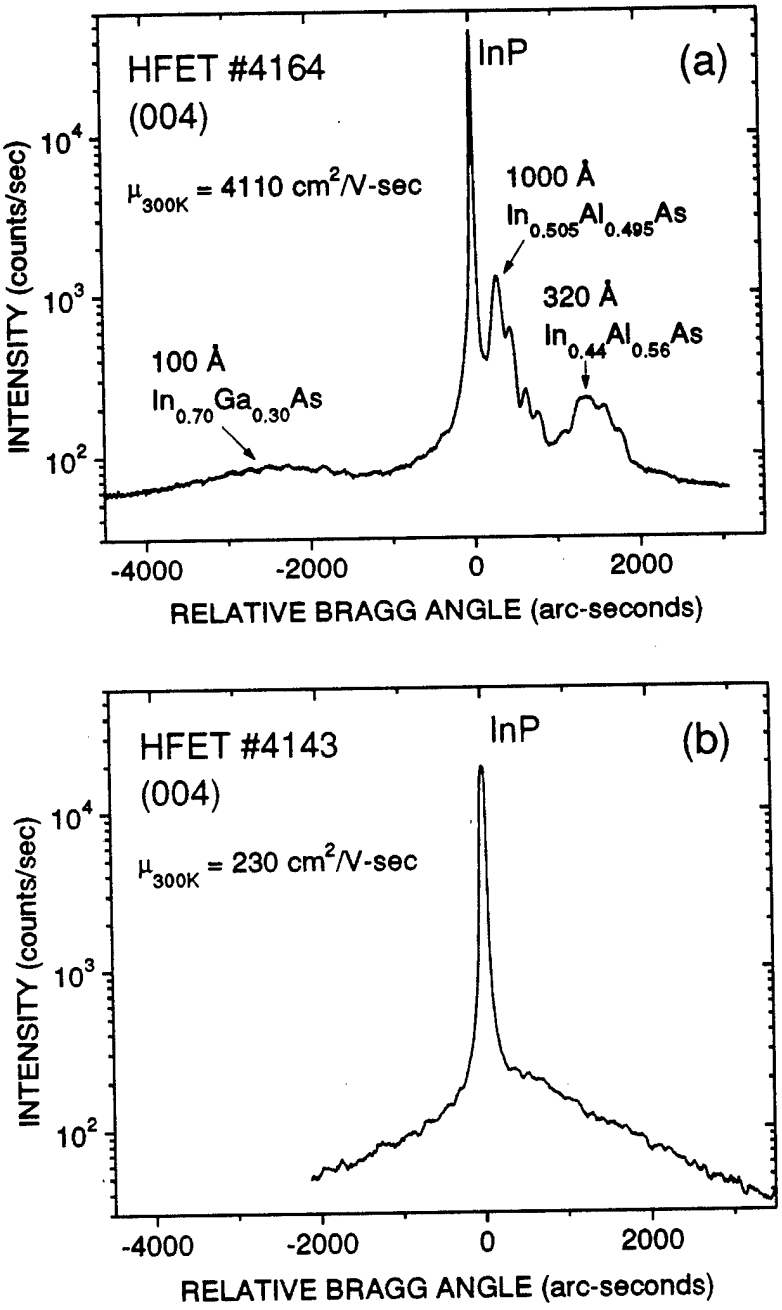

Figure 5-5: HRXRD rocking curves for HFETs with structures similar to fig. 5.1. Sample 4164 (a) exhibits distinct peaks for the buffer, insulator, and channel layers, but 4143 (b) does not.

5.4 Survey of Pseudomorphic $In_xGa_{1-x}As/In_yAl_{1-y}As/InP$ HFETs

Our results suggest that high-performance HFETs can include layers exceeding the Matthews-Blakeslee critical layer thickness. To confirm this finding, we surveyed the literature for HFETs using mismatched layers of either InAs-rich $In_xGa_{1-x}As$ or AlAs-rich $In_yAl_{1-y}As$ on InP.[11,69,70,127-129,133,134] In most reports, the channel thickness does not exceed $t_{c,MB}$, and, as expected, the devices show no sign of misfit dislocations. In some studies, however, devices were fabricated on a series of heterostructures with increasing mismatch, and a degradation in performance was observed when the mismatch was too large. In fig. 5.6 we plot layer thickness versus mismatch for InP-based HFETs with InGaAs (a) and InAlAs (b) strained layers. Closed symbols indicate device structures showing no signs of dislocations and open symbols represent degraded devices. Fig. 5.6 includes the calculated values of $t_{c,MB}$ (see Appendix C).

All the device results in fig. 5.6 suggest that HFETs can accomodate strained layers up to 2-4 times $t_{c,MB}$ without degradation. We also include lines showing estimates for the limit of high crystalline quality based upon our experimental HRXRD criteria from chapter 2 (FWHM ratio < 1.8). We observe reasonable agreement between the HRXRD results and the limited device data available. For mismatches greater than $\pm 1\%$ we use a dotted line because of our limited HRXRD data in that region.

In the InGaAs/GaAs system, a recent paper[10] reported high-performance metal-semiconductor field-effect transistors in which the InGaAs layers were 2 and 4 times $t_{c,MB}$. The author concluded that the mismatched layers are strain-relaxed because, "As the InGaAs layer grows thicker than the critical thickness, the surface lattice constant increases abruptly and becomes close to the bulk InGaAs lattice constant." Our works suggests an alternative interpretation: the InGaAs layers are primarily strained with a low density of misfit dislocations which is insufficient to appreciably degrade device performance.

As mentioned in chapter 1, Temkin *et al.*[12] examined the reverse-bias leakage

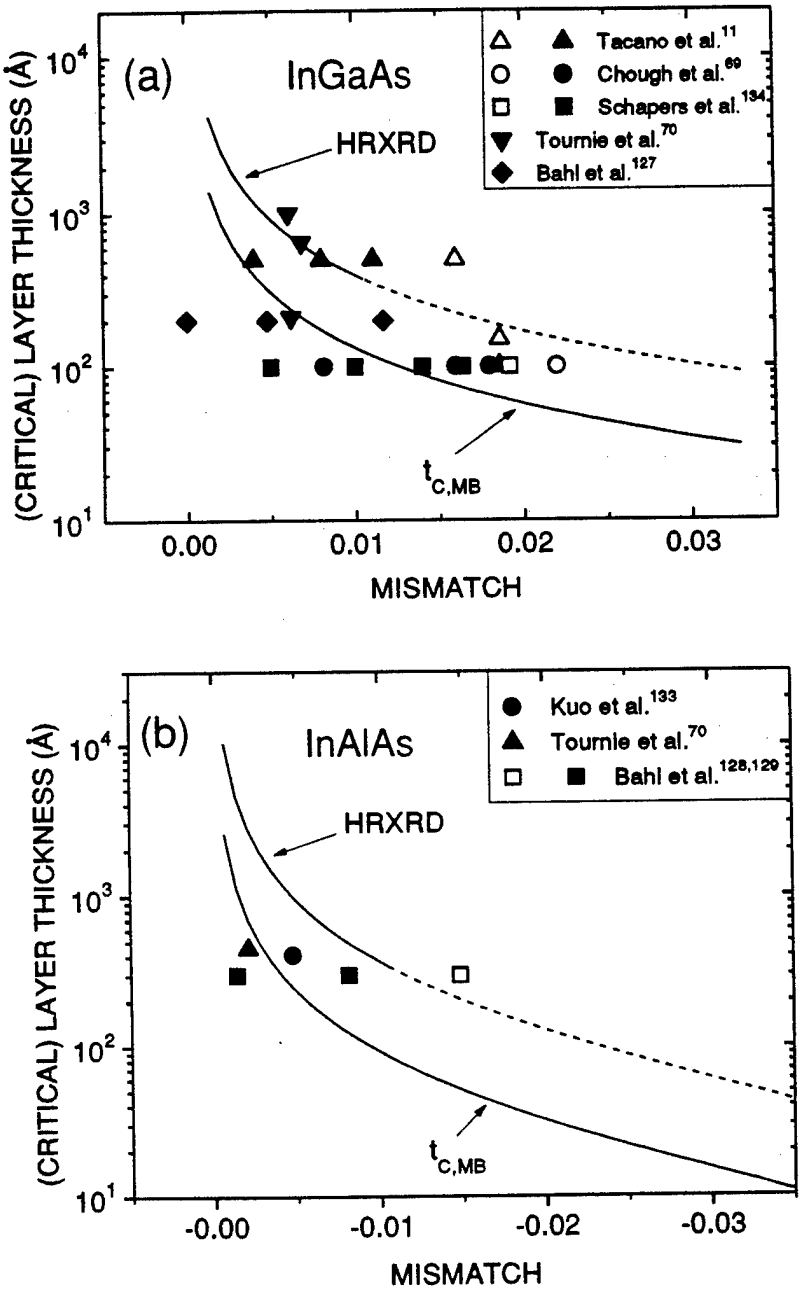

Figure 5-6: Layer thickness versus mismatch for InGaAs (a) and InAlAs (b). Symbols represent InAlAs/InGaAs HFET's with (open) and without (filled) signs of degradation due to mismatch. Estimates of critical thickness from the anisotropic extension of the Matthews-Blakeslee theory are shown as solid lines. We also include lines showing our HRXRD-based limit (FWHM ratio < 1.8) for high crystalline quality; the lines are dotted for mismatches greater than $\pm$ 1% because of our limited data in that region.

current in $In_xGa_{1-x}AsInP$ quantum-well p-i-n photodiodes and found an apparent critical thickness of 1.0-1.5 $t_{c,MB}$. Because of their larger mesa area, such structures may be more sensitive to misfit dislocations than HFETs. In general, the amount of strain which can be tolerated in a device heterostructure may depend upon the type of device. For example, a small density of misfit dislocations may not affect an HFET, but the same dislocation density in the active region of a laser could severely degrade its performance.

5.5 Summary

In summary, HRXRD experimental rocking curves combined with simulations can be used to determine the composition of epitaxial layers in device heterostructures. HRXRD also gives a qualitative measure of the material quality in a device structure. This information can be used to select samples for device processing. In chapter 2, we found that high crystalline quality, as measured by HRXRD, can be maintained to thicknesses beyond $t_{c,MB}$. In this chapter, we have used actual device measurements to demonstrate that layers thicker than $t_{c,MB}$ can be used in high-performance HFETs. Our device results are in general agreement with other reports for HFETs in the InAlAs/InGaAs/InP materials system.

Chapter 6

Discussion

In this chapter, we first consider the possibility that composition modulation may affect the crystalline quality and lattice relaxation in strained layers. We then explore the connection between heterogeneous dislocation nucleation, strain relief, thermal stability, and growth modes. We explain the thermal stability of our InGaAs/InP and InAlAs/InP pseudomorphic heterostructures as well as conflicting reports in the literature for the InGaAs/GaAs and SiGe/Si systems. Based upon our findings, we suggest procedures for the growth of high-quality, thermally-stable strained epilayers. In addition, we consider the cause of asymmetry in misfit dislocation density for our samples.

6.1 Composition Modulation

As discussed in section 1.5, others have observed composition modulation in both InGaAs and InAlAs layers. In chapter 3, we showed that composition modulation was in the wrong direction to account for the large optical anisotropy observed for many strained layers. Here, we will address the role of composition modulation in the crystalline quality and lattice relaxation of strained layers.

The period of composition modulation is typically a few hundred to a few thousand angstroms compared to our HRXRD spot size of about 1 x 2 mm. Hence, we expect the x-ray beam to sample many periods of oscillation. Substantial variations in lattice

parameter would clearly broaden the HRXRD layer peak.

We do not know of any measurements of the modulation amplitude for InAlAs or InGaAs. In the case of $In_xGa_{1-x}As_yP_{1-y}$, variations in x and y are as large as 0.1.[50] In such a quaternary system, the lattice parameter can remain constant as both x and y change. In our ternary layers, however, any change in composition also changes the lattice constant. Contrast modulation with a period of 365 Å was observed for sample 3099, 1000 Å of $In_{0.579}Al_{0.421}As$ (fig. 3.15). The HRXRD scan for 3099 (fig. 2.8) exhibited interference fringes and a FWHM ratio of 1.3. We speculate that the amplitude of the modulation in sample 3099 is very small ($\Delta y \ll 0.01$) and hence does not affect the HRXRD measurements.

In section 2.3, we observed that asymmetric broadening of the (004) HRXRD layer peaks occurs in some cases. The peak widths were a maximum in the [110] and $[\bar{1}\bar{1}0]$ directions and a minimum in the $[1\bar{1}0]$ and $[\bar{1}10]$ directions. The observed composition modulations are in the $< 100 >$-type directions.[51,52,106] Hence, composition modulation cannot explain the asymmetric peak broadening.

We have TEM micrographs for three samples with degraded crystalline quality: 1530 (fig. 3.16), 1880 (fig. 3.19) and 1486 (not shown). In each case, composition modulation is not visible. It is possible, however, that composition modulation is present but is obscured by the extreme surface roughness. Hence, we cannot completely rule out the possibility that composition modulation is a factor in HRXRD peak broadening and fringe loss for some samples.

Composition modulation can lower the total energy of a strained epitaxial layer.[48] Unlike crystalline defects such as misfit dislocations and stacking faults, however, it cannot relieve a significant amount of the lattice strain. Peiro *et al.*[51] investigated layers of $In_{0.54}Ga_{0.46}As$ on InP by TEM and HRXRD. For samples which were 1-2 $\times$ $t_{c,MB}$, they observed composition modulation, but no crystalline defects or lattice relaxation. Samples 3-7 $\times$ $t_{c,MB}$ exhibited composition modulation, high densities of stacking faults, and substantial lattice relaxation. Based upon these results and our measurements on sample 3099, we believe that composition modulation alone is not necessarily harmful to epitaxial layers. Composition modulation might influence the

point at which misfit dislocations, surface roughness, or 3-D growth begins.

Finally, we note that Yao *et al.*[41] used TEM to observe the transition from 2-D to 3-D growth in the InGaAs/GaAs system. They did not see any evidence of composition modulation. All the layers they investigated had a mismatch of at least 1%, compared to less than 0.1% for Peiro's InGaAs layers. This suggests that composition modulation may be more likely in systems with small mismatch because 3-D growth does not occur.

6.2 Heterogeneous Nucleation of Dislocations

In chapter 4, we demonstrated the thermal stability of high-quality InGaAs and InAlAs layers which exceeded the Matthews-Blakeslee critical layer thickness. We suggested that the layers were stable because of 1) an insufficient number of threading dislocations to bend into misfit dislocations and relieve strain and 2) insufficient thermal energy to homogeneously nucleate half-loop dislocations. We also showed an example from the literature in which a comparable SiGe layer relaxed substantially during annealing. Calculations show that even more thermal energy is required to homogeneously nucleate half-loops on SiGe than on InGaAs or InAlAs. Hence, homogeneous half-loop nucleation cannot explain the difference in thermal stability.

A survey of the SiGe literature reveals conflicting results for thermal stability with some layers relaxing during anneals of 600-800°C,[115,135-137] as illustrated in fig. 4.4, and others remaining stable to at least 800°C.[138,139] A few annealing experiments have also been reported in the InGaAs/GaAs system. Peercy *et al.*[20] observed a drastic reduction in photoluminescence intensity when device heterostructures with InGaAs layers thicker than $t_{c,MB}$ were annealed. Bertolet *et al.*[21] annealed similar samples and found no changes in the photoluminescence. Bertolet *et al.* point out that their structures were grown by MOCVD whereas Peercy *et al.* used MBE. They suggest that the MOCVD layers are more stable because of the higher growth temperature. Watson *et al.*[140] examined the stability of MBE- and MOCVD-grown InGaAs on patterned GaAs by counting dark-line defects imaged by cathodoluminescence. They

found the MOCVD layers to be much more stable, and attributed the difference to heterogeneous nucleation sources, with more sources available in the MBE layers.

Our growth temperatures were slightly lower than the temperatures used by Peercy *et al.*[20] (550°C) and Watson *et al.*[140] (520°C) for MBE-growth of InGaAs on GaAs. Our samples do not, however, show signs of relaxation during annealing.† Based upon this, we believe the growth temperature is not the primary factor determining thermal stability.

Differences in heterogeneous nucleation sources can explain our data as well as the InGaAs/GaAs and SiGe/Si results. Apparently, our samples did not have a sufficient number of sources to nucleate half loops to relieve strain and degrade the HRXRD rocking curves and electron mobility. Since our samples were grown by MBE, we conclude there is nothing inherent in the MBE process which causes high densities of nucleation sources.

We now consider the origin of the heterogeneous dislocation sources. Dodson[141] suggests that dislocation half-loops will be generated to relieve any local stress concentration. The stress concentrations could result from *clusters of impurities* such as oxygen, nitrogen, or carbon. Eaglesham identified *"diamond defects"* as a heterogeneous, regenerative nucleation source in SiGe films. These defects are produced by the dissociation of stacking faults.[142] Another possible source of nucleation sites is *oval defects* which are thought to be caused by Ga-spitting (in MBE) and particulates on the surface.[143,144] This suggests that sample preparation, transfer, and outgassing may influence the stability of strained layers. Our use of epi-ready substrates without additional cleaning (see appendix A) could be important.

Point defects might also be a significant source of misfit dislocations. In the case of intentionally doped layers, the dopant atoms themselves are probably the most abundant source of point defects. Watson *et al.*[140] noted that their layers were n-type, with sulfur as the dopant in the MOCVD material and silicon in the MBE layers. They suggest that the Si atoms might be better nucleation sources. In the

†We are using different characterization techniques than Watson and Peercy, but the post-annealing dislocation densities on MBE-grown samples observed by Watson are much larger than the detection limit for our HRXRD measurements.

case of the MODFETs we annealed, the Si atoms were in the lattice-matched InAlAs, not the mismatched channel. Hence, Si should not play a role unless it diffused into the channel. The strained layers in samples 1879 (fig. 4.5) and 1682 (fig. 4.6), however, were intentionally Si-doped, with nominal concentrations of $2\times10^{17}/cm^3$ and $6 \times 10^{17}/cm^3$, respectively. These samples did not relax during anneals up to 850°C. We conclude that substitutional Si atoms are not an efficient source of nucleation sites at these concentrations.

6.3 Asymmetries in Misfit Dislocation Density

In chapter 2, we used two HRXRD techniques to demonstrate asymmetric lattice relaxation in both InGaAs and InAlAs in compression or tension. We are now in a position to explain the asymmetries. Fox and Jesser performed a detailed analysis of dislocation asymmetries in MOCVD-grown $GaAs_{0.95}P_{0.05}$ on GaAs.[145] They considered four possible sources: substrate misorientation, thickness gradients, differences in nucleation energies, and differences in Peierls barriers. We will evaluate each of these sources for our samples.

1) **Substrate Misorientation:** All of our substrates were guaranteed to be within 0.5° of the (001) orientation. It seems unlikely that such small misorientations could cause substantial asymmetries. Furthermore, we have observed the same asymmetry pattern on substrates from many different InP boules. If we assume that the misorientations are randomly distributed in direction, the asymmetry patterns should vary from one substrate to another. We conclude that substrate misorientation is not the cause of the observed asymmetries.

2) **Thickness Gradient:** Unlike the MOCVD layers of Fox and Jesser, our MBE layers do not have significant thickness gradients. Hence, we rule this out as a cause of asymmetries.

3) **Nucleation Energy:** Dislocations along the [110] and [1$\bar{1}$0] directions in zinc-blende semiconductors have different dislocation cores. Abrahams *et al.* illustrated the difference and we show their drawing as fig. 6.1.[77] In case b) of fig. 6.1, the core

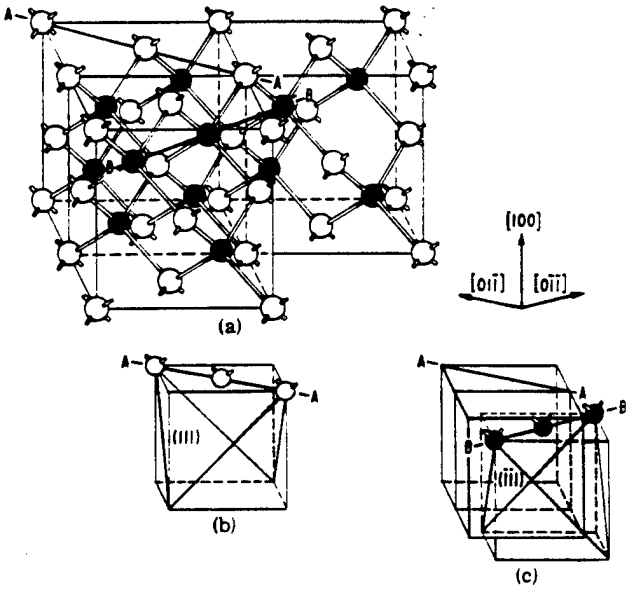

Figure 6-1: a) Atom positions in three unit cells of the zinc-blende structure. Atoms labelled **A** represent In, Ga, or Al in our materials. Atoms labelled **B** represent As. b) Core of 60° dislocation parallel to $[01\bar{1}]$; the slip plane is (111). c) Core of 60° dislocation parallel to $[0\bar{1}\bar{1}]$; the slip plane is $(\bar{1}\bar{1}1)$. (figure from Abrahams *et al.*[77])

of the 60° dislocation is parallel to the $[01\bar{1}]$ direction; in c), it is parallel to $[0\bar{1}\bar{1}]$. The dislocation motion occurs on the group III or group V glide set of planes. Since the dislocation cores are different, we expect different energy barriers for the two types of dislocations.

Fox and Jesser argued that in their samples, sufficient threading dislocations were present to account for the observed misfit dislocations. Hence, nucleation of additional dislocations was not required. As we showed above and in chapter 4, nucleation of half-loops is necessary to substantially relax our layers. Thus, we cannot rule out the possibility that differences in nucleation energy contribute to the orthorhombic distortion shown in fig. 2.20.

4) **Peierls Barriers:** Based upon the influence of doping on the dislocation asymmetries, observations of dislocation motion in bulk GaAs, and the elimination of the other three sources, Fox and Jesser concluded that differences in Peierls barriers were responsible for the asymmetries in misfit dislocation density. We have TEM images of InGaAs in tension (fig. 3.16) and InAlAs in tension (not shown) which reveal misfit dislocations along the $[1\bar{1}0]$ direction only, with an average spacing of

about 1 μm. These relatively low densities of misfit dislocations can be attributed to threading dislocations. Hence, the Fox-Jesser analysis applies for samples with low dislocation densities and negligible relaxation. Differences in the Peierls barriers could be responsible for the observed asymmetry in such samples.

The preferred direction for dislocations is consistent in our TEM and HRXRD measurements. Assuming a difference in Peierls barriers exists to account for the asymmetries in the samples with a low dislocation density, the difference in barriers should also be present in the layers which have substantially relaxed, presumably from heterogeneous nucleation of dislocation half-loops. Hence, the Peierls barrier differences could also cause asymmetries at high dislocation densities. Differences in nucleation energy may also contribute to the asymmetry.

6.4 Surface Roughness and Relaxation

We have proposed that heterogeneous nucleation sources are required for substantial lattice relaxation. We explained the thermal stability of our high-crystalline-quality strained layers by the lack of these sources in our MBE process. We also observed significant lattice relaxation in many as-grown samples (fig. 2.19). This raises the question: *What is the dislocation source for the relaxed epilayers?*

In chapter 3, we observed large optical anisotropies before the onset of significant relaxation in most cases. We attributed the optical anisotropies to surface roughness, possibly associated with 3-D growth. HRXRD and TEM results suggest that this roughness results in the initial loss of Pendellosung fringes and broadening of the layer peak, although misfit dislocations are probably a factor as well. We propose that the roughness provides a source of crystalline imperfections which serve as sites for subsequent heterogeneous nucleation of misfit dislocations during growth or annealing. This model is supported by the work of Guha *et al.*[35] who found that large numbers of defects are introduced at the boundaries between islands. We observed a high density of stacking faults in plan-view TEM of sample 1486 (not shown), a 6000 Å layer of $In_{0.460}Ga_{0.540}As$ with $\bar{R} = 52\%$. These stacking faults relieve strain and

may also serve as a source of diamond defects, as suggested by Eaglesham *et al.*[142]

Based upon the as-grown characteristics of epilayers and their thermal stability, we propose classifying layers into four categories. We show the regions on a plot of thickness versus composition for InGaAs/InP in fig. 6.2. In region I, the layers grow in a 2-D mode with no misfit dislocations and hence no relaxation (A in fig. 1.2). The HRXRD characteristics are good, with peak widths near the theoretical value and, if the layer is thick enough, Pendellosung fringes. The optical anisotropy is small and the layers are thermally stable. The only change in region II is that a low density of misfit dislocations is present, probably formed from threading dislocations from the substrate (B in fig. 1.2). The relaxation is no longer zero, but still very small. The lines dividing regions I and II are at $t_{c,MB}$. This boundary is difficult to determine experimentally; we use $t_{c,MB}$ based upon the work of others.

Going from region II to region III, the sample morphology and x-ray characteristics become poor. In addition, the optical anisotropy changes from small to large. We expect the layers to be thermally unstable, but we have not verified this experimentally. We separate the regions by lines at $4 \times t_{c,MB}$. We use this value based upon our HRXRD and VAAE measurements. It is the same as the **C** lines in fig. 2.13a. We note, however, that based upon the HRXRD FWHM ratio, we found a transition region from 3 to $9 \times t_{c,MB}$. Hence, the boundaries between regions in fig. 6.2 are only approximate. It is likely that they depend on variables such as growth temperature.

Region IV represents samples which have undergone substantial relaxation ($\bar{R} >$ 10%). The strain is relieved by a high density of misfit dislocations and possibly other defects such as stacking faults. The layers may relax further if annealed at high temperatures. The optical anisotropy is small, perhaps because the surface morphology is no longer dominated by elongated islands. We used a value of $10 \times t_{c,MB}$ to separate regions III and IV. Again, this is a rough approximation (same as curves **R** in fig. 2.13), based upon our HRXRD and VAAE data.

For clarity, we do not show most of our data points in fig. 6.2; the reader is referred to fig. 2.13. We do, however, include the samples on which we measured

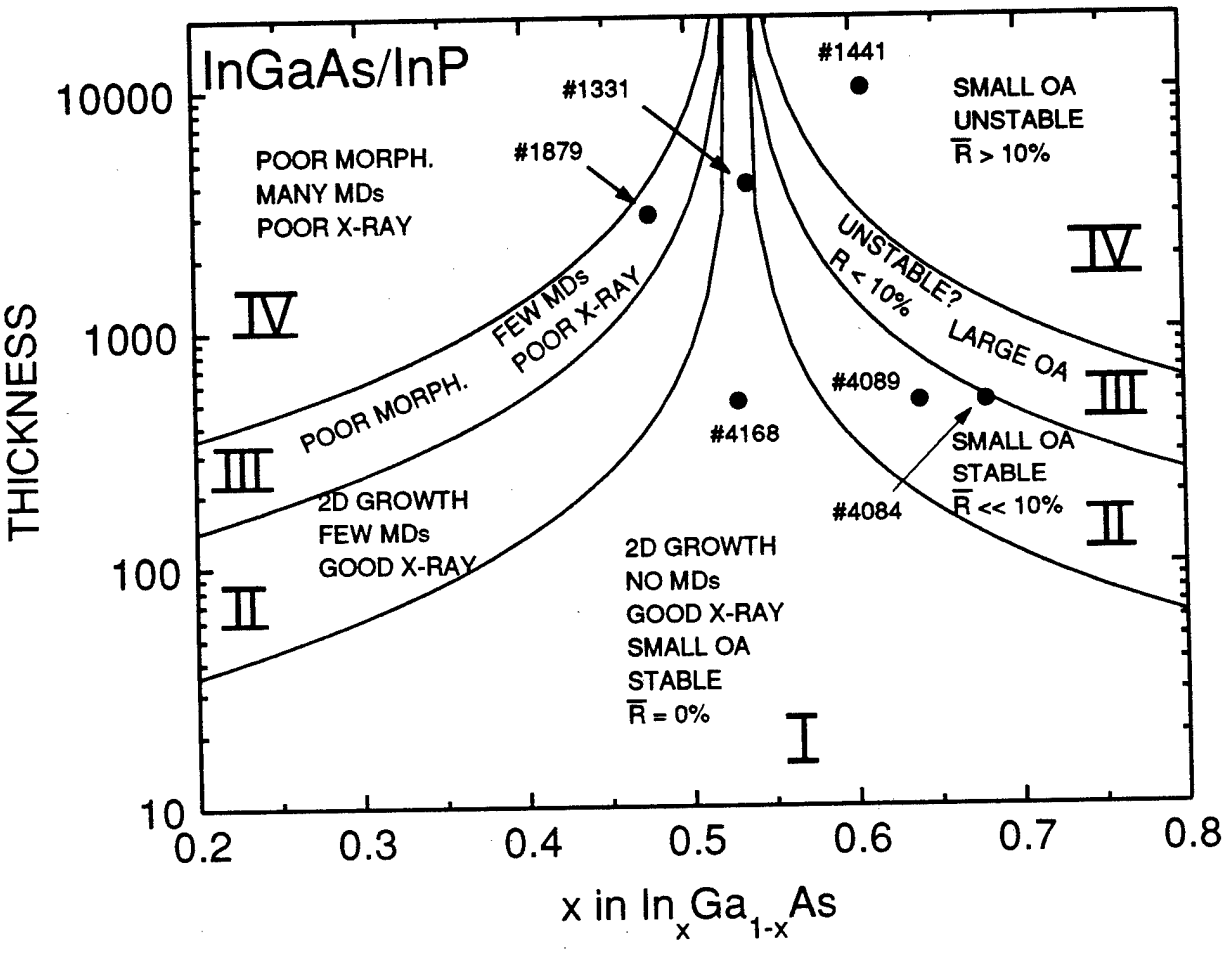

Figure 6-2: Proposed regions based upon material quality and thermal stability of our InGaAs layers on InP. The solid lines are at $t_{c,MB}$, $5t_{c,MB}$, and $12t_{c,MB}$, and are only approximate boundaries. The descriptions in regions II, III, and IV apply to both tension and compression; they are separated because of limited space on the plot. Samples used in thermal stability experiments are indicated. MDs = misfit dislocations, OA = optical anisotropy, Morph = morphology.

thermal stability in chapter 4. Samples 1331 and 4168 are in region I and, based upon HRXRD and Hall mobility measurements, respectively, are thermally stable. Samples 4089 and 4084 in region II are also thermally stable. In our model, these samples did not relax because their surfaces did not roughen during growth. Sample 1879 is in region III, but was thermally stable based upon HRXRD measurements (fig. 4.4). Its morphology and optical anisotropy are also consistent with region II samples. We note that this layer is in the HRXRD transition region, with $t/t_{c,MB} = 7.3$. Sample 1441 is well into region IV and exhibits all the expected characteristics. The additional relaxation during annealing of this layer can be explained by the nucleation of additional half-loop dislocations. Another possibility is that existing misfit dislocations lengthened during the annealing cycle.

Much of fig. 6.2 may also apply to layers of InAlAs on InP. As shown in fig. 2.13b, HRXRD measurements can be used to separate layers into regions similar to II, III, and IV in fig. 6.2. There was a difference in tension and compression, with layers in tension retaining high crystalline quality longer. InAlAs layers in tension did not usually exhibit large optical anisotropy. In addition, layers in tension did not relax as much as comparable layers in compression (figs. 4.12 and 4.13). We speculate that the evolution of surface roughness is much different in tension and compression, possibly due to differences in cation mobilities. The difference could result in fewer heterogeneous nucleation sites and hence less lattice relaxation in tension.

For an alternative interpretation of the InAlAs relaxation data, we return to the Dodson-Tsao model discussed in chapter 4. For InAlAs in tension, the value of the fitting parameter D was about three orders of magnitude lower than $D's$ for InAlAs in compression or InGaAs in tension or compression. D is a function of dislocation mobility. One possibility is that at the relatively high densities of dislocations required for significant relaxation, dislocations are pinning each other, reducing the average dislocation mobility. This phenomenon is also known as work hardening.[146] It is not clear why dislocation pinning should be different in tension and compression, but it could be related to differences in surface roughening and the types of dislocations present.

In section 6.1, we considered the role of heterogeneous nucleation in lattice relaxation. Based upon our proposed model, we now discuss techniques which can be used to grow high-quality, thermally-stable strained layers.

We know of no reports of misfit dislocations or 3-D growth in InGaAs or InAlAs layers thinner than $t_{c,MB}$. Hence, one is always safe in staying below the Matthews-Blakeslee limit. In fact, for device or circuit applications in which a single misfit dislocation would be catastrophic, $t_{c,MB}$ should probably be used as an upper limit. For applications in which a relatively low density of misfit dislocations is tolerable (*e.g.* HFETs), it may be possible to exceed the severe constraints imposed by the Matthews-Blakeslee limit. Klem has shown that the misfit dislocation density is a function of the density of threading dislocations in the substrate for InGaAs growth on GaAs.[147] Hence, one should begin by choosing substrates with the lowest possible density of threading dislocations.[‡] As mentioned earlier, there are several potential sources of heterogeneous nucleation including oval defects and particulates. At this point in time, it is not clear which sources are dominant. We will not attempt to review the literature on substrate preparation and elimination of oval defects, but one should take steps to minimize probable nucleation sources. Finally, surface roughness and 3-D growth should be avoided.

Considerable progress has been made in the modelling of crystalline growth modes by molecular dynamics simulations.[26,27] To our knowledge, however, there is not yet a simple way to predict the onset of 3-D growth or surface roughening for a given material and set of growth conditions. Experimental evidence suggests that 3-D growth does not occur until thicknesses well beyond $t_{c,MB}$ for both InGaAs[39,43–45] and InAlAs.[45] Growth temperature plays a role, with 3-D growth occurring sooner at higher temperatures.[38,44,148] Hence, growth temperatures as low as possible[§] should be used. If surface roughness and 3-D growth are avoided, and the density of nucleation sources is low, epilayers with high crystalline quality and thermal stability should result.

[‡] As shown by Fitzgerald *et al.*[22] and Watson *et al.*,[140] the use of patterned substrates can reduce the dislocation density by limiting the number of threading dislocations available.

[§] If the growth temperature is too low, material quality will degrade, independent of strain.

6.5 Summary

In summary, we have shown that the contradictory results from studies of thermal stability of strained layers can be explained by the heterogeneous nucleation of dislocation loops. Our high quality InGaAs and InAlAs layers were thermally stable because of a relatively low density of nucleation sources in our MBE process. We propose that if a layer undergoes surface roughening or 3-D growth, additional nucleation sources are made available, allowing substrate relaxation during growth or subsequent annealing. Based upon these findings, we have suggested procedures for the growth of high-quality, thermally-stable strained layers beyond the Matthews-Blakeslee critical layer thickness.

Chapter 7

Summary

7.1 Conclusions

We used high-resolution x-ray diffraction (HRXRD) extensively in this work and found it to be a powerful and versatile characterization tool. It is routinely used to measure the composition of single epitaxial layers. We showed that if the thickness of a calibration layer is chosen properly, the InAs mole fraction in InGaAs or InAlAs on InP can be determined to within 0.01 with a single measurement. If HRXRD scans are combined with dynamical simulations, one can determine the composition in complex multi-layer heterostructures. In addition, HRXRD gives information about the crystalline quality of epitaxial layers. A good figure of merit is the ratio of the experimental to the theoretical epilayer peak width, with values close to unity representing high crystalline quality. The presence of interference fringes also indicates a coherent, high-quality layer. These criteria can detect degradation in crystalline quality earlier than direct measurements of lattice relaxation. HRXRD measurements are non-destructive and relatively simple and fast in most cases.

Variable azimuthal-angle ellipsometry (VAAE) is a new characterization technique which measures the optical anisotropy of epitaxial layers. Nearly lattice-matched layers of InGaAs and InAlAs always exhibit a small anisotropy which is caused by surface chemistry effects. Layers with a large mismatch often exhibit large optical anisotropies. We have attributed these large values to strain-induced roughness. This

roughness is correlated with a degradation in crystalline quality measured by HRXRD. In some cases, the morphology consists of islands elongated in the $[1\bar{1}0]$ direction. VAAE is simple, non-destructive, and extremely fast. It emerges as a potentially powerful technique for probing the limits of strained layer epitaxy.

Using the HRXRD FWHM ratio and interference fringes, we found that the crystalline quality of InGaAs and InAlAs epitaxial layers consistently remains unperturbed to thicknesses up to 3-9 $\times$ $t_{c,MB}$ for lattice mismatch up to $\pm$ 1%. For InAlAs, layers in tension can withstand larger mismatch than layers in compression (at constant thickness). For InGaAs, we observe no clear differences between compression and tension. Layers which are beyond $t_{c,MB}$ but have high crystalline quality may have a low density of misfit dislocations at the epilayer/substrate interface. Both TEM and VAAE show that such layers have good surface morphology, suggesting 2-D growth. In summary, the Matthews-Blakeslee critical layer thickness is not a sharp limit beyond which epilayer quality abruptly degrades.

Asymmetric HRXRD measurements show that partially relaxed epitaxial layers of InGaAs and InAlAs on (001) InP exhibit orthorhombic distortion. The maximum strain relief is in the [110] direction for either material in tension or compression. Symmetric HRXRD measurements reveal anisotropic peak broadening for certain samples, with a maximum peak width in the [110] direction. All observations are consistent with a model in which strain is relieved by 60° misfit dislocations, with a majority parallel to the $[1\bar{1}0]$ direction. TEM observations on selected samples confirm this model. For other samples, the situation may be more complex, with surface roughness and islands elongated in the $[1\bar{1}0]$ direction. The asymmetry is attributed to the fact that dislocations along the [110] and $[1\bar{1}0]$ directions have different dislocation cores in zinc-blende structures. Orthorhombic distortion must be taken into account when measuring the composition of partially relaxed epitaxial layers by HRXRD.

High-quality layers of InGaAs and InAlAs with thicknesses up to 9 $\times$ $t_{c,MB}$ were annealed at temperatures from 600 to 850°C. HRXRD measurements before and after the anneals showed no degradation of crystalline quality. In addition, MODFET

structures with strained InGaAs channels were annealed and characterized by Hall mobility measurements. The 300K mobilities were not affected by anneals. Some degradation in the 77K mobility occurred, but it is apparently the result of diffusion of Si dopant atoms into the channel rather than lattice relaxation. We attribute the thermal stability of our strained layers to: 1) insufficient energy to homogeneously nucleate half-loop dislocations, 2) insufficient number of threading dislocations in the substrate, and 3) insufficient number of sites (possibly impurity clusters or oval defects) for heterogenerous nucleation of dislocations.

Based upon TEM, VAAE, and HRXRD measurements, a roughening transition occurs when the layer thickness and mismatch become too large. This transition may be equivalent to the so-called 2-D to 3-D transition other authors have observed using RHEED. We cannot, however, confirm that true 3-D growth results in all cases. One possibility is that surface roughness is sometimes an intermediate stage between 2-D growth with a smooth morphology and true 3-D or island growth. We propose that surface roughening provides defect sites for the heterogeneous nucleation of dislocation loops. Layers which reach the roughening transition can then relax substantially. This model is also consistent with the thermal stability of high-quality strained layers: such layers did not reach the roughening transition during growth.

The fact that thermally stable layers with high crystalline quality can be grown to thicknesses greater than $t_{c,MB}$ suggests that such layers may be suitable for device applications. We grew and fabricated InAlAs/InGaAs/InP HFETs in which the InAlAs pseudo-insulator was AlAs-rich, with $t/t_{c,MB} = 2.0$. The device results were excellent and showed no signs of degradation due to lattice mismatch. Others have fabricated similar HFETs with strained InGaAs channels exceeding $t_{c,MB}$ by a factor of 2-4 without degradation. These results suggest that the thickness-mismatch limit for InP-based HFETs may be approximated by the boundary between regions II and III in fig. 6.2. The limits may be different for other devices, but it is clear that the Matthews-Blakeslee critical layer thickness should not be taken as an absolute upper limit in all cases.

7.2 Suggestions for Future Work

Strained layer epitaxy is likely to remain an important field for many years to come. Its challenges range from fundamental problems of materials science to practical applications for electronic and optical devices. Based upon the research described here, we have identified three promising areas which could benefit from additional work.

In chapter 6, we proposed a model relating lattice relaxation, material quality, and growth modes. A few key experiments could confirm or refute this model. First, the thermal stability of samples from region III of fig. 6.2 (surface roughening and crystalline degradation without substantial relaxation during growth) should be tested. Our model predicts that relaxation will occur during annealing because of the defects associated with surface roughness. Second, additional sources of heterogeneous nucleation sites should be introduced into samples from region II (high-crystalline quality with $t > t_{c,MB}$). Damage could be created by ion implantation after growth and before annealing. Sample surfaces could be scratched before growth or between growth and annealing. Other possibilities include the use of substrates with much higher densities of threading dislocations ($\rho > 10^6/\text{cm}^2$), and the growth of epitaxial layers with extremely high doping densities (n or p $> 10^{19}/\text{cm}^3$). We would expect some if not all of these procedures to result in unstable epitaxial layers. HRXRD could be used as the primary characterization tool to assess thermal stability. TEM could be applied to selected samples to determine relaxation mechanisms.

Additional studies of the origin of optical anisotropy could help to make VAAE a standard characterization tool. Correlation of VAAE results with plan-view and cross-sectional TEM as well as optical microscopy should lead to a better understanding of the growth morphologies which cause optical anisotropy. Thus far, we have only used VAAE to characterize samples after growth. VAAE could also be applied as an *in situ* characterization technique. This would allow measurements on each layer in complex heterostructures and might provide enough warning so that strained layer growth can be halted before severe degradation occurs. VAAE could be applied in either an MBE or MOCVD system. It might be especially useful in MOCVD since RHEED is

not available. Some groups have already installed ellipsometers on MOCVD systems; VAAE measurements could be made with little additional effort.

We have investigated asymmetries in x-ray and optical measurements. Others have observed electrical anisotropies in strained III-V layers as well. It is not yet clear whether the electrical anisotropies result from asymmetric arrays of misfit dislocations, surface roughness, 3-D growth, or some combination. Comparison to TEM measurements should settle this question. Mobilities must be measured with lithographically-defined Hall patterns to separate geometry effects from true anisotropies. Such measurements may be very sensitive to the onset of dislocations. They could be combined with annealing to investigate thermal stability. Actual device measurements are, of course, more time-consuming, but can provide a wealth of additional information. For example, our findings of thermal stability based upon the mobility of strained-channel MODFET heterostructures should be confirmed by fabricating and testing MODFETs on samples with and without post-growth annealing.

Appendix A

Molecular Beam Epitaxy of InGaAs and InAlAs

The InGaAs and InAlAs layers characterized in this study were grown by molecular beam epitaxy (MBE). In general, we used established growth and calibration procedures. The procedures are described in this appendix.

InP substrates from Sumitomo Electric were used for all growths. They were 5 cm in diameter, 350 μm thick, and nominally within 0.5° of the (001) orientation. The InP was doped with Fe to make it semi-insulating, with a resistivity of at least 10^6 ohm-cm. The wafers were pre-etched and shipped in nitrogen. Wafers were scribed and mounted on molybdenum blocks with indium. We did no wafer cleaning or etching except for blowing the samples with nitrogren after mounting.

Epitaxial layers were grown in a Riber 2300 solid source MBE system. A schematic of the evaporation chamber is shown in fig. A-1. The base pressure of this chamber is typically 1-2 $\times 10^{-10}$ Torr (after cooling with liquid nitrogen). The system also includes preparation and load-lock chambers. The cell temperatures, shutter positions, and substrate temperature are computer-controlled.[149]

Samples were baked in the preparation chamber at 200-250°C for 45-60 minutes prior to growth. They were then transferred into the evaporation chamber and ramped up to growth temperature under an As overpressure. Samples were rotated during layer growth. The ratio of the group V (As) to group III (In, Al, and Ga)

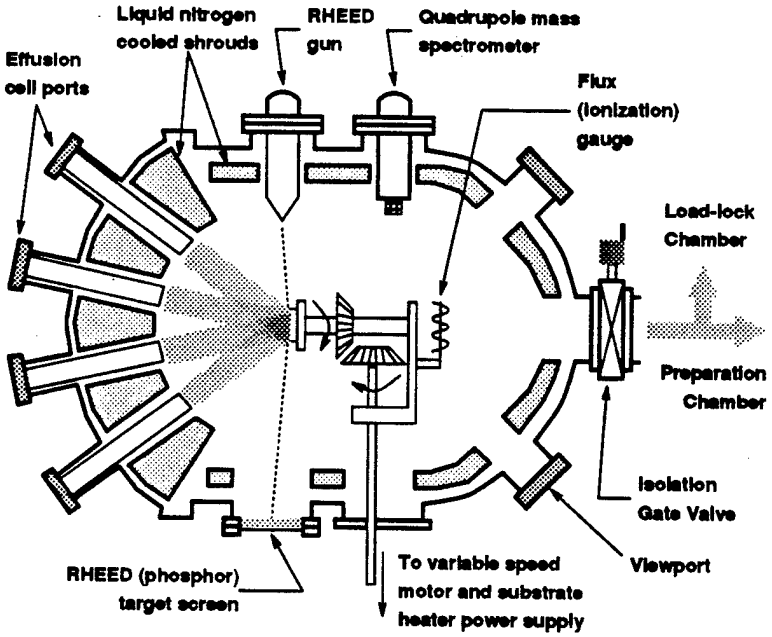

Figure A-1: Schematic of Riber 2300 Molecular Beam Epitaxy system used in this study (courtesy of J.C. Vlcek).

beam-equivalent-pressures was between 15:1 and 25:1 during growth, with background pressures in the 10^{-8} Torr range.

Sample temperature was monitored by a thermocouple and an optical pyrometer during growth. The two measurements often differed by as much as 50°C. Surface reconstruction patterns were monitored by reflection high-energy electron diffraction (RHEED) during ramp-up. Layers were always grown at temperatures above the 2×4 InP reconstruction and typically 5-25°C below the 4×2 InP reconstruction. We estimate that the growth temperature was always between 460 and 510°C.

In MBE, it is rare for a source molecule to strike a gas molecule because of the extremely low pressure. Hence, the process can be modelled as line-of-sight evaporation into a perfect vacuum. The flux of a species D evaporated into a perfect vacuum is given by:[144]

$$F_D = \frac{P_D}{\sqrt{2\pi M_D k T_D}} \tag{A.1}$$

where P_D is the equilibrium vapor pressure of D, M_D is the mass of species D, T_D is the absolute temperature, and k is the Boltzmann constant. The vapor pressure is

an exponential function of temperature:

$$P_D = P_{0,D} e^{-E_{A,D}/kT_D} \tag{A.2}$$

where $E_{A,D}$ is the activation energy and $P_{0,D}$ is a constant independent of temperature. Combining (A.1) and (A.2) for Ga evaporation:

$$F_{Ga} = \frac{P_{0,Ga} e^{-E_{A,Ga}/kT_{Ga}}}{\sqrt{2\pi M_{Ga} k T_{Ga}}} \tag{A.3}$$

We grew a series of $In_xGa_{1-x}As$ layers with a constant In cell temperature and varying Ga cell temperature. For this case, assuming that the mole fractions of GaAs and InAs are proportional to their fluxes (no re-evaporation), we have:

$$\frac{1-x}{x} = \frac{F_{Ga}}{F_{In}} = \frac{B}{\sqrt{T_{Ga}}} e^{-E_{A,Ga}/kT_{Ga}} \tag{A.4}$$

where B is a constant. To a good approximation, we can neglect the $\sqrt{T}$ term in (A.4) and obtain:

$$\frac{1-x}{x} \cong A e^{-E_{A,Ga}/kT_{Ga}} \tag{A.5}$$

where A is a constant.

A plot of the logarithm of (1-x)/x versus inverse absolute temperature should approximately yield a straight line with a slope of ($-E_A/k$). In fig. A-2, we show the data for 13 samples of $In_xGa_{1-x}As$ grown from the same charges of Ga and In. The composition of each InGaAs layer was measured by HRXRD, as described in chapter 2. A least-squares fit gives an activation energy of 2.19 eV or 25,340 K for Ga.[†] We assume that the activation energy (slope) remains constant after cell recharging. The intercept of the line (or the lattice-matching temperature) typically changes when the cells are recharged.

Given the Ga cell temperature, the growth rate can also be estimated. We again

[†]The activation energy of a cell can also be determined from flux measurements. Such measurements gave a value of 2.12 eV for the Ga cell.

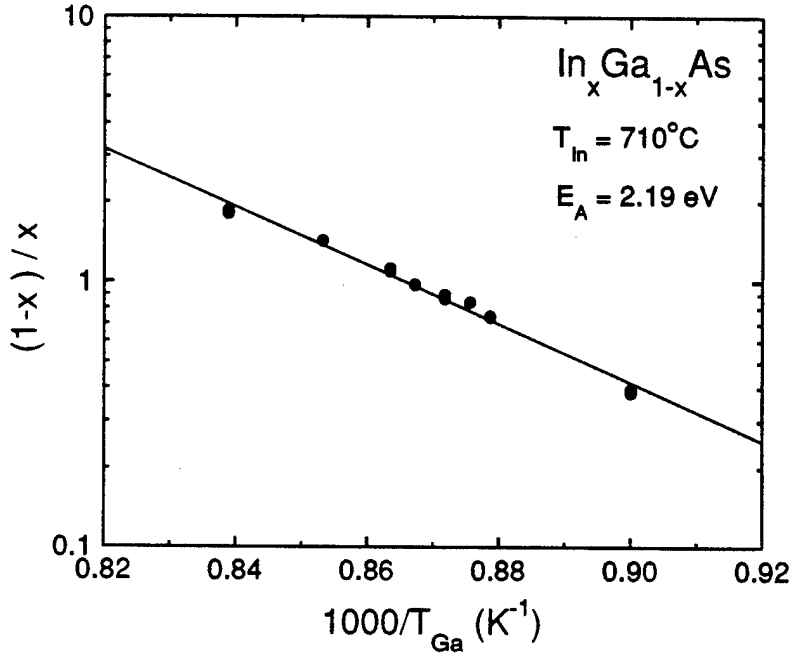

Figure A-2: Calibration of the composition of $In_xGa_{1-x}As$: plot of ratio of GaAs mole fraction to InAs mole fraction versus inverse absolute Ga cell temperature (In cell temperature was constant) for 13 samples. The slope, 2.19 eV, is the activation energy for the Ga cell (see eq. A.5). Composition was measured by HRXRD.

assume that all the Ga and In will be absorbed on the substrate surface. The growth rate, G, will then be proportional to the sum of the Ga and In fluxes:

$$G = C(F_{In} + F_{Ga}) \tag{A.6}$$

where C is a constant. We assume that the growth rate, G_0, and composition, x_0, are known for the Ga temperature, T_0. (T_0 is often the temperature which yields lattice-matched InGaAs on InP, but it can be any temperature.) Combining (A.4) and (A.6):

$$G_0 = CF_{Ga}(T_0)\left[\frac{x_0}{1-x_0} + 1\right] \tag{A.7}$$

We now wish to determine the growth rate, G_1, at the Ga temperature T_1. We obtain the composition, x_1, from (A.5) or fig. A-2. Using (A.3), we can approximate the ratio of Ga fluxes at T_1 and T_0

$$\frac{F_{Ga}(T_1)}{F_{Ga}(T_0)} \cong e^{(-E_A/k)(1/T_1-1/T_0)} \tag{A.8}$$

We can now express the growth rate as:

$$G_1 = C[F_{In} + F_{Ga}(T_1)] = CF_{Ga}(T_1)\left[\frac{x_1}{1-x_1} + 1\right] \tag{A.9}$$

Combining (A.8) and (A.9):

$$G_1 \cong CF_{Ga}(T_0)\left[\frac{x_1}{1-x_1} + 1\right] e^{(-E_A/k)(1/T_1-1/T_0)} \tag{A.10}$$

Given the activation energy for the Ga cell and a calibration sample for which the composition and thickness have been measured, the composition and growth rate can be estimated for any Ga cell temperature from (A.5) and (A.10). We measured the thickness of calibration samples by one of three techniques: profilometry after selective etching, HRXRD fringe spacing (see section 2.1), and infrared reflectance.[150] Using the above procedures, we were usually able to grow $In_xGa_{1-x}As$ with x within 0.01 of the desired value. Thickness was typically within 5-10% of the targeted value.

Procedures analogous to those above were used for $In_yAl_{1-y}As$ calibration, but the error in y was sometimes as large as 0.02. The reason for the larger errors appears to be fluctuations in the activation energy of the Al cell. Our HFET heterostructures are an ideal way to measure the Al activation energy because they typically have well-defined HRXRD peaks from both the buffer and insulator layers (see fig. 5.2). Values of $E_{A,Al}$ determined from HFET structures ranged from 2.4 to 3.4 eV.

A key parameter in our HFETs is the electron concentration in the channel. We used Hall/van der Pauw measurements of electron concentration to calibrate Si doping of InGaAs. A plot of electron concentration versus inverse Si cell temperature yielded a Si cell activation energy of 4.8 eV for $n = 3 \times 10^{18}$ to $3 \times 10^{19}/\text{cm}^3$. In this doping range, however, we were only able to consistently obtain the desired electron concentration within a factor of two. We suspect the variations are due to the amphoteric nature of Si in III-V's. The incorporation of Si is known to be sensitive to the growth temperature which, as discussed above, is not constant for all growths.[151,152]

Appendix B

Material Parameters of InP, GaAs, InAs, and AlAs*

Property	Parameter (units)	InP	GaAs	InAs	AlAs
Lattice constant	a_0 (Å)	5.8688	5.6532	6.0584	5.6623
Density	ρ (g/cm^3)	4.787	5.307	5.667	3.81
Thermal expansion	$\alpha_{th}(\times 10^{-6}/^oC)$	4.56	6.63	5.16	
Elastic constant	$C_{11}(\times 10^{11} dyn/cm^2)$	10.22	11.88	8.33	15.1
Elastic constant	$C_{12}(\times 10^{11} dyn/cm^2)$	5.76	5.37	4.53	5.7
Elastic constant	$C_{44}(\times 10^{11} dyn/cm^2)$	4.6	5.94	3.96	5.89
Young's modulus	Y $(\times 10^{11} dyn/cm^2)$	9.49	12.40	7.93	16.50
Shear modulus	G $(\times 10^{11} dyn/cm^2)$	3.02	4.15	2.59	5.1
Poisson's ratio	ν	0.36	0.311	0.352	0.274
Band gap	E_g (eV)	1.35	1.42	0.36	2.15
Electron mass	m_e^*/m_0	0.08	0.067	0.023	0.14
Light-hole mass	m_{lh}^*/m_0	0.089	0.074	0.027	0.15
Heavy-hole mass	m_{hh}^*/m_0	0.85	0.62	0.6	0.76
Electron mobility	$\mu_e(cm^2/\text{V-sec})$	4500	8500	28000	
Hole mobility	$\mu_h(cm^2/\text{V-sec})$	130	400	450	
Static dielectric constant	ϵ_s/ϵ_0	12.4	13.1	14.6	8.2
Optical dielectric constant	$\epsilon_\infty/\epsilon_0$	9.55	11.1	12.3	10.1
Refractive index (1.96 eV)	n	3.54	3.86	3.96	3.11
Extinction coef. (1.96 eV)	k	0.30	0.20	0.61	0.0015
Absorption coef. (1.96 eV)	$\alpha(/cm)$	61000	39000	120000	290

*Parameters from references[60,87–89]

Appendix C

Matthews-Blakeslee Critical Layer Thickness

In this appendix, we briefly outline the Matthews-Blakeslee theory of critical layer thickness and modify it to account for anisotropic elastic properties. Matthews and Blakeslee estimated the critical layer thickness, t_c, by equating the force exerted by misfit strain with the tension in a dislocation line.[2] The result was a transcendental equation:*

$$t_c = \frac{b(1-\nu\cos^2\alpha)}{8\pi f(1+\nu)\cos\lambda}\left(\ln\frac{t_c}{b}+1\right) \tag{C.1}$$

where b is the magnitude of the Burger's vector of the dislocation, f is the lattice mismatch, α is the angle between the dislocation line and its Burger's vector, λ is the angle between the slip direction and that direction in the film plane which is orthogonal to the line of intersection of the slip plane and the interface, and ν is Poisson's ratio which is related to the elastic stiffness coefficients by:

$$\nu = \frac{C_{12}}{C_{11}+C_{12}} \tag{C.2}$$

For III-V semiconductors, experimental work has shown that misfit dislocations

*Matthews and Blakeslee originally considered a special type of strained-layer superlattice for which the right-hand-side of (C.1) has an additional factor of 4 in the numerator.

are primarily of the 60° type on (001) substrates.[22] For this case, $\cos\lambda = \cos\alpha = 1/2$, $b = a_e/\sqrt{2}$, and (C.1) becomes:

$$t_c = \frac{a_e(1-\nu/4)}{4\sqrt{2}\pi f(1+\nu)}\left(\ln\frac{\sqrt{2}t_c}{a_e}+1\right) \tag{C.3}$$

where a_e is the natural (relaxed) lattice constant of the epilayer.

To simplify calculations, Matthews[153,154] assumed that the epitaxial layer was elastically isotropic and that the shear modulus of the substrate was equal to the shear modulus of the epilayer. Hirth[155] and Fitzgerald[156] modified the Matthews theory to consider elastic anisotropy, a general feature of crystalline materials. Fitzgerald also considered unequal shear moduli, and obtained:

$$t_c = \frac{a_e(1-\nu/4)\,G_E G_S}{\sqrt{2}\pi f(1-\nu)\,Y(G_E+G_S)}\left(\ln\frac{\sqrt{2}t_c}{a_e}+1\right) \tag{C.4}$$

where Y is Young's modulus of the epilayer, and G_S and G_E are the shear moduli of the substrate and epilayer, respectively. In the case of biaxial stress applied to an anisotropic material, Y and G are given by:[154]

$$Y = C_{11} + C_{12} - \frac{2C_{12}^2}{C_{11}} \tag{C.5}$$

and

$$G = C_{44} - \frac{1}{3}(2C_{44} + C_{12} - C_{11}) \tag{C.6}$$

We plot the critical thickness from eq. (C.3) (isotropic) and eqs. (C.4)-(C.6) (anisotropic) in figs. C.1 (InGaAs) and C.2 (InAlAs). Throughout this thesis, we use the anisotropic critical thickness defined by (C.4) and refer to it as $t_{c,MB}$.

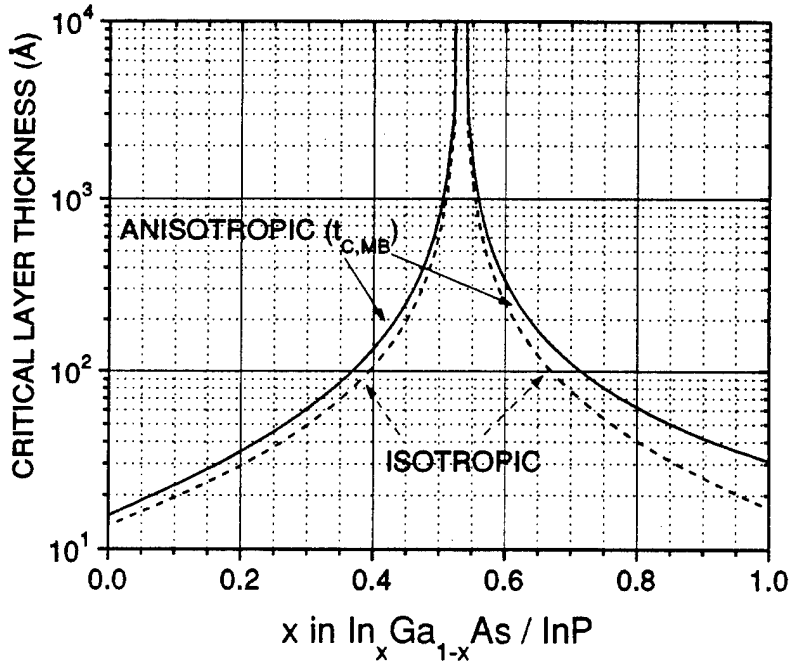

Figure C-1: Matthews-Blakeslee critical layer thickness for InGaAs layers on InP.

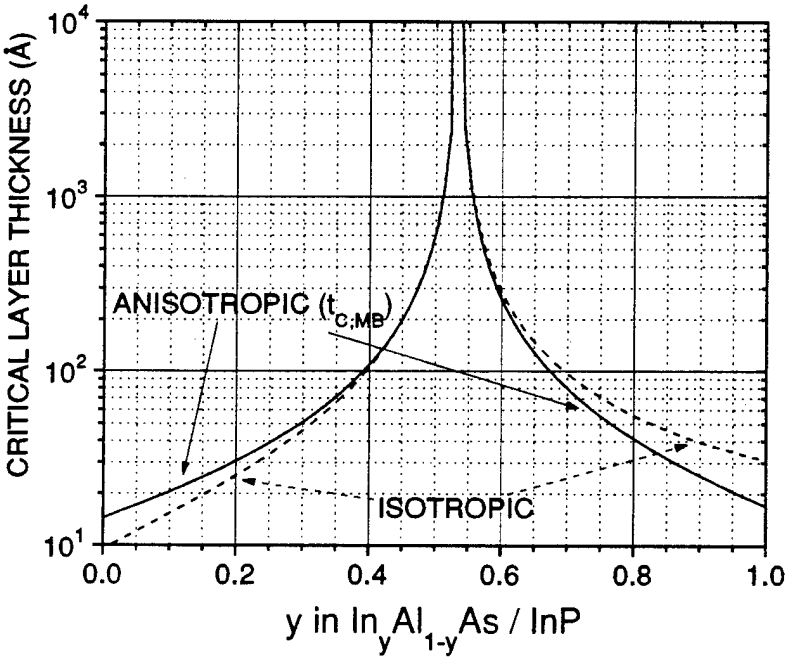

Figure C-2: Matthews-Blakeslee critical layer thickness for InAlAs layers on InP.

Bibliography

[1] K. Heime InGaAs Field Effect Transistors (John Wiley and Sons, New York, 1989).

[2] J. W. Matthews and A. E. Blakeslee, "Defects in epitaxial multilayers," *J. Cryst. Growth* **27**, 118 (1974).

[3] D.K. Gaskill, N. Bottka, L. Aina, and M. Mattingly, "Band-gap determination by photoreflectance on InGaAs and InAlAs lattice matched to InP," *Appl. Phys. Lett.* **56**, 1269 (1990).

[4] B. Elman, E.S. Koteles, P. Melman, K. Ostreicher, and C. Sung,"Low substrate temperature MBE growth and the critical layer thickness of InGaAs grown on GaAs," *J. Appl. Phys.* **70**, 2634 (1991).

[5] R. Hull and J.C. Bean, "Principles and concepts of strained-layer epitaxy," in Semiconductors and Semimetals **Vol. 33**, edited by T.P. Pearsall (Academic Press, San Diego, 1991) pp. 1-72.

[6] T. Yao, "Lattice strain in heteroepitaxial films," *Optoelectronics–Devices and Technologies* **6**, 37 (1991).

[7] P.J. Orders and B.F. Usher, "Determination of critical layer thickness in InGaAs/GaAs heterostructures by x-ray diffraction," *Appl. Phys. Lett.* **50**, 980 (1987).

[8] M. Gal, P.C. Taylor, B.F. Usher, and P.J. Orders, "Photoluminesence in strained InGaAs/GaAs heterostructures," *J. Appl. Phys.* **62**, 3898 (1987).

[9] I.J. Fritz, S.T. Picraux, L.R. Dawson, and T.J. Drummond, "Dependence of critical layer thickness on strain for InGaAs/GaAs strained-layer superlattices," *Appl. Phys. Lett.* **46**, 967 (1985).

[10] G.W. Wang, "Strain-relaxed epitaxial layers for high-speed electronic devices," *Appl. Phys. Lett.* **59**, 573 (1991).

[11] M. Tacano, Y. Sugiyama, Y. Takeuchi, and Y. Ueno, "Very high electron mobility $In_{0.80}Ga_{0.20}As$ heterostructure grown by molecular beam epitaxy," *J. Electron. Mat.* **20**, 1081 (1991).

[12] H. Temkin, D.G. Gershoni, S.N.G. Chu, J.M. Vandenberg, R.A. Hamm, and M.B. Panish, "Critical layer thickness in strained InGaAs/InP quantum wells," *Appl. Phys. Lett.* **55**, 1668 (1989).

[13] I. J. Fritz, "Role of experimental resolution in measurements of critical layer thickness for strained-layer epitaxy," *Appl. Phys. Lett.* **51**, 1080-1082 (1987).

[14] P.L. Gourley, I.J. Fritz, and L.R. Dawson, "Controversy of critical layer thickness for InGaAs/GaAs strained-layer epitaxy," *Appl. Phys. Lett.* **52**, 377 (1988).

[15] A. Madhukar, "Far from equilibrium vapour phase growth of lattice matched III-V compound semiconductor interfaces: Some basic concepts and Monte-Carlo computer simulations," *Surface Science* **132**, 344 (1983).

[16] B.W. Dodson and J.Y. Tsao, "Structural relaxation in metastable strained-layer semiconductors," *Annu. Rev. Mater. Sci.* **19**, 419 (1989).

[17] J.H. van der Merwe, "Misfit dislocation generation in epitaxial layers," *Crit. Rev. Sol. St. Mat. Sci.* **17**, 187 (1991).

[18] K. Rajan, E. Fitzgerald, K. Jagannadham, and W.A. Jesser, "Misfit accomodation at epitaxial interfaces," *J. Electron. Mat.* **20**, 861 (1991).

[19] G. J. Whaley and P. I. Cohen, "Relaxation of strained InGaAs during molecular beam epitaxy," *Appl. Phys. Lett.* **57**, 144-146 (1990).

[20] P.S. Peercy, B.W. Dodson, J.Y. Tsao, E.D. Jones, D.R. Myers, T.E. Zipperian, L.R. Dawson, R.M. Biefeld, J.F. Klem, and C.R. Hills, "Stability of strained quantum-well field-effect transistor structures," *IEEE Electron Dev. Lett.* **9**, 621 (1988).

[21] D.C. Bertolet, J.-K. Hsu, F. Agahi, and K.M. Lau, "Critical thickness of GaAs/InGaAs and AlGaAs/GaAsP strained quantum wells grown by organometallic chemical vapor deposition," *J. Electron. Mat.* **19**, 967 (1990).

[22] E. A. Fitzgerald, G. P. Watson, R. E. Proano, D. G. Ast, P. D. Kirchner, G. D. Pettit, and J. M. Woodall, "Nucleation mechanisms and the elimination of misfit dislocations at mismatched interfaces by reduction in growth area," *J. Appl. Phys.* **65**, 2220-2237 (1989).

[23] E. Bauer, "Phanomenologische teorie der kristallabscheidung an oberflachen," *Z. Kristallogr.* **110**, 423 (1958).

[24] R.W. Vook, "Nucleation and growth of thin films," *Opt. Eng.* **23**, 343 (1984).

[25] D. Gammon, B.V. Shanabrook, and D.S. Katzer, "Excitons, phonons, and interfaces in GaAs/AlAs quantum-well structures," *Phys. Rev. Lett.* **67**, 1547 (1991).

[26] M.H. Grabow and G.H. Gilmer, "Thin film growth modes, wetting and cluster nucleation," *Surface Science* **194**, 333 (1988).

[27] G.H. Gilmer, M.H. Grabow, and A.F. Bakker "Modeling of epitaxial growth," *Mater. Sci. Eng.* **B6**, 101 (1990).

[28] I. Tanaka and S. Ohkouchi, "GaAs heteroepitaxial growth on an InP (001) substrate," *Jpn. J. Appl. Phys.* **30**, L1662 (1991).

[29] M. Hopkinson, J.P.R. David, P.A. Claxton, and P. Kightley, "Growth of strained InAs/InP quantum wells by MBE," *Appl. Phys. Lett.* **60**, 841 (1992).

[30] J.L. de Miguel, M.-H. Meynadier, M.C. Tamargo, R.E. Nahory, and D.M. Hwang, "MBE growth and characterization of pseudomorphic InAs/InAlAs quantum wells," *J. Vac. Sci. Technol.* **B 6**, 617 (1988).

[31] G.J. Whaley and P.I. Cohen, "Diffraction studies of the growth of strained epitaxial layers," *Mat. Res. Soc. Symp. Proc.* **160**, 35 (1990).

[32] G.L. Price, "Critical-thickness and growth-mode transitions in highly strained InGaAs films," *Phys. Rev. Lett.* **66**, 469 (1991).

[33] D.J. Eaglesham and M. Cerullo, "Dislocation-free Stranski-Krastanow growth of Ge on Si(100)," *Phys. Rev. Lett.* **64**, 1943 (1990).

[34] C.W. Snyder, B.G. Orr, D. Kessler, and L.M. Sander, "Effect of strain on surface morphology in highly strained InGaAs films," *Phys. Rev. Lett.* **66**, 3032 (1991).

[35] S. Guha, A. Madhukar, and K.C. Rajkumar, "Onset of incoherency and defect introduction in the initial stages of MBE growth of highly strained InGaAs on GaAs(001)," *Appl. Phys. Lett.* **57**, 2110 (1990).

[36] P.R. Berger, K. Chang, P. Bhattacharya, J. Singh, and K.K. Bajaj, "Role of strain and growth conditions on the growth front profile of InGaAs on GaAs during the pseudomorphic growth regime," *Appl. Phys. Lett.* **53**, 684 (1988).

[37] K.R. Breen, P.N. Uppal, and J.S. Ahearn, "Homogeneous nucleation of dislocations in $In_{0.4}Ga_{0.6}As$/GaAs near critical thickness," *J. Vac. Sci. Technol.* **B 8**, 730 (1990).

[38] S.M. Wang, T.G. Andersson, and M.J. Ekenstedt, "Interface morphology in MBE grown InGaAs/GaAs strained heterostructures," *Appl. Phys. Lett.* **59**, 2156 (1991).

[39] K.H. Chang, R. Gibala, D.J. Srolovitz, P.K. Bhattacharya, and J.F. Mansfield, "Crosshatched surface morphology in strained III-V semiconductor films," *J. Appl. Phys.* **67**, 4093 (1990).

[40] M. Lentzen, D. Gerthsen, A. Forster, and K. Urban, "Growth mode and strain relaxation during the initial stage of InGaAs growth on GaAs (001)," *Appl. Phys. Lett.* **60**, 74 (1992).

[41] J.Y. Yao, T.G. Andersson, and G.L. Dunlop, "The interfacial morphology of strained epitaxial InGaAs/GaAs," *J. Appl. Phys.* **69**, 2224 (1991).

[42] B. Elman, E.S. Koteles, P. Melman, C. Jagannath, J. Lee, and D. Dugger, "*In situ* measurements of critical layer thickness and optical studies of InGaAs quantum wells grown on GaAs substrates," *Appl. Phys. Lett.* **55**, 1659 (1989).

[43] M. Gendry, V. Drouot, C. Santinelli, and G. Hollinger, "Critical thicknesses of highly strained InGaAs layers grown on InP by molecular beam epitaxy," *Appl. Phys. Lett.* **60**, 2249 (1992).

[44] M. Gendry, V. Drouot, C. Santinelli, and G. Hollinger, C. Miossi, and M. Pitaval, "Growth modes and relaxation mechanisms of strainedInGaAs layers grown on InP (001)," *J. Vac. Sci. Technol.* **B 10**, 1829 (1992).

[45] J.-L. Lievin and C.G. Fonstad, "Reflection high-energy electron diffraction intensity oscillation study of InGaAs and InAlAs on InP: Application to pseudomorphic heterostructures," *Appl. Phys. Lett.* **51**, 1173 (1987).

[46] J.Y. Yao, T.G. Andersson, and G.L. Dunlop, "Structure of lattice-strained InGaAs/GaAs layers studied by transmission electron microscopy," *Appl. Phys. Lett.* **53**, 1420 (1988).

[47] J.W. Cahn, "Phase separation by spinodal decomposition in isotropic systems," *J. Chem. Phys.* **42**, 93 (1965).

[48] F. Glas, "Elastic state and thermodynamical properties of inhomogeneous epitaxial layers: Application to immiscible III-V alloys," *J. Appl. Phys.* **62**, 3201 (1987).

[49] R. Bruinsma and A. Zangwill, "Morphological transitions in solid epitaxial overlayers," *Europhys. Lett.* **4**, 729 (1987).

[50] P. Henoc, A. Izrael, M. Quillec and H. Launois, "Composition modulation in LPE InGaAsP layers lattice matched to InP substrates," *Appl. Phys. Lett.* **40**, 963 (1982).

[51] F. Peiro, A. Cornet, J.R. Morante, S. Clark, and R.H. Williams, "Influence of the composition modulation on the relaxation of $In_{0.54}Ga_{0.46}As$ strained layers," *Appl. Phys. Lett.* **59**, 1957 (1991).

[52] F. Peiro, A. Cornet, J.R. Morante, S. Clark, and R.H. Williams, "Alloy inhomogeneities in InAlAs strained layers grown by MBE," *J. Appl. Phys.* **71**, 2470 (1992).

[53] J.E. Oh, P.K. Bhattacharya, Y.C. Chen, O. Aina, and M. Mattingly, "The dependence of the electrical and optical properties of MBE InAlAs on growth parameters: Interplay of surface kinetics and thermodynamics," *J. Electron. Mat.* **19**, 435 (1990).

[54] J. Hornstra and W.J. Bartels, "Determination of the lattice constant of epitaxial layers of III-V compounds," *J. Cryst. Growth* **44**, 513 (1978).

[55] W.J. Bartels, "Characterization of thin layers on perfect crystals with a multipurpose high resolution x-ray diffractometer," *J. Vac. Sci. Technol.* **B1**, 338 (1983).

[56] A. Segmuller, "Characterization of epitaxial films by x-ray diffraction," *Advances in X-Ray Analysis* **29**, 353 (1986).

[57] I.C. Bassignana, C.J. Miner, and N. Puetz, "Photoluminescence and double-crystal x-ray study of InGaAs/InP: Effect of mismatch strain on bandgap," *J. Appl. Phys.* **65**, 4299 (1989).

[58] B.K. Tanner, "High resolution x-ray diffraction for the characterization of semiconducting materials," *Advances in X-Ray Analysis* **33**, 1 (1990).

[59] V. Swaminathan and A.T. Macrander, Materials Aspects of GaAs and InP Based Structures (Prentice Hall, Englewood Cliffs, NJ, 1991), pp. 181-232.

[60] Eq. (2.9) uses the most recent measurements of the lattice constant of AlAs: M.S. Goorsky, T.F. Kuech, M.A. Tischler, and R.M. Potemski, *Appl. Phys. Lett.* **59**, 2269 (1991); B.K. Tanner, A.G. Turnbull, C.R. Stanley, A.H. Kean, and M. McElhinney, *ibid.*, **59**, 2272 (1991).

[61] M.A.G. Halliwell, M.H. Lyons, and M.J. Hill, "The interpretation of x-ray rocking curves from III-V semiconductor device structures," *J. Cryst. Growth* **68**, 523 (1984).

[62] M. A. Capano, "X-ray studies of strained overlayers," PhD Thesis, MIT, 1989.

[63] X-ray simulation program RADS from Bede Scientific; see D.K. Bowen, N. Loxley, B.K. Tanner, L. Cooke, and M.A. Capano, "Principles and performance of a PC-based program for simulation of double-axis x-ray rocking curves of thin epitaxial layers," *Mat. Res. Soc. Symp. Proc.* **208**, 113 (1991).

[64] C.R. Wie, "Relaxation and rocking-curve broadening of strained GaInAs single layers on (001) GaAs," *J. Appl. Phys.* **65**, 2267 (1989).

[65] J.C. Bean, L.C. Feldman, A.T. Fiory, S. Nakahara, and I.K. Robinson, "GeSi/Si strained-layer superlattice grown by molecular beam epitaxy," *J. Vac. Sci. Technol.* **A 2**, 436 (1984).

[66] B.R. Bennett and J.A. del Alamo, "Relaxation of mismatched InAlAs/InP heterostructures," *Mat. Res. Soc. Symp. Proc.* **240**, 153 (1992).

[67] B.R. Bennett and J.A. del Alamo, "High quality InGaAs/InP and InAlAs/InP heterostructures beyond the Matthews-Blakeslee critical layer thickness," Proc. 4th Int. Conf. on InP, 650 (1992).

[68] B.R. Bennett and J.A. del Alamo, "Mismatched InGaAs/InP and InAlAs/InP heterostructures with high crystalline quality," submitted to *J. Appl. Phys.*

[69] K.B. Chough, T.Y. Chang, M.D. Feuer, and B. Lalevic, "Comparison of device performance of highly strained GaInAs/AlInAs MODFETs," *Electron. Lett.* **28**, 329 (1992).

[70] E. Tournié, L. Tapfer, T. Bever, and K. Ploog, "Structural properties and transport characteristics of pseudomorphic GaInAs/AlInAs modulation-doped heterostructures grown by molecular beam epitaxy," *J. Appl. Phys.* **71**, 1790 (1992).

[71] E. Tournié, Y.-H. Zhang, N.J. Pulsford, and K. Ploog, "Structural and optical properties of AlInAs layers grown on InP by MBE: influence of the substrate temperature and of a buffer layer," *J. Appl. Phys.* **70**, 7362 (1991).

[72] R. People and J.C. Bean, "Calculation of critical layer thickness versus lattice mismatch for GeSi/Si strained-layer heterostructures," *Appl. Phys. Lett.* **47**, 322 (1985).

[73] C. Bocchi, C. Ferrari, P. Franzosi, G. Fornuto, S. Pellegrino, and F. Taiariol, "LPE highly perfect InGaAs/InP structure characterization by x-ray double crystal diffractometry," *J. Electron. Mat.* **16**, 245 (1987).

[74] B.R. Bennett and J.A. del Alamo, "Orthorhombic distortion of mismatched InGaAs/InP heterostructures," *J. Electron. Mat.* **20**, 1075 (1991).

[75] J.F. Nye, Physical Properties of Crystals (Clarendon Press, Oxford, UK 1985).

[76] M. S. Abrahams, L. R. Weisberg, C. J. Buiocchi, and J. Blanc, "Dislocation morphology in graded heterojunctions: GaAsP," *J. Mater. Sci.* **4**, 223-235 (1969).

[77] M.S. Abrahams, J. Blanc, and C.J. Buiocchi, "Like-sign asymmetric dislocations in zinc-blende structure," *Appl. Phys. Lett.* **21**, 954 (1972).

[78] H. Nagai, "Anisotropic bending during epitaxial growth of mixed crystals on GaAs substrate," *J. Appl. Phys.* **43**, 4254-4256 (1972).

[79] K. S. Kavanagh, M. A. Capano, L. W. Hobbs, J.C. Barbour, P.M.J. Maree, W. Schaff, J.W. Mayer, D. Pettit, J.M. Woodall, J.A. Stroscio, and R.M. Feenstra, "Asymmetries in dislocation densities, surface morphology, and strain of GaInAs/GaAs single heterolayers," *J. Appl. Phys.* **64**, 4843-4852 (1988).

[80] M. Grundmann, U. Lienert, D. Bimberg, A. Fischer-Colbrie, and J. N. Miller, "Anisotropic and inhomogeneous strain relaxation in pseudomorphic $In_{0.23}Ga_{0.77}As/GaAs$ quantum wells," *Appl. Phys. Lett.* **55**, 1765-1767 (1989).

[81] V. S. Speriosu and T. Vreeland, Jr., "X-ray rocking curve analysis of superlattices," *J. Appl. Phys.* **56**, 1591-1600 (1984).

[82] S. N. G. Chu, A. T. Macrander, K. E. Strege, and W. D. Johnston, Jr., "Misfit stress in InGaAs/InP heteroepitaxial structures grown by vapor-phase epitaxy," *J. Appl. Phys.* **57**, 249-257 (1985).

[83] M.W. Wanlass, T.J. Coutts, J.S. Ward, K.A. Emery, and G.S. Horner, "High-efficiency, thin-film InP concentrator solar cells," Proc. of the 3rd Intern. Conf. on InP, 40 (1991).

[84] A. Suzuki, T. Itoh, T. Terakado, K. Kasahara, K. Asano, Y. Inomoto, H. Ishihara, T. Torikai, and S. Fujita, "Long-wavelength PINFET receiver OEIC on a GaAs-on-InP heterostructure," *Electron. Lett.* **23**, 954 (1987).

[85] S.R. Bahl, W.J. Azzam, and J.A. del Alamo, "Orientation dependence of mismatched InAlAs/InGaAs HFETs," *J. Cryst. Growth* **111**, 479 (1991).

[86] K. Sugii, H. Koizumi, and E. Kubota, "Precision lattice parameter measurements on doped InP single crystals," *J. Electron. Mat.* **12**, 701 (1983).

[87] Landolt-Bornstein Tables, **Vol. 22**, edited by O. Madelung and M. Schulz (Springer-Verlag, Berlin, 1987).

[88] Properties of Indium Phosphide (INSPEC, London, 1991).

[89] Properties of Gallium Arsenide (INSPEC, London, 1990).

[90] P.F. Fewster and C.J. Curling, "Composition and lattice-mismatch measurement of thin semiconductor layers by x-ray diffraction," *J. Appl. Phys.* **62**, 4154 (1987).

[91] E.F. Hockings, T.E. Seidel, C.M. Schmelz, and E.F. Steigmeier, "Thermal and electrical transport in InAs-GaAs alloys," *J. Appl. Phys.* **37**, 2879 (1966).

[92] R.E. Nahory, M.A. Pollack, W.D. Johnston, and R.L. Barns, "Band gap versus composition and demonstration of Vegard's law for InGaAsP lattice matched to InP," *Appl. Phys. Lett.* **33**, 659 (1978).

[93] K. Nakajima, A. Yamaguchi, K. Akita, and T. Kotani, "Composition dependence of the band gaps of InGaAsP quaternary solids lattice matched on InP substrates," *J. Appl. Phys.* **49**, 5944 (1978).

[94] J.P. Dismukes, L. Ekstrom, R.J. Paff, "Lattice parameter and density in germanium-silicon alloys," *J. Phys. Chem.* **68**, 3021 (1964).

[95] R. M. Azzam and N. M. Bashara, Ellipsometry and Polarized Light (North-Holland, New York, 1977).

[96] K. Riedling, Ellipsometry for Industrial Applications (Springer-Verlag, New York, 1988).

[97] E. Kuphal and H.W. Dinges, "Composition and refractive index of GaAlAs determined by ellipsometry," *J. Appl. Phys.* **50**, 4196 (1979).

[98] K.G. Merkel, P.G. Snyder, J.A. Woollam, S.A. Alterovitz, and A.K. Rai, "Characterization of multilayer GaAs/AlGaAs transistor structures by variable angle spectroscopic ellipsometry," *Jpn. J. Appl. Phys.* **28**, 1118 (1989).

[99] B.R. Bennett and J.A. del Alamo, "Index of refraction anisotropy in InGaAs/InP heterostructures measured by ellipsometry," *Mat. Res. Soc. Symp. Proc.* **160**, 713 (1990).

[100] B.R. Bennett and J.A. del Alamo, "Optical anisotropy in mismatched InGaAs/InP heterostructures," *Appl. Phys. Lett.* **58**, 2978 (1991).

[101] D. Morris, Q. Sun, C. Lacelle, A.P. Roth, J.L. Brebner, M. Simard-Normandin, and K. Rajan, "Structure property anisotropy in lattice-mismatched single heterostructures," *J. Appl. Phys.* **71**, 2321 (1992).

[102] D.E. Aspnes and A.A. Studna, "Anisotropies in the above-bandgap optical spectra of cubic semiconductors," *Phys. Rev. Lett.* **54**, 1956 (1985)

[103] D.E. Aspnes, "Above-bandgap optical anisotropies in cubic semiconductors: A visible-near ultraviolet probe of surfaces," *J. Vac. Sci. Technol.* **B3**, 1498 (1985).

[104] D.E. Aspnes, J.P. Harbison, A.A. Studna, and L.T. Florez, "Reflectance-difference spectroscopy system for real-time measurements of crystal growth," *Appl. Phys. Lett.* **52**, 957 (1988).

[105] D. J. Jackson and D. L. Persechini, "Waveguide formation in bulk GaAs and InP materials," *Electron. Lett.* **21**, 44 (1985).

[106] M.M.J. Treacy, J.M. Gibson, and A. Howie, "On elastic relaxation and long wavelength microstructures in spinodally decomposed InGaAsP epitaxial layers," *Philos. Mag. A* **51**, 389 (1985).

[107] Q. Sun, C. Lacelle, D. Morris, M. Buchanan, P. Marshall, P. Chow-Chong, and A.P. Roth, "Effects of substrate misorientation on anisotropic electron transport in InGaAs/GaAs heterostructures," *Appl. Phys. Lett.* **59**, 1359 (1991).

[108] H. Asai, "Anisotropic lateral growth in GaAs MOCVD layers on (001) substrates," *J. Cryst. Growth* **80**, 425 (1987).

[109] A. Salokatve and M. Hovinen, "The effects of strain on morphology and structural properties of InGaAs/InP (001) grown by MBE," *J. Appl. Phys.* **67**, 3378 (1990).

[110] Y. Horikoshi, H. Yamaguchi, F. Briones, and M. Kawashima, "Growth process of III-V compound semiconductors by migration-enhanced epitaxy ," *J. Cryst. Growth* **105**, 326 (1990).

[111] O. Acher, F. Omnes, M. Razeghi, and B. Drevillon, "In situ characterization by reflectance difference spectroscopy of III-V materials and heterojunctions grown by low pressure metalorganic chemical vapour deposition," *Mater. Sci. Eng.* **B5**, 223 (1990).

[112] O. Acher, S.M. Koch, F. Omnes, M. Defour, M. Razeghi, and B. Drevillon, "In situ investigation of the low-pressure metalorganic chemical vapor deposition of lattice-mismatched semiconductors using reflectance anisotropy measurements," *J. Appl. Phys.* **68**, 3564 (1990).

[113] J.P. Hirth and J. Lothe, Theory of Dislocations (John Wiley and Sons, New York, 1982).

[114] J. Oshinowo, A. Forchel, D. Grutzmacher, M. Stollenwerk, M. Heuken, and K. Heime, "Photoluminiscence study of interdiffusion in InGaAs/InP surface quantum wells," *Appl. Phys. Lett.* **60**, 2660 (1992).

[115] P.Y. Timbrell, J.-M. Baribeau, D.J. Lockwood, and J.P. McCaffrey, "An annealing study of strain relaxation and dislocation generation in SiGe/Si heteroepitaxy," *J. Appl. Phys.* **67**, 6292 (1990).

[116] A.C. Gossard, "Modulation doping of semiconductor heterostructures," in Molecular Beam Epitaxy and Heterostructures, L.L. Chang and K. Ploog, eds. (Martinus Nijhoff: Boston, 1985), pp. 499-532.

[117] M.E. Greiner and J.F. Gibbons, "Diffusion of Si in GaAs using rapid thermal processing: Experiment and model," *Appl. Phys. Lett.* **44**, 750 (1984).

[118] P.S. Peercy *et al.* "Fundamental issues in heteroepitaxy–a Department of Energy, Council on Materials Science panel report," *J. Mater. Res.* **5**, 852 (1990).

[119] W.A. Jesser and J.H. van der Merwe, "The prediction of critical misfit and thickness in epitaxy," in Dislocations in Solids, edited by F.R.N. Nabarro (Elsevier, Amsterdam, 1989) pp. 423-460.

[120] B.W. Dodson and J.Y. Tsao, "Relaxation of strained-layer semiconductor structures via plastic flow," *Appl. Phys. Lett.* **51**, 1325 (1987); Erratum: **52**, 852 (1988).

[121] H. Yaguchi, K. Fujita, S. Fukatsu, Y. Shiraki, and R. Ito, "Strain relaxation in MBE-grown SiGe/Si(100) heterostructures by annealing," *Jpn. J. Appl. Phys.* **30**, L1450 (1991).

[122] H. Alexander and P. Haasen, "Dislocations and plastic flow in the diamond structure," in Solid State Physics, F. Seitz, D. Turnbull, and H. Ehrenreich, eds. (Academic Press: New York, 1968), pp. 28-159.

[123] S.V. Kamat and J.P. Hirth, "Dislocation injection in strained multilayer structures," *J. Appl. Phys.* **67**, 6844 (1990).

[124] J.W. Matthews, A.E. Blakeslee, and S. Mader, "Use of misfit strain to remove dislocations from epitaxial thin films," *Thin Solid Films* **33**, 253 (1976).

[125] W.T. Masselink and T.F. Kuech, "Velocity-field characteristics of electrons in doped GaAs," *J. Electron. Mat.* **18**, 579 (1989).

[126] J.A. del Alamo and T. Mizutani, "An $In_{0.52}Al_{0.48}As/n^+$-$In_{0.53}Ga_{0.47}As$ MISFET with a heavily doped channel," *IEEE Electron Dev. Lett.* **8**, 534 (1987).

[127] S.R. Bahl and J.A. del Alamo, "An $In_{0.52}Al_{0.48}As/n^+$-$In_xGa_{1-x}As$ HFET with an In-enriched channel," Proc. 2nd Int. Conf. on InP, 100 (1990).

[128] S.R. Bahl, W.J. Azzam, and J.A. del Alamo, "Strained-Insulator $In_xAl_{1-x}As/n^+$-$In_{0.53}Ga_{0.47}As$ HFET," *IEEE Trans. Electron Devices* **38**, 1986 (1991).

[129] S.R. Bahl, B.R. Bennett, and J.A. del Alamo, "A high-voltage, doubly-strained $In_{0.41}Al_{0.59}As/n^+$-$In_{0.65}Ga_{0.35}As$ HFET," Proc. 4th Int. Conf. on InP, 222 (1992).

[130] S.R. Bahl, B.R. Bennett, and J.A. del Alamo, "Doubly-strained $In_{0.41}Al_{0.59}As/n^+$-$In_{0.65}Ga_{0.35}As$ HFET with high breakdown voltage," submitted to *IEEE Electron Dev. Lett.*

[131] K. Hikosaka, S. Sasa, N. Harada, and S. Kuroda "Current-gain cutoff frequency comparison of InGaAs HEMTs," *IEEE Electron Dev. Lett.* **9**, 241 (1988).

[132] K.Y. Cheng and A.Y. Cho, "Silicon doping and impurity profiles in GaInAs and AlInAs grown by MBE," *J. Appl. Phys.* **53**, 4411 (1982).

[133] J.M. Kuo, T.-Y. Chang, and B. Lalevic, "$In_{0.6}Ga_{0.4}As/In_{0.45}Al_{0.55}As$ pseudomorphic modulation-doped field-effect transistors," *IEEE Electron Dev. Lett.* **8**, 380 (1987).

[134] Th. Schapers, J. Appenzeller, R. Meyer, H. Hardtdegen, H. Loken-Larsen, and H. Luth, "Electrical characterization of strained modulation-doped $In_xGa_{1-x}As$/InP heterostructures with extremely high mobilities," Proc. of the 4th Int. Conf. on InP and Related Materials (1992), pp. 485-488.

[135] R.J. Hauenstein, B.M. Clemens, R.H. Miles, O.J. Marsh, E.T. Croke, and T.C. McGill, "Strain relaxation in SiGe/Si heterostructures," *J. Vac. Sci. Technol.* **B 7**, 767 (1989).

[136] D.C Houghton, C.J. Gibbings, C.G. Tuppen, M.H. Lyons, and M.A.G. Halliwell, "Equilibrium critical thickness for SiGe strained layers on (100) Si," *Appl. Phys. Lett.* **56**, 460 (1990).

[137] J. Spitzer, K. Thonke, R. Sauer, H. Kibbel, H.-J. Herzog, and E. Kasper, "Direct observation of band-edge luminescence from ultrametastable silicon-germanium alloy layers," *Appl. Phys. Lett.* **60**, 1729 (1992).

[138] R. Hull and J.C. Bean, "Thermal stability of Si/GeSi/Si heterostructures," *Appl. Phys. Lett.* **55**, 1900 (1991).

[139] S.-M. Jang, H.-W. Kim, and R. Reif, "Thermal stability of Si/SiGe/Si heterostructures deposited by very low pressure chemical vapor deposition," *Appl. Phys. Lett.* **61**, 315 (1992).

[140] G.P. Watson, D.G. Ast, T.J. Anderson, Y. Hayakawa, and B. Pathangey, "The thermal stability of lattice mismatched InGaAs grown on patterned GaAs," *J. Electron. Mat.* **20**, 703 (1991).

[141] B.W. Dodson, "Nature of misfit dislocation sources in strained-layer semiconductor structures," *Appl. Phys. Lett.* **53**, 394 (1988).

[142] D.J. Eaglesham, E.P. Kvam, D.M. Maher, C.J. Humphreys, and J.C. Bean, "Dislocation nucleation near the critical thickness in GeSi/Si strained layers," *Phil. Mag.* **A59**, 1059 (1989).

[143] K. Fujiwara, K. Kanamoto, Y.N. Ohta, Y. Tokuda, and T. Nakayama, "Classification and origins of GaAs oval defects grown by MBE," *J. Cryst. Growth* **80**, 104 (1987).

[144] M.A. Herman and H. Sitter, Molecular Beam Epitaxy (Springer-Verlag, New York, 1989), pp. 303-305.

[145] B.A. Fox and W.A. Jesser, "Investigation of the asymmetric misfit dislocation morphology in epitaxial layers with the zinc-blende structure," *J. Appl. Phys.* **68**, 2739 (1990).

[146] B. W. Dodson, "Work-hardening and strain relaxation in strained-layer buffers," *Appl. Phys. Lett.* **53**, 37 (1988).

[147] J.F. Klem, W.S. Fu, P.L. Gourley, E.D. Jones, T.M. Brennan, and J.A. Lott, "Role of substrate threading dislocation density in relaxation of highly strained InGaAs/GaAs quantum well structures," *Appl. Phys. Lett.* **56**, 1350 (1990).

[148] G.J. Whaley and P.I. Cohen, "Relaxation of strained InGaAs during MBE," *Appl. Phys. Lett.* **57**, 144 (1990).

[149] J.C. Vlcek, "Molecular beam epitaxial growth and applications of graded bandgap InGaAlAs semiconducting alloys," PhD Thesis, MIT, 1991.

[150] L.E. Tarof, C.J. Miner, and A.J. Springthorpe, "Epitaxial layer thickness measurements by reflection spectroscopy," *J. Electron. Mat.* **18**, 361 (1989).

[151] T. Fujii, T. Inata, K. Ishii, and S. Hiyamizu, "Heavily Si-doped InGaAs lattice-matched to InP grown by MBE," *Electron. Lett.* **22**, 191 (1986).

[152] Y.G. Chai, R. Chow, and C.E.C. Wood, "The effect of growth conditions on Si incorporation in MBE GaAs," *Appl. Phys. Lett.* **39**, 800 (1981).

[153] J. W. Matthews, "Defects associated with the accomodation of misfit between crystals," *J. Vac. Sci. Technol.* **12**, 126 (1975).

[154] J. W. Matthews, "Coherent interfaces and misfit dislocations," in Epitaxial Growth, Part B, edited by J. W. Matthews, (Academic Press, New York, 1975) pp. 560-610.

[155] J. P. Hirth, "On dislocation injection into coherently strained multilayer structures," *S. Afr. J. Phys.* **9**, 72 (1986).

[156] E. A. Fitzgerald, "The Properties, Control, and Elimination of Misfit Dislocations in Semiconductor Heterostructures," PhD Thesis, Cornell (1989).